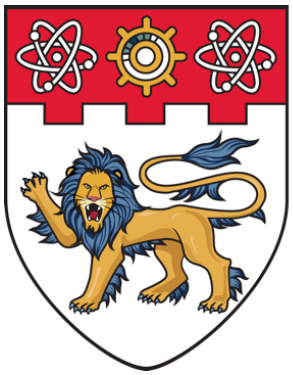

NANYANG TECHNOLOGICAL UNIVERSITY
SINGAPORE

POLYPHTHALONITRILE MEMBRANE MATERIALS: MICROSTRUCTURE CHARACTERISTICS AND GAS PERMEATION BEHAVIOR

HU CHUN-PO

GRADUATE COLLEGE

INTERDISCIPLINARY GRADUATE PROGRAMME

NANYANG ENVIRONMENT & WATER RESEARCH INSTITUTE

2024

POLYPHTHALONITRILE MEMBRANE MATERIALS: MICROSTRUCTURE CHARACTERISTICS AND GAS PERMEATION BEHAVIOR

HU CHUN-PO

GRADUATE COLLEGE

INTERDISCIPLINARY GRADUATE PROGRAMME

NANYANG ENVIRONMENT & WATER RESEARCH INSTITUTE

A thesis submitted to the Nanyang Technological University

in partial fulfilment of the requirement for the degree of

Doctor of Philosophy

2024

Statement of Originality

I hereby certify that the work embodied in this thesis is the result of original research, is free of plagiarised materials, and has not been submitted for a higher degree to any other University or Institution.

06 Aug 2024

. . . . . .

Date

. . . . . .

HU CHUN-PO

Supervisor Declaration Statement

I have reviewed the content and presentation style of this thesis and declare it is free of plagiarism and of sufficient grammatical clarity to be examined. To the best of my knowledge, the research and writing are those of the candidate except as acknowledged in the Author Attribution Statement. I confirm that the investigations were conducted in accord with the ethics policies and integrity standards of Nanyang Technological University and that the research data are presented honestly and without prejudice.

08/08/2024

. . . . . .

Date

. . . . . .

HU XIAO

Authorship Attribution Statement

This thesis contains material from 2 paper published in the following peer-reviewed journal conferences in which I am listed as an author.

Chapter 5 is published as Chun-Po Hu, Yen Nan Liang, Hong-Li Yang, Wei-Song Hung, Jacob Song Kiat Lim, Zeming He, Xiao Matthew Hu. Polyphthalonitrile as a novel precursor for carbon membranes: Tunable microstructure characteristics and gas permeation behavior, Carbon 228 (2024), 119284, DOI: 10.1016/j.carbon.2024.119284

The contributions of the co-authors are as follows:

- I prepared the manuscript, designed and conducted the experiments, performed all characterization and result analysis at Graduate College.
- Field Emission Scanning Electron Microscopy and X-ray Diffraction analysis were conducted by me in the Facility for Analysis, Characterization, Testing and Simulation (FACTS), NTU.
- Transmission Electron Microscopy was conducted by Dr Liang Yen Nan in the Facility for Analysis, Characterization, Testing and Simulation (FACTS), NTU.
- Dr Yang Hong-Li conducted the Positron Annihilation Lifetime Analysis and Prof Hung Wei-Song provided critical assessment on the analysis.
- Dr He Zeming provided critical revise and editing on the manuscript.
- Prof Hu Xiao provided research supervision and revised the manuscript.

Chapter 6 is published as Chun-Po Hu, Jacob Song Kiat Lim, Kuo-Hsiang Ping, Wei-Song Hung, Yen Nan Liang, Xiao Matthew Hu. Understanding hydrogen solubility and free volume characteristics in charge-transfer phthalonitrile prepolymer and polyimide blend membranes, Journal of Membrane Science 687 (2023), 122058, DOI: 10.1016/j.memsci.2023.122058

The contributions of the co-authors are as follows:

- I prepared the manuscript, designed and conducted the experiments, performed all characterization and result analysis at the Graduate College.
- Field Emission Scanning Electron Microscopy and X-ray Diffraction analysis were conducted by me in the Facility for Analysis, Characterization, Testing and Simulation (FACTS).
- Dr Lim Song Kiat Jacob provided guidance in the synthesis of resorcinol-based phthalonitrile prepolymer.
- Mr Kuo-Hsiang Ping conducted the gas sorption analysis.
- Prof Hung Wei-Song conducted Positron Annihilation Lifetime Analysis provided critical assessment on the analysis.
- Dr Liang Yen Nan provided critical revise and editing on the manuscript.
- Prof Hu Xiao provided research supervision and revised the manuscript.

08/08/2024

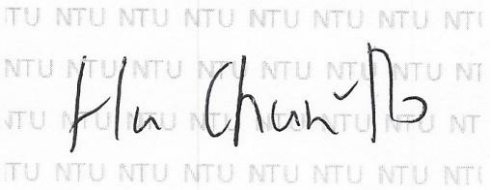

. . . . . .

Date

. . . . . .

Hu Chun-Po

Acknowledgments

First and foremost, I sincerely appreciate and respect my supervisor, Professor Hu Matthew Xiao, for his support and encouragement to me on pursuing knowledge together on both sides of fundamental and applied studies. I would like to thank him for his guidance in developing my studies and thesis. Moreover, when days went back to his speech in Taiwan, his enthusiasm enlightened my path to pursuing a Ph.D. in Singapore. Of course, I am grateful for learning many other merits from him along with research.

I also want to thank my co-supervisor and mentor, Professor Shen Zexiang, Professor Chew Jia Wei, and members of QE and OD for their encouragement and support. It's my fortune to have my thesis advisory committee members who are experts on both inorganic materials and computational simulation. Besides, I am grateful to both research groups in NEWRI and MSE. I especially appreciate Dr. Liang Yen Nan, Dr. Lim Jacob, Dr. Yan Welli, Dr. Chen Hui, Dr. Lu Yong, Dr. Pan Xiaoyong, Dr. Chen Xuelong, Dr. He Zeming, Dr. Zoey, Dr. Ng Joseph, Dr. Feng Han, Dr. Bao Yueping, Dr. Nupur Gupta, Dr. Liang Alvin, Dr. Mo Zijing, and Professor Tan Kwan Wee for their kind support of my study in many discussions. Moreover, I am thankful to NEWRI for its financial and academic support. This center builds a place for creative, foreseeing, and dynamic research for interdisciplinary studies to benefit both the environment and society.

I also extend my appreciation to Professor Lai Juin-Yih for his encouragement and continuous support from the beginning of my academic journey.

Last but not least, I express my great appreciation to my parents and my family, for with great hope, all of us have been healthy and happy. I wish to give my heartfelt gratitude and endless miss to my beloved grandmother and grandfather for their lifetime support and effort to all the families; I wish both of you are resting in a peaceful place together.

My great appreciation to my families, and all my group members, supporters, and friends! I hope you and your families are safe and healthy and we will have a better life experience in a bright future.

Table of contents

Table Captions

Figure Captions

Abbreviations

CMS	Carbon molecular sieve
CoPc	Cobalt-doped phthalocyanine
CoPPN	Cobalt-doped polyphthalonitrile
CTC	Charge-transfer complex
CuPc	Copper-doped phthalocyanine
CuPPN	Copper-doped polyphthalonitrile
DFT	Density functional theory
DMA	Dynamic mechanical analysis
DMSO	Dimethyl sulphoxide
DTG	Derivative thermogravimetry
EMI	Electromagnetic interference
FESEM	Field emission scanning electron microscopy
FFV	Fractional free volume
FTIR-ATR	Fourier-transform infrared spectroscopy with attenuated total reflectance
GPC	Gel permeation chromatography
GPU	Gas permeation unit
IPA	Isopropyl alcohol
IPN	Interpenetrating polymer network
M_n	Number average molecular weight
M_w	Weight average molecular weight
NMP	N-methyl-2-pyrrolidone
o-Ps	Ortho-positronium
PAL	Positron annihilation lifetime
PALS	Positron annihilation lifetime spectroscopy
PAN	Polyacrylonitrile
PBI	Polybenzimidazole
Pc	Phthalocyanine
PDI	Polydispersity index

PEEK	Poly(ether ether ketone)
PEI	Polyetherimide
PES	Polyethersulfone
PFA	Poly(furfuryl alcohol)
PIM	Polymer of intrinsic microporosity
PLM	Polarized light microscopy
PMMA	Polymethylmethacrylate
PPN	Polyphthalonitrile
pPN	Resorcinol-based phthalonitrile prepolymer
p-Ps	para-positronium
PR	Phenolic resin
Ps	Positronium
PTFE	Polytetrafluoroethylene
PU	Polyurethane
STP	Standard temperature and pressure
T_d	Decomposition temperature
TEM	Transmission electron microscopy
TGA	Thermogravimetric analysis
T_g	Glass transition temperature
UV-vis	Ultraviolet-Visible Spectroscopy
XRD	X-ray diffraction
ZnPc	Zinc-doped phthalocyanine
ZnPPN	Zinc-doped polyphthalonitrile

Abstract

Polyphthalonitrile (PPN) has emerged as a promising candidate for high-performance polymeric and carbon materials for various applications due to its excellent thermal stability, char yield, and versatile molecular design. However, the microstructure characteristics and gas permeation behavior of PPN-based polymeric and carbon materials has been rarely understood, hindering their potential on emerging sustainable and energy-efficient membrane gas separations (CO_2/N_2, O_2/N_2, H_2/CO_2, and H_2/N_2). This thesis systematically investigates the adjustability of the microstructure and gas transport properties of resorcinol-based PPN and the derived carbon materials in the context of membrane. It was demonstrated that metal-ion doping and thermal curing could significantly adjust the molecular arrangement and gas separation performance of the PPN network as well as the derived carbon molecular sieve (CMS) membranes. The carbonization of the PPN network formed CMS membranes with superior ideal gas separation performance comparable to state-of-the-art gas permeability-selectivity trade-off relationship of membranes. Notably, the stacking arrangement and interchain spacing of the PPN precursor were identified as key factors in shaping the pore size distribution and molecular sieving ability of the PPN-CMS membranes. Furthermore, incorporating PPN with polyimide (PI) formed charge-transfer complexes that narrowed the free volume distribution, enhancing H_2 solubility, solubility selectivity, and permselectivity of the PPN/PI blend membranes. These findings provide crucial insights into the microstructure-property relationships of PPN-based materials and demonstrate their great potential as advanced membrane materials for membrane gas separation applications.

Lay Summary

Polyphthalonitrile (PPN) is a unique class of heterocyclic polymer resin known for its good processibility, exceptional thermal stability, and high char yield. Despite the rapid development of PPN-derived high-performance polymeric and carbonaceous materials, there has been a lack of fundamental understanding of their microstructure characteristics and gas permeation behavior. This thesis aims to investigate the adjustability of the microstructure characteristics of PPN-based polymeric/carbonaceous materials and demonstrate the potential of PPN-based membranes on energy-efficient membrane gas separation applications, i.e., CO_2 capture, O_2-fuel enrichment, and H_2 purification.

The first objective was to understand the relationship between microstructure characteristics and gas permeation behavior of PPN and PPN-derived microporous carbon materials in the context of membranes. It was demonstrated that doping metal ions or curing treatment could adjust the molecular arrangement of the PPN network. The microporosity of PPN-derived microporous carbon materials was identified to be generated from the thermal decomposition of the nonporous PPN network.

To further obtain in-depth insights into microstructure evolution from PPN precursors to derived microporous carbon materials, PPN networks with various molecular arrangement adjusted by curing treatment and the derived carbon molecular sieve (CMS) membranes were characterized. It was found that the enhanced aromatic-aromatic stacking of the PPN network was a key factor in generating small-sized, narrow-

distributed ultramicropores in the derived carbon materials. The cured PPN network with enlarged average chain spacing and promoted π-π stacking could produce PPN-CMS membranes with increased average interchain distance and enhanced molecular sieving ability. Notably, it was demonstrated that the PPN-derived carbon molecular sieve membranes possessed promising gas separation performance comparable to that of state-of-the-art membranes.

The third aim was to explore PPN as an advanced membrane material via adjusting the microstructure characteristics of PPN and a commercially available polyimide resin. Incorporating PPN into polyimide enabled the formation of intermolecular charge-transfer complexes, resulting in narrowed free volume cavity size and distribution. Consequently, the hydrogen solubility and selectivity of the novel PPN/polyimide blend membranes was significantly improved, leading to enhanced hydrogen separation performance surpassing the state-of-the-art polymeric membranes.

In summary, this thesis advances the understanding of microstructure characteristics and gas permeation behavior of PPN-based materials and extends their potential applications to membrane gas separation. The microstructure-property relationship of PPN-based polymeric and carbon materials was established. The microstructure evolution from PPN precursor to the derived microporous carbon was elucidated. The potential of PPN as an advanced membrane material for various gas separation applications was demonstrated. The insights gained from this work pave the way for further development of high-performance PPN-based polymeric and carbon materials.

Chapter 1

Introduction

Though PPN resin and its derived microporous carbon materials are regarded as outstanding gas barriers and absorbents in various emerging vital applications, there is a lack of understanding of their microstructure characteristics and gas permeation behavior. Furthermore, previous studies treat PPN as an excellent carbon source but generally overlook the fundamental mechanism of the microstructure evolution of the polymer toward microporous carbon. This chapter introduces the rationale, hypothesis, objectives, and scope of this study and provides an overview of the chapters in this dissertation.

1.1 Background

Polyphthalonitrile (PPN) resin has attracted intensive research interest as a high-temperature polymeric barrier and high char yield carbon precursor for various applications [1, 2]. In particular, resorcinol-based PPN resin has been widely studied as a precursor to fabricate carbon materials [3-5]. This is due to the commercially available PPN resin possessing high decomposition temperature and high char yield as an excellent carbon source [5, 6]. Many techniques have been reported to introduce porosity in the PPN network to produce PPN-derived hierarchical carbon, supposedly composed of micropores, mesopores, and macropores for various application purposes [2-5]. However, the nature of microporosity (< 2 nm) of resorcinol-based PPN-derived carbon has not been fully revealed. Besides, the microstructure evolution from the PPN precursor to the derived carbon materials require a comprehensive understanding for developing high-performance materials. The understanding of the microstructure-property relationship of PPN and PPN-derived carbon materials might extent their application as thin-film or composite materials for barrier or separation at the molecular level, such as gas molecules with kinetic diameters less than 4 Å.

Compared to traditional distillation techniques, gas separation via membrane has become a promising way to address various environmental challenges, including carbon capture and energy issues. The advancement of polymeric materials enabled the thrilling development of contemporary membrane gas separation technology. For decades, polymers, such as polyimide, played a critical role in the fabrication of membranes due to their good availability, scalability, and mechanical and gas separation properties.

Polymeric membranes follow the solution-diffusion gas transport mechanism to achieve the ability to differentiate gas molecules. However, the polymeric membranes generally were facing the trade-off effect on gas separation performance.

Recently, the development of carbon molecular sieve (CMS) membranes derived from polymeric materials holds promise to become another large-scalable membrane fabrication for gas separation. The CMS membranes derived from heterocyclic polymers often possess gas permeability that is several magnitudes higher than their polymeric counterparts while maintaining outstanding molecular sieving ability due to their unique carbon microstructure. However, those heterocyclic resins generally require organic solvents for membrane fabrication. The monomer (oligomer) of thermosetting PPN resins can be potentially processed without the use of organic solvent, which holds the promise of achieving solvent-free fabrication of CMS membranes. However, the lack of understanding of the microstructure characteristics and gas permeation behavior of PPN and the derived carbon materials hindered the application of these high-performance materials in the context of membranes.

1.1 Problem statement/Hypothesis

PPN resin has been described as a class of thermally stable polymeric materials for gas barrier applications [1]; however, its gas permeation behavior has seldom been reported. Similarly, PPN-derived hierarchical carbon has been developed for various applications, but its intrinsic microstructure characteristics remain unclear in published literature. Moreover, there is a lack of insights into the relationship between microstructure

characteristics and gas permeation properties of the PPN-based materials. Understanding the microstructure-property relationship can benefit the development of PPN-based materials for membrane applications.

Problem statement

> *Most reported studies on PPN resins are mainly focused on their thermal/mechanical properties and carbon yield. The formation mechanism of carbon structure from PPN resin has been intensively studied. However, the lack of insights into the microstructure characteristics and gas permeation properties of the PPN network and the derived carbon materials, particularly their microstructure-property relationships, hinders these materials from being useful for gas separation applications.*

Most previous studies focused on curing treatment to enhance the thermal stability and char yield of PPN resins. However, most works based on carbon materials pyrolyzed from PPN resins ignored studying their fundamental microporous structure. Instead, the focus was on introducing extra porosity (i.e., micro-, meso-, and macropores) via post-treatment of the PPN precursors. Tay hypothesized that PPN-derived carbon materials might be microporous due to their rigid moieties, such as phthalocyanine [7]. However, Weng *et al.* [4] observed no apparent microporosity in PPN-derived carbon via typical microstructure analysis. The controversy pointed out the insufficient understanding of the fundamental microstructure characteristics of PPN and the derived carbon materials. This

work systematically studied the microstructure-property relationship of PPN and PPN-derived carbon to advance their application in the context of membrane materials.

Hypothesis

This thesis proposes that the adjustment of the microstructure arrangement of thermosetting PPN resin can alter that of the derived carbon materials; thus, the gas permeation behavior of the carbon membranes shall change with subtle differences in microstructure characteristics.

Despite the complicated nature of PPN polymerization, the heterocyclic moieties dominate the microstructure of the cured PPN resins. Intuitively, the crosslinking of the phthalonitrile group might be the main effect on the microstructure arrangement of the polymer network and the derived carbon matrix. Metal-ion doping was utilized to test the hypothesis that metal-ion-doped phthalocyanine moieties might facilitate the aromatic-aromatic stacking of planar heterocyclic moieties. Besides, the microstructure arrangement of the PPN network should be subjected to curing history or thermal treatment, which is also essential to achieve high glass transition temperature and molecular chain rigidity of the polymer network. Lastly, the heterocyclic moieties with electron donor/acceptor properties might be able to adjust the microstructure characteristics of other types of heterocyclic polymers, such as polyimide.

1.2 Objectives and scope

There are three main objectives addressed sequentially in this thesis. This work aims to:

1) To understand the relationship between microstructure characteristics and gas permeation behavior of PPN and PPN-derived microporous carbon materials in the context of membranes.

2) To provide in-depth insights into the microstructure evolution of the PPN-derived carbon from its polymeric precursor.

3) To explore PPN as an advanced membrane material for adjusting the microstructure characteristics of membranes fabricated from commercially available polyimide resin.

Previous studies on the microstructure characteristics of PPN and its derived carbon were limited to typical gas adsorption analysis (i.e., cryogenic N_2 adsorption), which might have limited ability to determine microporosity less than 2 nm. PALS, CO_2 adsorption, and gas permeation analyses revealed the existence and distribution of micropores and ultramicropores of PPN-derived microporous carbon materials.

The fabrication of PPN and the derived carbon in the context of membranes enabled gas permeation analysis using small gas molecules of various sizes to probe the subtle differences in the microstructure arrangement of the materials. More importantly, the gas permeation analysis on PPN-based membranes provided a solid foundation for these materials in gas barrier or separation applications.

By revealing the relationship between microstructure characteristics and gas permeation behavior of PPN-based polymer and carbon membranes, the fundamental understanding of how to adjust their pore size distribution was established for future applications.

Incorporating PPN with existing polymeric membrane materials reveals the potential of the heterocyclic polymer to shape the pore size distribution and intrinsic gas transport properties.

Based on the understanding and insights gained from the microstructure study of PPN and the derived carbon materials, the potential of these materials on various gas separation applications has been demonstrated.

1.3 Dissertation Overview

The thesis addresses the lack of insights into the microstructure characteristics and gas permeation behavior of PPN resin and its derived carbon materials in published literature. The thesis consists of seven chapters, which are summarized as follows.

Chapter 1 introduces the problem statement, hypothesis, and outlines of this work.

Chapter 2 reviews the literature concerning thermoset PPN resin, PPN-derived carbon materials, polymeric membrane materials, carbon membrane materials, and gas permeation mechanisms involving polymeric and carbon membranes. This chapter

identified the knowledge gap from relevant published literature addressed in this thesis.

Chapter 3 introduces the experimental methodology, including instruments to address the proposed research objective and scope. The working principles of instruments were described, and possible experimental errors were discussed.

Chapter 4 presents the adjustment of microstructure characteristics and gas permeation behavior of the PPN network and its derived carbon materials via metal-ion doping. This section identified the potential of PPN-derived materials on membrane gas separation.

Chapter 5 systematically investigates the mechanism of microstructure evolution of PPN and PPN-CMS membranes. It was revealed that the effects of curing treatment and pyrolysis temperature play critical roles in shaping pore size distribution and gas permeation behavior of PPN-derived microporous carbon membranes.

Chapter 6 presents the blending of PPN to adjust the microstructure characteristics of polyimide membranes and identified the effects of charge-transfer complex and thermal treatment on the free volume characteristics and gas transport properties of the blends.

Chapter 7 summarizes the research findings and includes recommendations for further investigations.

1.4 Findings and Outcomes/Originality

This study presents novel findings and impactful outcomes as follows:

1) Explored the adjustability of microstructure characteristics and gas permeation behavior of PPN and the derived carbon materials.

2) Demonstrated PPN and the derived carbon materials as promising candidates for gas separation membranes.

3) Proposed and tested a mechanism for the microstructure evolution of PPN to the derived microporous carbon materials at the angstrom level.

4) Established the relationship between microstructure characteristics and gas permeation behavior of PPN and the derived microporous carbon membranes.

5) Identified the impact of incorporating PPN in commercially available polyimide on the microstructure characteristics and gas transport properties of the blend membranes.

Chapter 2

Literature Review

PPN is a unique class of heterocyclic resin with high thermal stability and char yield. In spite of the rapid development of PPN to high-performance carbon materials, which generally requires an in-depth understanding of microporosity, previous works lack an understanding of the microstructural relationship between polymeric precursor and PPN-derived carbonaceous materials at the sub-nanometer level. A review of gas separation membrane materials of heterocyclic polymers and carbons has also been presented to evaluate the potential of PPN materials on this energy-efficient separation application that requires size-sieving resolution at sub-0.1 nm. This chapter will review the microstructure characteristics of PPN-based polymeric and carbon materials to identify knowledge gaps regarding polymeric and carbonaceous gas separation membrane materials.

2.1 Polymerization and carbonization of the heterocyclic PPN resin

The chemical reaction of phthalonitrile to form heterocyclic structures has been intensively studied [6, 8, 9]. The nitrile groups can form isoindolenine, triazine, and phthalocyanine moieties via addition-polymerization (**Figure 2.1**) [1, 3]. With organic or inorganic catalysts, the PPN resin can be obtained from polymerizing phthalonitrile monomers in melting form or organic solution [6, 10]. The mixture of phthalonitrile monomer and catalyst was firstly melted into liquid state above its melting temperature, followed by the polymerization of phthalonitrile moieties above 200 ℃ into oligomers [3] and thermosetting polymer networks [11, 12]. That is to say, the process window of PPN depends on the melting temperature of the monomers. Furthermore, a meltable and thermally stable catalyst is preferred to form a uniform mixture of monomers and catalysts [6, 8]. For instance, it required heating the monomers and the organic diamine catalyst above their melting temperatures of 186 ℃ and 173 ℃, respectively, to promote a homogeneous reaction to form a resorcinol-based polyphthalonitrile oligomer or a polyphthalonitrile network [3, 5, 13]. However, the insoluble inorganic catalyst could not be homogeneously dispersed in the polymer matrix [13]. Another synthesis approach is to dissolve phthalonitrile monomers with organic catalysts in a high boiling temperature solvent (i.e., NMP) [10]. The use of solvent can also well disperse insoluble inorganic catalysts to facilitate PPN polymerization [10].

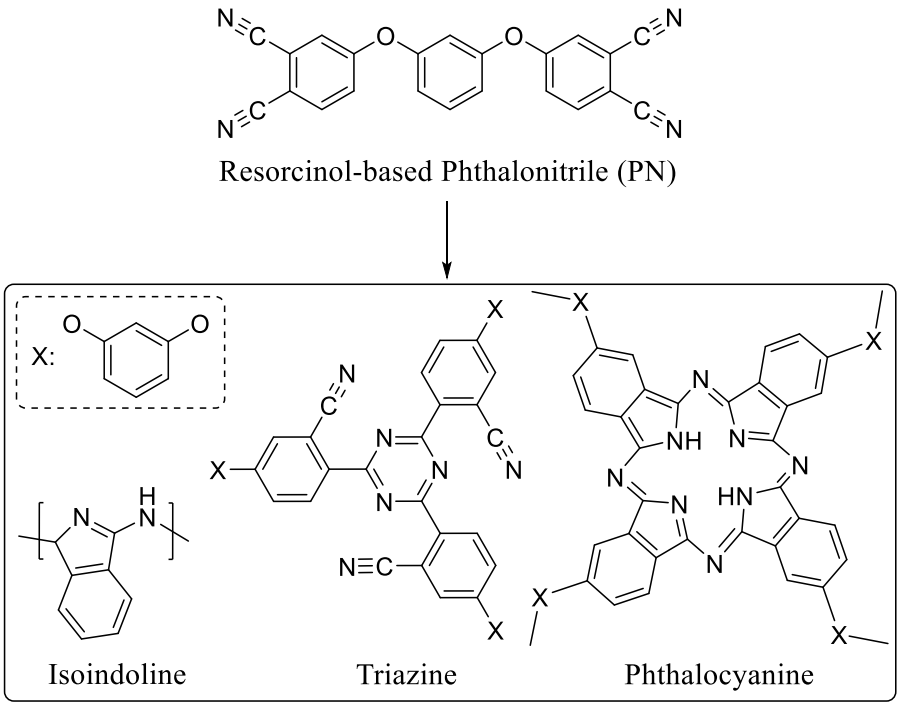

Figure 2.1 Scheme of PN monomer and its derived polymer network [3]

The polar solvent can dissolve some inorganic metal salts, allowing metal ions to react with phthalonitrile to form metal-ion-doped phthalocyanine moieties [9, 14]. The incorporation of metal ions may be able to adjust the molecular arrangement of the PPN network by introducing cation-aromatic interactions [15]. Details of the microstructure characteristics of PPN will be discussed in ***Chapter 2.1.1***.

The phthalonitrile-derived heterocyclic moieties were the main reason for the exceptional thermal stability of PPN resins [6]. There is little doubt that PPN requires progressive thermal treatment with elevated curing temperature to achieve exceptional thermal stability [9]. This was because the higher curing temperature can kinetically facilitate the crosslinking reaction of pendant phthalonitrile groups, resulting in a more stable PPN network [16].

Due to the excellent thermal stability and outstanding char yield of the PPN network, the thermosetting resin is a promising candidate for obtaining high-performance carbon materials [4, 5, 7, 9, 17-24]. The abundant heterocyclic structure with nitrogen atoms can form a nitrogen-doped carbon structure after the pyrolysis process [20]. For resorcinol-based polyphthalonitrile, the carbonization of the polymer network can occur as low as 500 ℃ by cleavage of oxygen-containing moieties to form a sp^2/sp^3 hybrid carbon structure [25]. Above 550 ℃, the PPN-derived carbon matrix becomes electrically conductive, indicating the formation of more graphitic (sp^2) carbon structures [4, 5]. The increase in pyrolysis temperatures resulted in more graphitic components in the PPN-derived carbon [5]. Meanwhile, the nitrogen content decreases with increasing pyrolysis temperatures due to the decomposition of heterocyclic moieties [4, 5, 25]. The PPN-derived carbon can transfer from straticulate-like to graphitic-like amorphous carbonaceous microstructure in the temperature range from 500 ℃ to 1000 ℃ [5, 20]. However, the evolution of carbon microstructure from the microstructure characteristics of PPN resin is absent in published literature. The microstructure characteristics of PPN-derived carbon are discussed in ***Chapter 2.1.2***.

2.1.1 Microstructure characteristics of PPN resins

Snow *et al.* [15] systematically studied the microstructure characteristics of PPN networks in comparison to phthalocyanine monomers and model polyphthalocyanine networks (**Figure 2.2**). It was found that the polymerization of bisphthalonitrile monomer was able to form a semi-crystalline polymer network with a distinguished π-π stacking crystallinity peak at $2\theta = 26^{\circ}$ (d-spacing = 3.4 Å). This was mainly attributed to the stacking of planar phthalocyanine moieties in the polymer network.

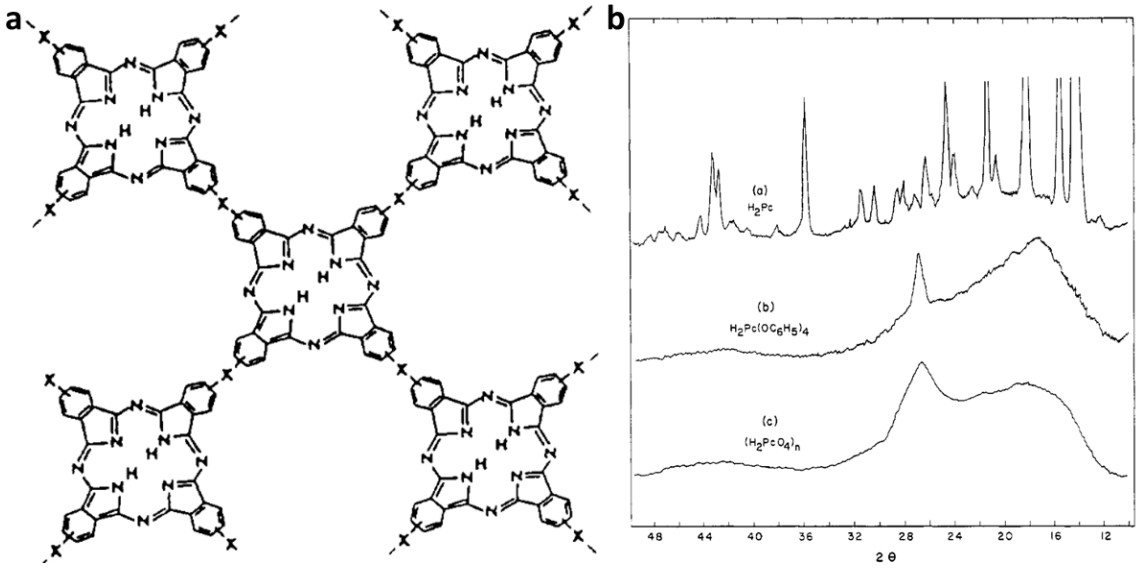

Figure 2.2 Molecular structure and microstructure arrangement of polyphthalocyanine network derived from phthalonitrile resin [15]. (a) Modeled polyphthalocyanine network (b) XRD pattern of PPN network.

Zhang's group [26-30] observed that an increase in curing temperature resulted in slightly decreased d-spacing values of pyrimidine and vinylpyridine-based phthalonitrile resins. It was proposed that the crosslinking of phthalonitrile could narrow the average intermolecular distance of the polymer chain. Mushtaq *et al.* [31] reported that the

thermal curing of poly(thioether ether imide)s containing terminal phthalonitrile groups resulted in decreased d-spacing due to crosslinking of the polymer network. However, the thermal curing of poly(thioether ether imide)s containing pendant nitrile groups resulted in slightly increased d-spacing, which might be attributed to the formation of bulky triazine groups. Liu *et al.* [32] proposed that the crosslinking of phthalonitrile that was end-capped onto poly(aryl ether ketone) might increase the intermolecular distance of ball-milled clay after thermal curing, resulting in the exfoliation of clay. Zhang *et al.* [5] exanimated the XRD spectrum of resorcinol-based polyphthalonitrile against thermal treatment. They observed that graphite-like molecular arrangement was promoted at elevated thermal treatment temperature, though the d-spacing values of π-π stacking about 0.34 to 0.36 nm were not clearly observed. Given the complicated nature of the PPN network derived from resorcinol-based phthalonitrile monomer, the stacking of planar phthalonitrile-derived moieties might be hindered by other moieties, resulting in the amorphous nature of the polymer network [15].

Many researchers initially hypothesized that phthalocyanine moieties might form intrinsic microporosity in the phthalonitrile-derived covalent network [7, 15, 33, 34]. McKeown *et al.* [35] demonstrated that the metal-ion-doped and neat phthalocyanine network can possess intrinsic microporosity with a rigid and twisted spirocyclic molecular chain (**Figure 2.3**). It was identified that the origination of microporosity of the PPN network with the spirocyclic linker was due to the rigid and nonlinear molecular chain structure instead of phthalonitrile-derived moieties [34]. Adopting rigid and twisted molecular chains into polymer systems was the key to the successful development of the polymer of microporosity (PIM), which possesses high gas permeability due to its

intrinsically high content of micropores or free volume [34]. The superior gas separation performance of PIM membranes is due to their microporous molecular structure that simultaneously favors the sorption and diffusion of gas molecules. For the resorcinol-based polyphthalonitrile network, Liu [9] demonstrated that the polymerization of phthalonitrile monomers might occur in between vacancies constructed by those rigid phthalocyanine or triazine blocks, resulting in limited or no microporosity in PPN networks. However, there are limited insights on the gas transport behavior of PPN-derived membranes in published literature. The gas permeation analysis on resorcinol-based polyphthalonitrile materials in the context of membranes might reveal the intrinsic microstructure characteristics of the thermosetting network.

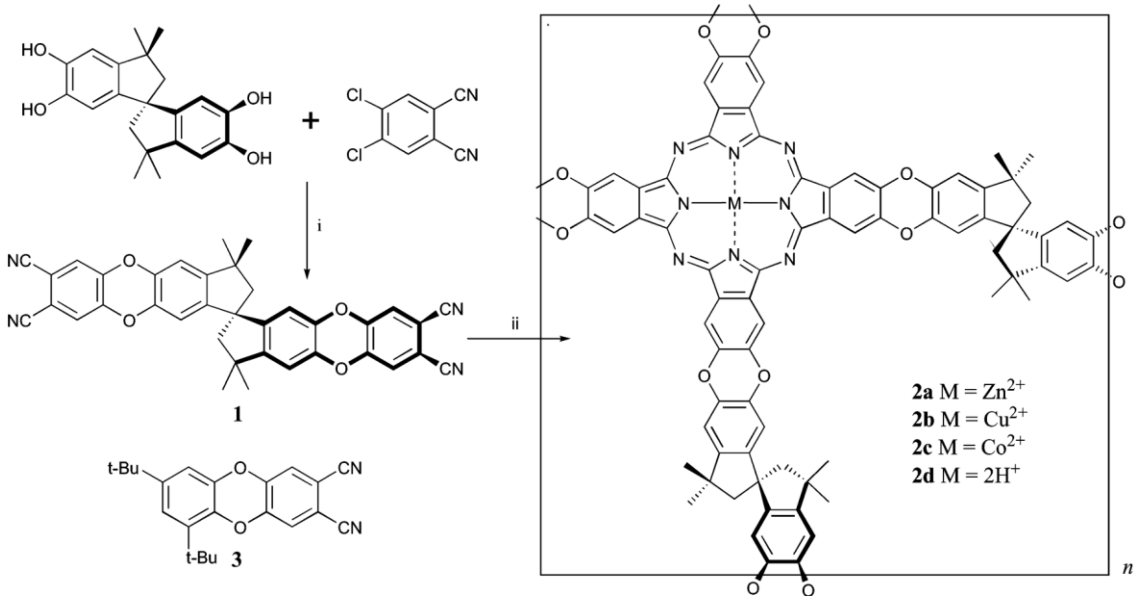

Figure 2.3 PPN-derived microporous polymer network [35].

2.1.2 PPN-derived microporous carbon materials and microstructure characteristics thereof

Phthalonitrile-derived porous carbon materials have been widely studied. Many efforts have focused on functionalizing the PPN-derived carbon materials via introducing porosity in the scale range from nano to micrometer. Zhang *et al.* [5] used the bubble foaming method to obtain resorcinol-based PPN foam, followed by carbonization of the porous polymeric foam into carbon foam. The meso- and microporous carbon materials showed superior EMI shielding effectiveness compared with their polymeric counterparts. It was also found that the PPN-derived carbon foam possessed outstanding mechanical strength in comparison to graphene foams. More recently, Xiao *et al.* [21] demonstrated that incorporating graphene in PPN-derived porous carbon could further improve the mechanical strength and EMI shielding performance of the carbon materials. The extrinsic porosity (mesopore (2-50 nm), macropore (50-100 nm), and macrovoid (>100 nm)) was identified as the key factor to EMI shielding effectiveness of the PPN-derived porous carbon materials.

Introducing microporosity into PPN-derived carbon materials enabled more applications. Weng *et al.* [4] developed activated hierarchical carbon derived from resorcinol-based PPN via co-doping of KOH and urea as activators. The addition of urea only in the PPN matrix could create mesopores or larger pores. It was identified that the reaction of KOH and PPN-derived carbon created abundant meso- and microporosity (< 2 nm), providing high performance for supercapacitor and gas absorbent applications. The blend of PPN with another immiscible polymer (i.e., polyaniline) could also introduce mesopores in the

derived hierarchical carbon materials [17, 36]. The formation of mesopores was possibly due to the aggravated decomposition of the thermally liable polyaniline phases, while the micropores were mainly created by KOH activation [17, 36]. The resorcinol-based polyphthalonitrile/polyaniline-derived carbon materials with high porosity and surface area showed outstanding electrocatalytic decomposition on organic matter in pharmaceutical wastewater [17]. There is, however, no clear evidence in the published literature for the existence of intrinsic microporosity of PPN-derived carbon materials without any modification or activation.

PPN-derived dense carbon materials also widely attract interest for their high char yield. Vladislav Aleshkevich *et al.* [18] improved the mechanical strength of PPN-based carbon materials via carbon fiber reinforcement. It was found that the micrometer scale cracks appeared in the millimeter scale composite materials, possibly resulting from the difference in thermal expansion of the PPN resin and carbon fiber during thermal treatment above 400 ℃. It was proposed that the cracking of the PPN might be beneficial by reducing the internal stress of the composite carbon materials during thermal treatment and improving the overall mechanical performance. Liu [9] reported that the carbonization of PPN-derived composite carbon thin-films above 800 ℃ might form unfavorable micrometer-sized defects. The unstable morphological properties of materials formed by carbonization at high temperatures might hinder the development of defect-free PPN-based carbon membranes for small molecule separation. However, no apparent defects in the PPN thin-films carbonized at 500 ℃ were found. These results indicated that the pyrolysis temperature is a key factor in designing defect-free resorcinol-based polyphthalonitrile-derived carbon thin-films.

Overall, there is a lack of understanding of the intrinsic microporosity of PPN-derived carbon materials. Furthermore, the gas transportation properties of the carbon materials were surprisingly absent from published literature. Investigating the microstructure characteristics and gas permeation behavior of PPN-derived carbon materials may open new opportunities for using PPN-derived carbon materials for membrane gas separation.

2.2 Polymeric materials for gas separation membrane

Membrane gas separation is a promising technique since this process has unique advantages like low capital and operational cost, ease of operation, good scalability, excellent reliability, and low energy requirement. Typically, no phase change is required in the membrane gas separation process. Membrane gas separation is considered a sustainable technology and is gaining more and more interest in replacing traditional thermal separation processes, such as distillation [37].

Numerous materials and membrane designs have been discovered and used in membrane separation, including polymers[38-40], ceramics[41-45], carbon-based materials[46-51], and other novel nanomaterials [52-56] developed recently. Among the above, polymeric membranes were intensively studied due to their excellent mechanical properties, flexibility, processability, scalability, reproducibility, separation performance, and feasible adjustability [57]. These features make such materials candidates for industrial-scale gas separation. **Table 2.1** lists polymeric membrane-based gas separation applications in industrial applications and future interest.

Table 2.1 Current and emerging applications of membrane-based gas separation in industries [58, 59].

Gas pair	Area of application	Materials
H_2/hydrocarbon	Refinery hydrogen recovery	polysulfone, polyimides
H_2/N_2	Ammonia purge gas	polysulfone, polyimides
H_2/CO	Syngas ratio adjustment	polysulfone, polyimides
CO_2/hydrocarbon	Acid gas treatment, greenhouse gas capture	cellulose acetates, polyimides
H_2S/hydrocarbon	Sour gas treating	cellulose acetates, polyimides
He/hydrocarbon	Helium separation	cellulose acetates, polyimides
Hydrocarbon/air	Hydrocarbon recovery	silicone rubber
O_2/N_2	Oxygen enrichment, inert gas generation	polyimides, polysulfone, polyphenylene oxide, substituted polycarbonates
CO_2/CH_4	CO_2 removal from natural or biosynthesized gas	cellulose acetates, polyimides

Gas pair	Emerging area of application	Selectivity	Permeance (GPU)
$C_2^{=}/C_2^{0}$	olefin/paraffin separation	>5	>50
CO_2/CH_4	CO_2 removal from natural or biosynthesized gas	20−30	>100
H_2/CO_2	Syngas purification	>10	>200
CO_2/H_2		>20	
CO_2/N_2	CO_2 capture from power and industrial exhaust gases; Direct carbon dioxide capture	30−50	1000−5000
H_2O/ethanol, H_2O/IPA	vapor/vapor organic solvent dehydration	50−100	1000−3000
aromatic/aliphatic, polar/nonpolar	vapor/vapor organic solvent separation	>10	>500

2.2.1 Gas transport mechanisms for nonporous and microporous membranes

Typically, the solution-diffusion model can be used to describe the separation behavior of nonporous membranes [60]. The gas molecules are first absorbed into the nonporous membrane substance, followed by diffusion cross the membrane subjected to concentration gradient from feed to permeate. That is to say, the gas permeability mainly depends on gas solubility and diffusivity in specific polymers [61]. Robeson [60] first proposed a general trade-off relationship between gas permeability and selectivity of polymeric membranes (**Figure 2.4**). The improvement in selectivity is accompanied by the sacrifice of permeability and vice versa. Rubbery polymers with low Tg and flexible chain structure generally show high permeability but low selectivity [58]. This is mainly due to the high diffusivity but low solubility of the rubbery polymers. On the other hand, a glassy polymer with high T_g and rigid backbone structure usually shows high selectivity but low permeability. The abundant free volumes constructed by rigid polymer chains favor the sorption of gas molecules despite the limited polymer chain mobility, which may compromise the diffusivity coefficient. Given the fact that the solubility selectivity of a glassy polymer is generally similar to that of a rubbery polymer, the improvement of diffusivity selectivity is the main reason for the overall high gas selectivity of glassy polymer membranes. More recently, PIM materials with high free volume improved the gas solubility and diffusivity coefficient of the glassy polymer membranes. As a result, glassy polymers generally possess superior gas permeation performance than rubbery polymers due to their higher gas solubility coefficients (**Figure 2.4**) [62]. However, the scalability of these high-performance PIM materials hindered its wide application.

Modifying commercially available polymers, such as polyimide, remains critical in pursuing high-performance gas separation membranes.

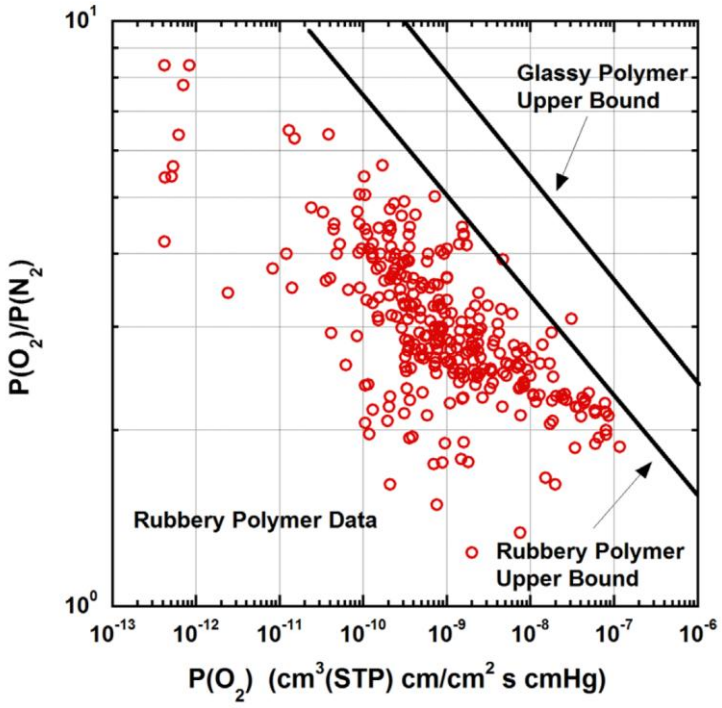

Figure 2.4 The relationship between permeability and selectivity of rubbery and glassy polymer membranes in terms of Robeson-type upper bounds [62, 63].

2.2.2 Heterocyclic polymeric materials for gas separation membranes

Glassy polymers with heterocyclic molecular structures are of particularly interest for gas separation because their rigid polymer chain creates a precise pore size distribution for fractionating small gas molecules. Heterocyclic polymer membranes have been intensively studied to design high-performance gas separation membranes in past decades [64]. Polyimide is one of the most studied high-performance polymers for gas separation membranes because of its good adsorption selectivity and favorable molecular chain

packing for achieving high diffusion selectivity [38]. Furthermore, polyimide also possesses high thermal stability, chemical and solvent resistance, flexibility, and membrane formability.

Polyimide resins can be synthesized via condensation polymerization of diamines and diphthalic anhydrides, which release small molecules such as H_2O during chemical reactions (**Figure 2.5**) [40]. The uncontrollable release of condensable small molecules makes obtaining defect-free polyimide thin-films from direct monomer synthesis difficult. The use of a solvent mitigates the problem [40]. The monomers can be either directly polymerized into polyimides or synthesized into a poly(amic acid), followed by imidization into polyimides [65]. Polyimide is a copolymer with a phthalimide ring connected to the dianhydride. For instance, Matrimid®5218 is a copolymer of 5(6)-amino-1-(4-aminophenyl)-1,3,3-trimethylindane (DAPI) and 3,34,4-benzophenone tetracarboxylic dianhydride (BTDA). This type of polyimide has outstanding physicochemical properties and excellent thermal stability (Tg > 315 ℃) due to the rigid imide group. Besides, the high intrinsic selectivity of polar gas molecules over other gas species makes this commercial polyimide a promising candidate for many gas separation applications.

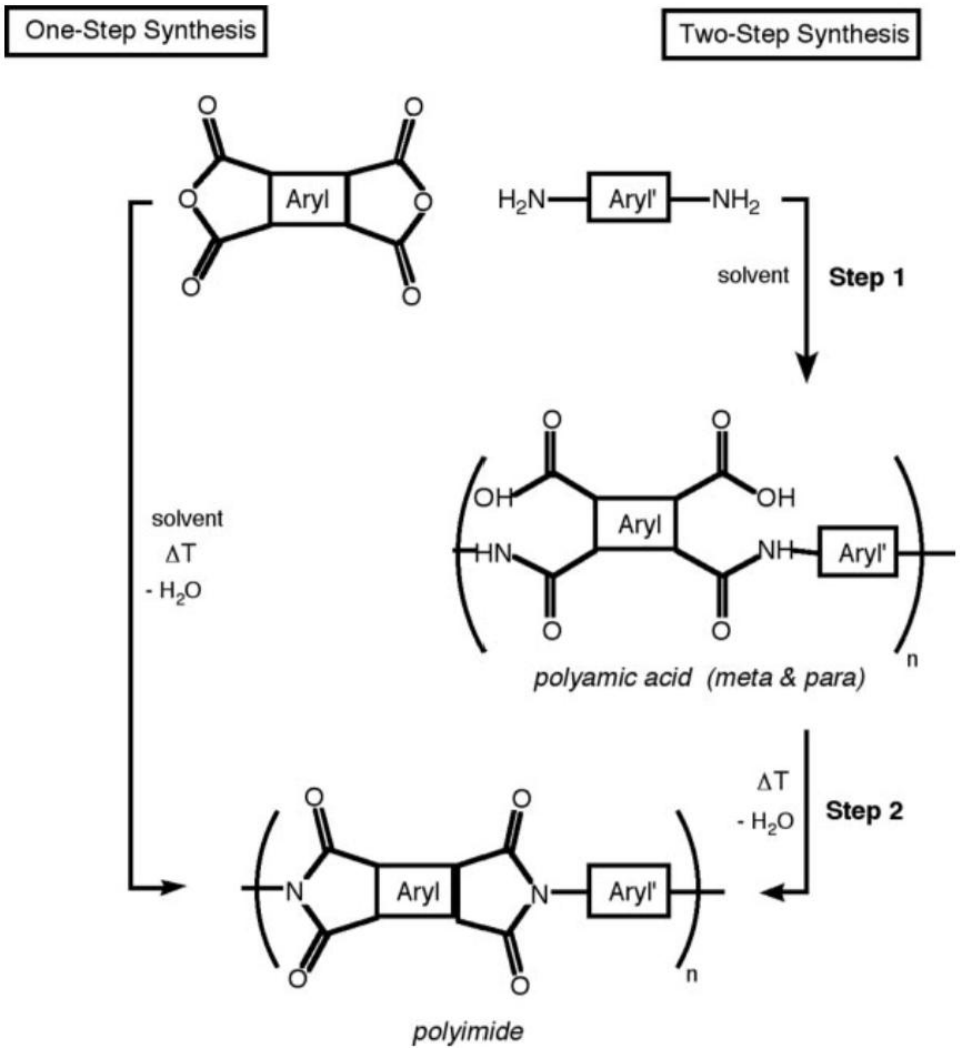

Figure 2.5 Typical synthesis routes of heterocyclic polyimide resins [66].

From the perspective of molecular engineering, the flexibility in the chemical synthesis of polyimide materials allowed tremendous advancement in gas separation membranes [59, 67-70]. However, due to the physiochemically stable nature of polyimide, the development of a new type of polyimide for gas separation faces challenges in balancing the gas separation performance and processability of the polyimide-based membranes [38, 40, 64, 69, 71]. From the perspective of membrane fabrication, the polyimide resins could be fabricated into thin-films via phase inversion or solvent evaporation methods.

However, the increasing demand for environmental-friendly membrane fabrication requires reducing or eliminating the use of harsh organic solvents [69], making it difficult to process polyimide-based resins with intrinsically high physicochemical and thermal stability. It was recognized that using liquid or melting processable monomers to directly polymerize and fabricate defect-free polymeric membranes without using any solvents might hold great promise in reducing the use of harsh organic solvents [69]. Developing new membranes from heterocyclic polymer systems based on addition polymerization, i.e., PPN, might be a potentially sustainable way to fabricate next-generation gas separation membranes. However, no publications were available for gas separation membranes based on PPN-based materials.

2.2.3 Relationship between microstructure characteristics and gas permeation behavior of polymeric membranes

The gas permeation behavior of polymeric membranes is mainly dependent on their microstructure characteristics [72]. In principle, polymeric materials comprise mobile polymer chain segments [73]. The randomly packed polymer chain segment can accommodate small molecules, such as gas molecules, in the intermolecular space, conceptionally called free volume [74-76]. At the same time, the movement of polymer chains creates a pathway for the migration of gas molecules inside the polymeric membrane [62].

The packing and mobility of the polymer chain segment are the key factors for gas transportation through a dense polymeric substance [62, 72]. For rubbery polymers, the

high mobility of the polymer chain allows faster diffusion of gas molecules inside the membrane. For glassy polymers, the intermolecular distance between the polymer chain and intrinsic sub-nanovoids created by the insufficient packing of polymer dominates the gas transport behavior. **Figure 2.6** demonstrates the general relationship between glass transition temperature related to polymer chain mobility and free volume related to intrinsic vacancy inside the polymeric solid substance [77]. The high extent of polymer chain rigidity and excess free volume in glassy polymer allows high gas selectivity and permeability of the glassy polymer membranes.

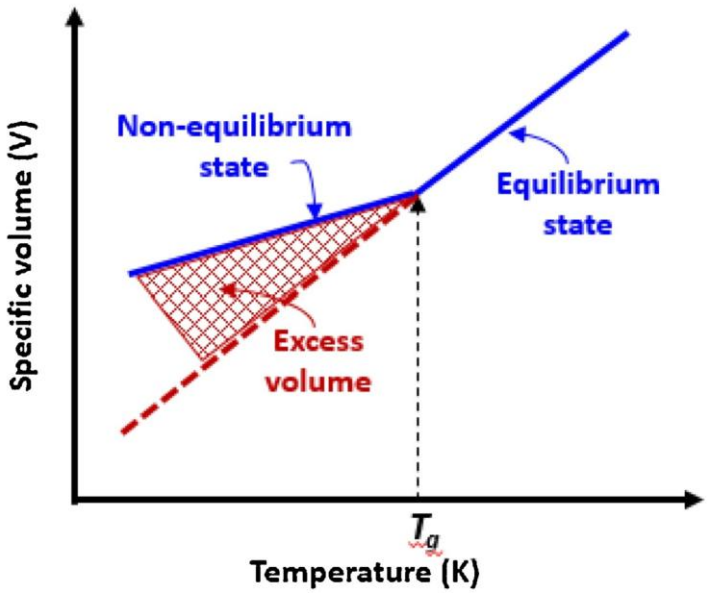

Figure 2.6 Relationship between glass transition temperature and free volume [77].

As polyimide holds a great share of the market in membrane gas separation, it becomes important to modify commercially available polyimide to enhance its intrinsic gas transport properties. Chung's group [72] summarized that the diffusion and solution of gas molecules in polymeric membranes mainly depend on intermolecular distance and

free volume characteristics, respectively. Moreover, the intrinsic free volume distribution and gas affinity of the polymer matrix are critical to achieving high gas diffusivity selectivity and solubility selectivity. The adjustment of microstructure characteristics of membranes plays an essential role in developing precise pore size distribution of the membrane materials to achieve high separation performance of molecules with a size difference of less than 0.1 nm. An enormous effort has been made to improve gas separation performance by exploring new membrane material designs [34, 37, 78, 79]. Gas permeability and selectivity of glassy polymeric membranes can be improved by the adjustment of the intermolecular space of the polymer matrix [76]. Incorporating a bulky side group with low electron affinity can enlarge the free volume of polymers, thereby improving the gas separation performance of membranes [80, 81]. More recently, incorporating rigid and twist polymer chain units enabled the design of polymers of intrinsic microporosity [34, 73, 82, 83]. The improvement in the amount of free volume brings the gas permeability of PIM membranes about 3-4 orders of magnitude higher than conventional polyimide membranes [84, 85]. Nonetheless, considerable investment and time are required to design new polymer systems and translate polymeric materials into practical membranes [34]. Furthermore, the physical and chemical stability of newly designed materials might not always match the need for practical use [59, 69].

The polymer blending method is a promising way to create new materials by combining commercially available polymers with high-performance polymers to enhance the gas transport properties of membranes [86]. Mixing polymeric materials with distinct properties can impart new microstructure characteristics to the blend [87]. Numerous polymers have already been designed and published, and the opportunity to combine two

or more polymers into a new system can be considered endless [86]. However, due to thermodynamic limitations, the polymer pairs require molecular structural compatibility or strong intermolecular interactions to form fully miscible blends [88]. In general, polymer blends can be classified by their miscibility into three groups: miscible (homogeneous), partially miscible, and immiscible (heterogeneous) [86]. The permeability of a homogeneous blend membrane (no phase separation) follows the prediction of semi-logarithmic law:

$$\ln P_B = \emptyset_1 \ln P_1 + \emptyset_2 \ln P_2 \tag{2.1}$$

where P_B, P_1 and P_2 are referred to the permeability of the blend and pure polymer membranes, $\emptyset_i$ to the volume fraction of polymer 1 and polymer 2, respectively. The selectivity of a homogeneous blend membrane can be predicted following the general rule of the semi-logarithmic equation:

$$\ln\left(\frac{P_1}{P_2}\right) = \emptyset_1 \ln\left(\frac{P_1}{P_2}\right) + \emptyset_2 \ln\left(\frac{P_1}{P_2}\right) \tag{2.2}$$

The permeability of heterogeneous (phase-separated) blend membranes is difficult to predict by the semi-logarithmic equation. The phase separation behavior of most polymer blend systems resulted in distinct gas permeation behavior compared to homogeneous polymer blend systems. The Maxwell equation is often utilized to predict the gas permeation behavior of the heterogenous (immiscible) blend membranes. This model assumes that the dispersed polymer phase with spherical droplet-like morphology is

uniformly distributed in the continuous phase. Maxwell's equation for gas permeability is described as:

$$P_b = P_c \left[\frac{P_d+2P_c-2\emptyset_d(P_c-P_d)}{P_d+2P_d+\emptyset_d(P_c-P_d)}\right] \quad (2.3)$$

where P_b refers to the permeability coefficient of the blend, P_c and P_d are to the continuous and dispersed phases, respectively. $\emptyset_d$ is referred to the dispersed phase's volume fraction. Bruggeman model is another empirical model that can predict gas transport properties of heterogenous blends. This model is based on a similar assumption of continuous and dispersed phases like the Maxwell equation, but it differently assumes the morphology of the disperse phase is ellipse instead of the spherical droplets. Bruggeman model is described as follows:

$$P_b = P_c \left[\frac{\frac{P_d}{c}-\frac{P_b}{P_c}}{\emptyset_c\left(\frac{P_d}{P_c}-1\right)}\right]^3 \quad (2.4)$$

where $\emptyset_c$ is the continuous phase's volume fraction.

Apart from morphology, the miscibility between the two components generally plays an important role in fine-tuning the gas separation performance of polymer blend membranes. There is little doubt that the thermodynamically miscible nature of polymer pairs is the key to the predictable gas separation performance according to additive law [58, 86, 87]. However, it was identified that it was difficult to overcome the selectivity-

permeability trade-off relationship by the blending of typical polymers with moderate gas separation performance below the Robeson upper bound relationship. In contrast, immiscible blends of polymers with moderate gas separation performance may possibly create new blends with superior gas separation performance. For instance, when the less permeable but more selective PBI forms a continuous phase in the blend, the dispersed phase of more permeable PI can improve the gas permeability of the blend (**Figure 2.7**). On the contrary, when PI forms the continuous phase, the dispersed phase of more selective PBI can only slightly enhance the gas selectivity of the blend membrane [86, 89]. The miscibility of the immiscible polymer blend membranes can be improved by adding compatibilizers [89, 90]. It was speculated that the compatibilizer would be released from the compatibilized blend membranes during the membrane fabrication process, altering the free volume characteristics of the membranes to achieve superior gas separation performance over model predictions. The true reason for this phenomenon is unclear; however, it becomes more practical to design high-performance membrane materials from commercially available polymers with gas separation performance lower than the Robeson upper bound relationship [89]. The polymer chain arrangement and intermolecular interaction between the two components become more critical to achieving an outstanding polymer blend membrane for gas separation. Many studies have reported that the synergistic effect of the partially miscible polymer blend system may bring unexpected gas performance, which will be discussed in ***Chapter 6.1*** in detail. In short, the polymer blend method has become one of the promising approaches to overcoming the trade-off challenge in gas separation.

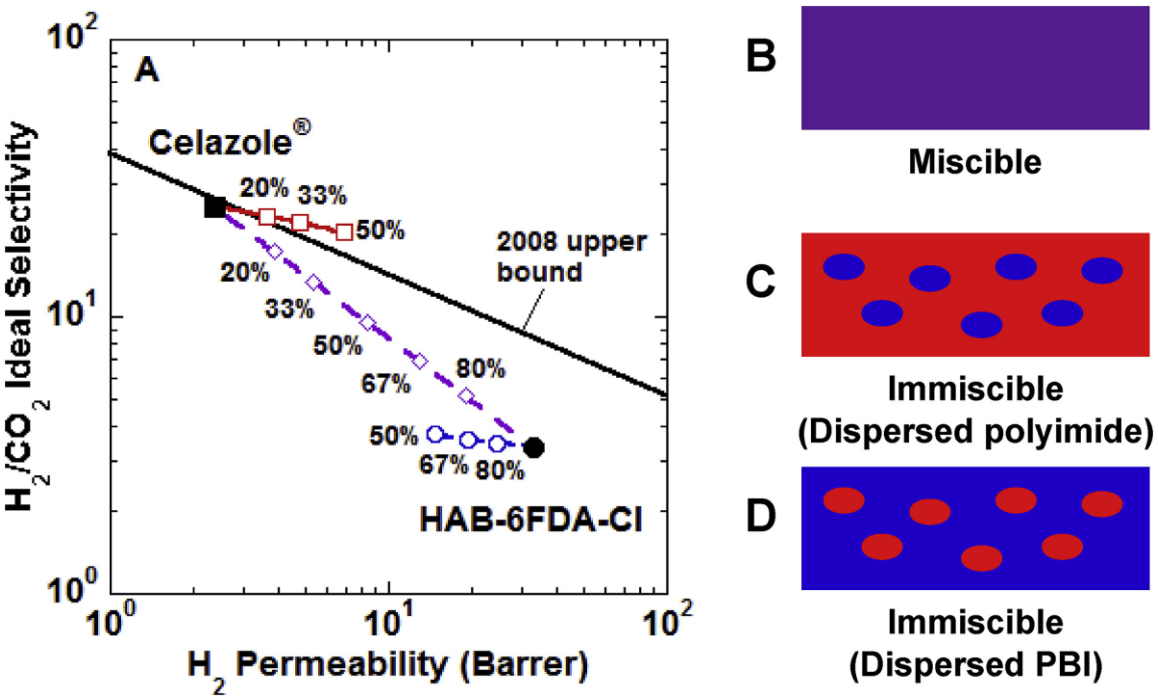

Figure 2.7 Additive model and Maxwell model for PBI/PI blends comparing to Robeson upper bounds [89]. (Percentage represents the concentration of HAB-6FDA-Cl in the Celazole(PBI)/HAB-6FDA-Cl(PI) blend; the dashed line with diamond represents the prediction of ideal gas separation performance by additive model; the solid line with square and short dash line with circle represent the prediction of ideal gas separation performance by Maxwell model.)

2.3 Carbon molecular sieve membranes derived from polymeric materials

Carbon molecular sieve membranes have been historically studied for their promising gas separation performance and excellent chemical and mechanical stabilities [69]. Scientifically, a carbon membrane that follows molecular sieving behavior can be categorized as a carbon molecular sieve membrane (**Figure 2.8**) [91]. The smaller micropores (ultramicropores, < 7 Å) provide the molecular sieving ability to molecules with similar size, while the larger micropores (> 7 Å) enable gas molecules to transport in

ways of surface diffusion or Knudsen diffusion, which gives gas selectivity equal to the square root of inverse molecular weight ratio of gas pairs ($\alpha_{1/2} = (M_2/M_1)^{0.5}$) [69]. Adjusting microstructure characteristics, especially ultramicropores, is critical to developing high-performance carbon molecular sieve membranes for fractionating small gas molecules.

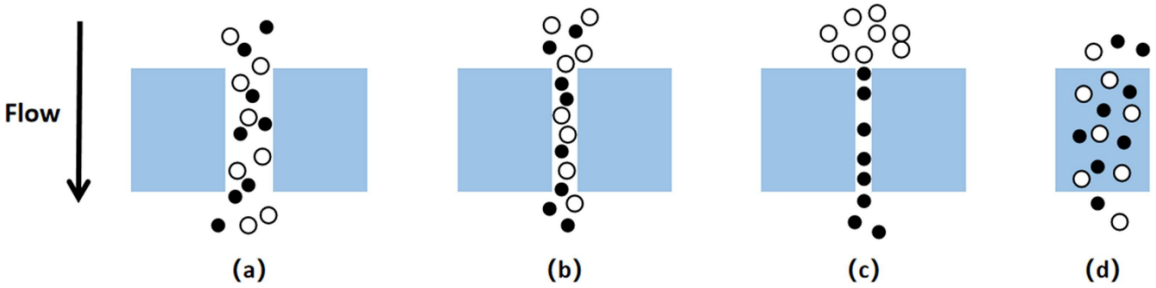

Figure 2.8 Typical gas transport mechanisms through porous, microporous, and dense membranes [91]. (a) bulk pore flow; (b) Knudsen flow; (c) molecular sieving; (d) solution-diffusion.

CMSM membranes are generally fabricated from the pyrolysis of polymer materials below its graphitization temperature (c.a. 1500 ℃) to form turbostratic carbon with amorphous microstructure (**Figure 2.9**) [69, 92]. Intuitively, the pyrolysis temperature plays a vital role in the microstructure characteristics and gas separation performance of the membranes. The higher pyrolysis temperature generally leads to higher gas selectivity but lower permeability (**Figure 2.10**) [49, 69, 93]. This effect is mainly due to the increased extent of carbonization, which narrows the microporosity of carbon materials at higher pyrolysis temperatures. In addition to the pyrolysis process, the intrinsic thermal stability of polymer materials is also a critical factor in microstructure characteristics and gas separation performance of carbon molecular sieve membranes. Different types of

thermally stable polymeric precursors and the gas separation performance of the obtained carbon molecular sieve membranes will be reviewed in ***Chapter 2.3.1***. The state-of-the-art understanding of the microstructure characteristics of carbon molecular sieve membranes will be reviewed in ***Chapter 2.3.2***.

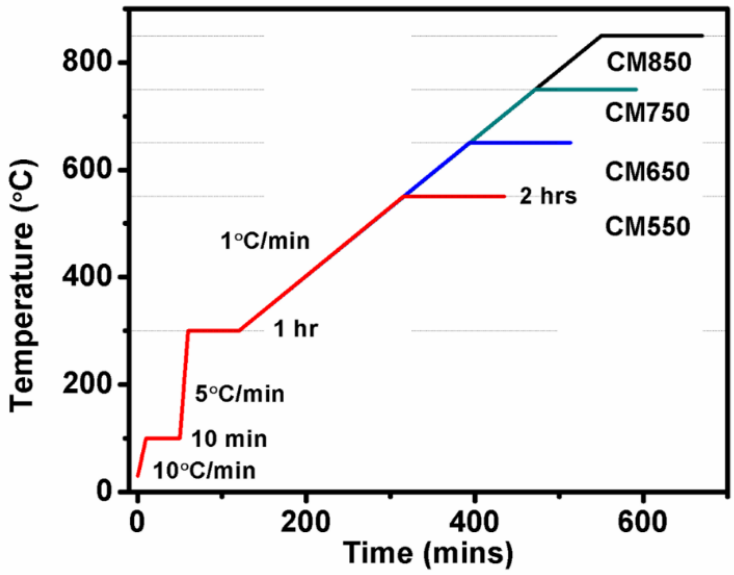

Figure 2.9 Schematic of typical pyrolysis protocol of carbon molecular sieve membranes [49].

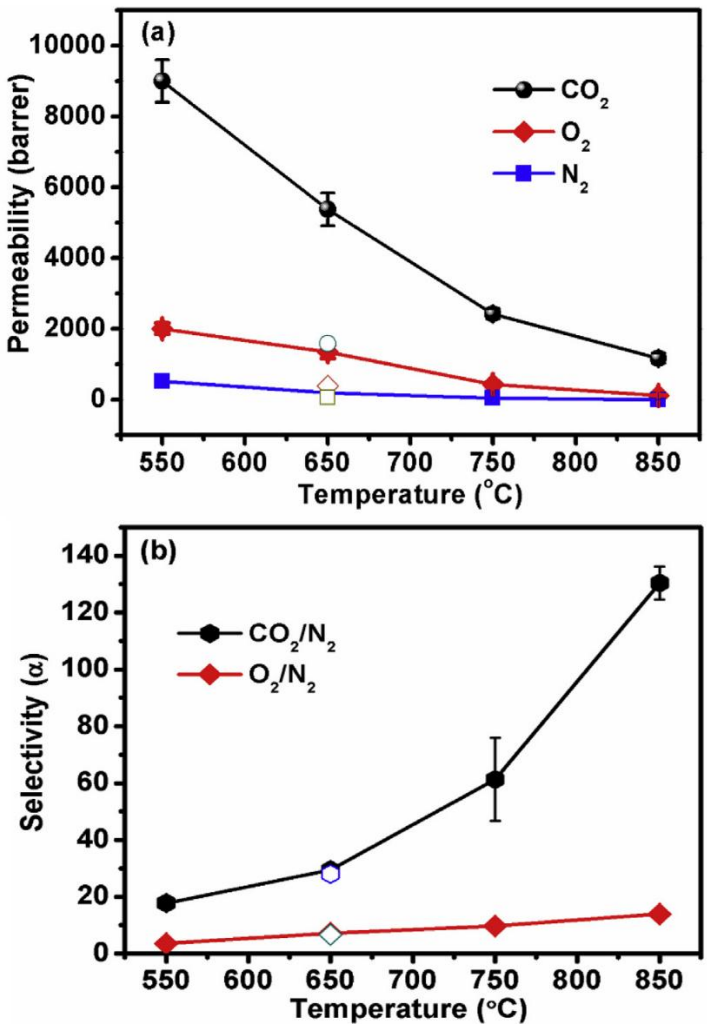

Figure 2.10 The effect of pyrolysis temperature on gas separation performance of carbon molecular sieve membranes [49].

2.3.1 Carbon molecular sieve membranes derived from low and high-decomposition temperature polymers

The thermal stability of polymeric materials largely determines the microstructure and gas permeation properties of the derived carbon molecular sieve membranes [94]. Early researchers discovered that the pyrolysis of thermosetting polymers with low decomposition temperature (i.e., which start to decompose below 400 ℃) could obtain

amorphous carbon molecular sieve membranes, which possessed improved gas separation performance in comparison to their polymeric counterparts [69]. In addition, the low decomposition temperature thermosetting polymer resins, such as PFA and PR, are generally both melting and solvent processable, giving excellent processability for membrane fabrication [69, 95]. Nonetheless, the gas separation performance of carbon molecular sieve membranes derived from low decomposition temperature polymers was generally below the state-of-the-art Robeson upper bound relationships for gas separation membranes [69]. The high glass transition temperature of polymeric materials is considered to benefit the conversion of the free volume of the precursor into microporosity of the derived microporous carbon (**Figure 2.11**) [49]. However, there is a lack of thermosetting polymer resins that possess high decomposition temperatures for fabricating carbon molecular sieve membranes.

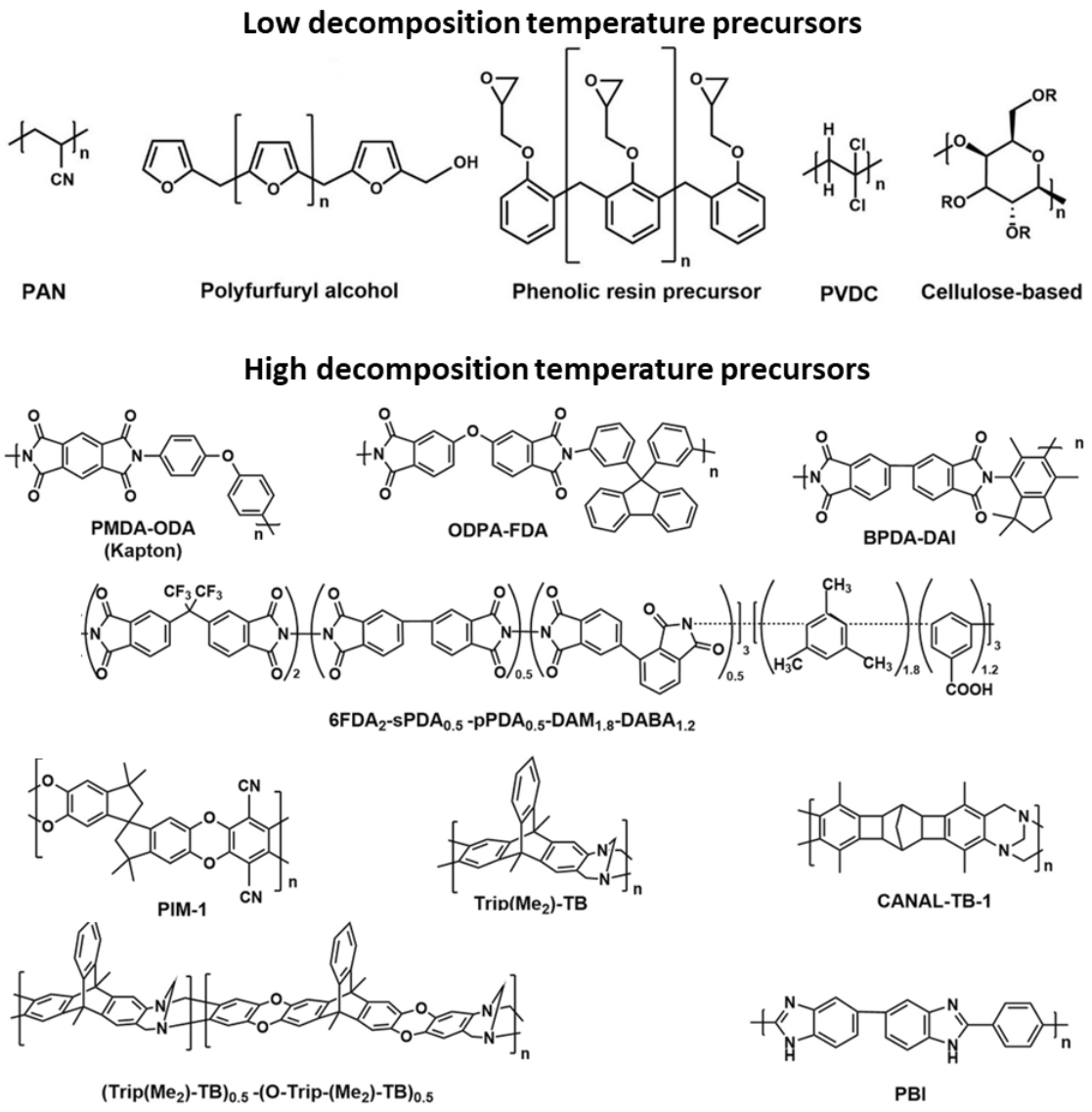

Figure 2.11 Typical high decomposition temperature polymeric precursors for carbon molecular sieve membranes [69].

The rigid and thermally stable molecular chain structure, typically heterocyclic rings with nitrogen atoms, of high decomposition polymers benefits the formation of more microporous carbon materials [69, 92, 94, 96, 97]. Therefore, carbon molecular sieve membranes derived from high decomposition temperature heterocyclic polymer precursors generally have superior gas separation performance (**Figure 2.12**) [69].

Polyimide is one of the most studied polymeric precursors for carbon molecular sieve membranes [69, 92, 94, 98-100]. Like many high-decomposition polymers, polyimide possesses heterocyclic rings that provide excellent thermal stability and chain rigidity. However, the high chain rigidity of polyimides generally leads to insufficient solubility in many organic solvents, challenging the development of high-performance polyimide materials with good processability [38, 40]. There is a need to explore high decomposition temperature heterocyclic resin as a precursor with both flexibility in molecular designs and good processability for developing high-performance carbon molecular sieve membranes.

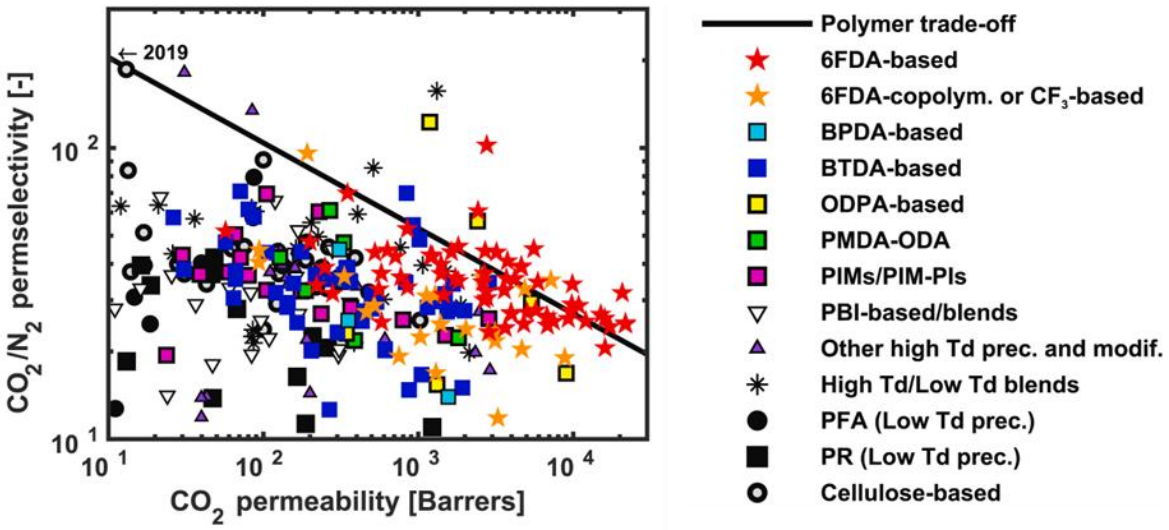

Figure 2.12 Gas separation performance of the state-of-the-art carbon molecular sieve membranes derived from various polymeric precursors [69]. (PI: polyimide; PBI: polymer of intrinsic microporosity; PBI: polybenzimidazole; PFA: poly(furfuryl acid); PR: Phenolic resin)

2.3.2 Envision the microstructure arrangement of carbon molecular sieve membrane

Many researchers have intensively studied the microstructure arrangement of carbon molecular sieve membranes to understand the complicated transition of polymeric materials into a carbonaceous matrix (**Figure 2.13**). Koresh and Soffer [95, 101] first developed a defect-free microporous carbon membrane obtained from thermosetting polymers or resins in the 1980s. They provided clear evidence that the gas separation performance of microporous carbon membranes can far exceed Knudsen diffusion selectivity. The intrinsic microporosity of carbon materials was able to be applied to gas separation in the context of the membrane to fractionate gas pairs with a size difference at the 0.1 nm level.

In 1992, Hatori *et al.* [102] first developed carbon molecular sieve membranes from thermoplastic polyimide (Kapton) thin-films with superior gas separation performance than those obtained from thermosetting resins. Since then, polyimides have gained tremendous interest in fabricating high-performance carbon molecular sieve membranes. In 1994, Jones and Koros [70] further developed fluorinated polyimides as precursors for fabricating high-performance carbon molecular sieve membranes in hollow fiber configuration. In 1997, Suda and Haraya [103] observed an interconnected “slit-like” microporous carbonaceous network derived from polyimide (Kapton) via TEM. In 2003, Steel and Koros [104] proposed that carbon molecular sieve membranes are composed of a dual model pore size distribution with micropores (0.7 to 2.0 nm) and ultramicropores (0.3 to 0.7 nm) (**Figure 2.13(a)**). They hypothesized that CMS membranes derived from

linear polymers (e.g., polyimides) could form amorphously packed carbon nanosheets with dual-mode pore distribution contributed from intra- and inter nano-sheets microstructures. In 2017, they further proposed that these carbon nanosheets might form "walls" and "cells" like microstructures that explained the high gas permeability and selectivity of polyimide-based carbon molecular sieve membranes (**Figure 2.13(b)**) [99, 105]. The micropores constructed by inefficient packing of carbon nanosheets might create "cell" like microstructure as a rapid pathway for gas diffusion. Meanwhile, ultramicropores constructed from intrinsic intermolecular space in between carbon strands in carbon nanosheet "wells" might serve as molecular sieving sites. Koros' group [106, 107] further identified the existence of "orphan carbon strands" derived from linear polymers (i.e., polyimides) that played an important role in forming a continuous microporous carbonaceous matrix contained isolated "cells" (**Figure 2.13(c)**). More recently, in 2023, Lively's group [98] proposed and demonstrated an alternative carbon microstructure model known as "nanoribbon" microstructures, which was first described by Jenkins and Kawamura back in 1976 [108] as ultramicropore domains instead of "wells-cells" microstructure in Koros' theory for polyimide-derived carbon molecular sieve membranes (**Figure 2.13(d)**).

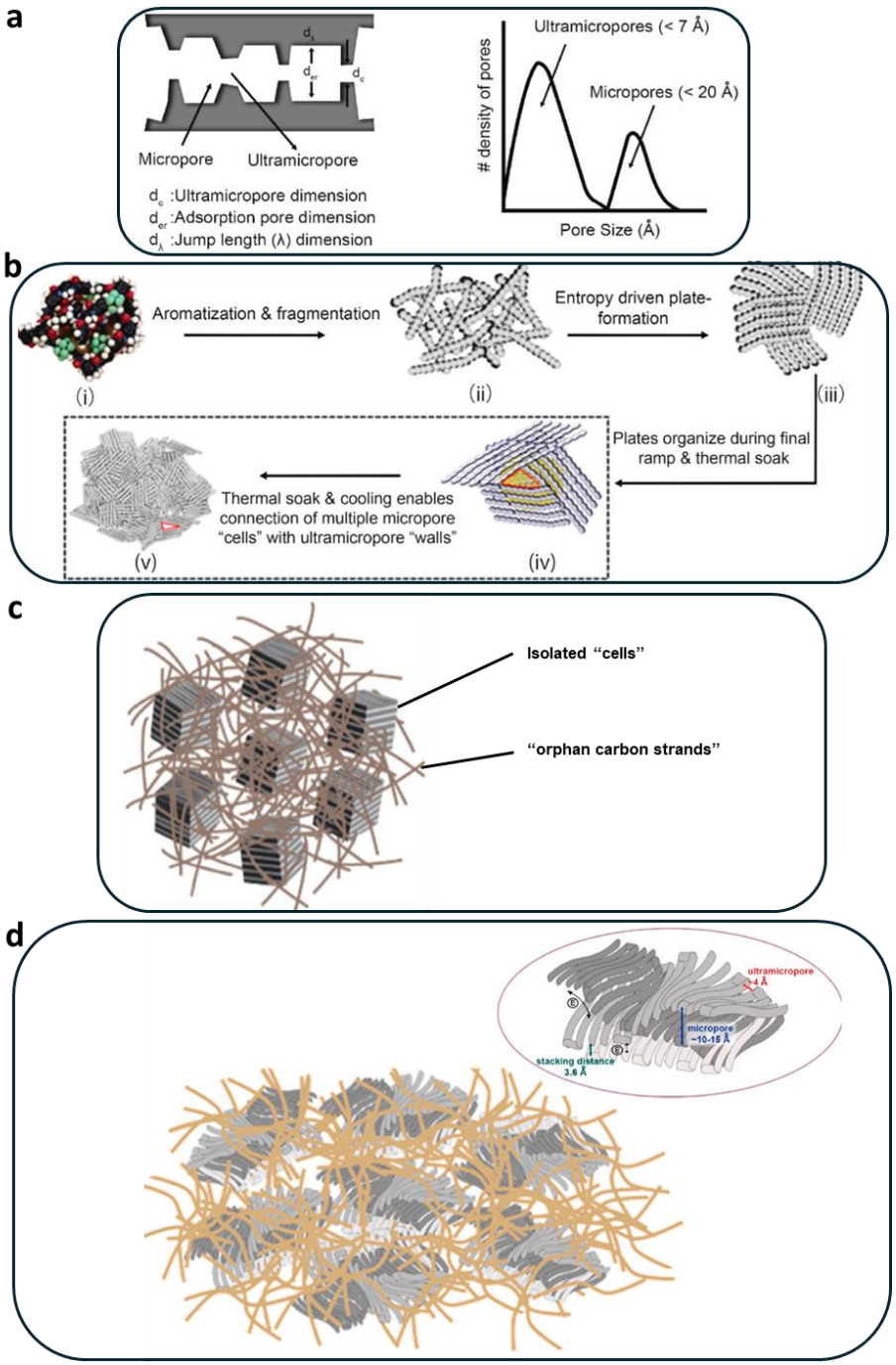

Figure 2.13 Hypothetical microstructure arrangement models of carbon molecular sieve membranes [69]. (a) Bimodal distribution characteristics of carbon molecular sieve [104]; (b) "walls" and "cells" like microstructure constructed by carbon strands and nanosheets [99, 105]; (c) continuous"orphan carbon strands" and isolated "cell" model proposed by Koros' group [106, 107]; (d) "nanoribbon" instead of "cell" structure in continuous "orphan carbon strands" proposed by Lively's group [98].

In short, the in-depth understanding of the microstructure arrangement of carbon molecular sieve membranes was mainly based on microporous carbon materials derived from linear polymers (especially polyimides). As previously discussed in ***Chapter 2.1.2***, however, there is limited insight into microstructure characteristics and gas permeation behavior of microporous carbon materials derived from thermosetting heterocyclic PPN resins with high decomposition temperatures.

2.4 Identified gaps in literature that will be addressed by this thesis

Despite the rapid development of phthalonitrile resin and the derived carbon materials for various applications, PPN has yet to be explored as an advanced membrane material for separation. This study pioneered the investigation of the potential of PPN and its derived carbon materials as advanced membrane materials on gas separation. For this purpose, it is essential to investigate the microstructure characteristics and gas permeation behavior of PPN and the derived carbon materials. Previous work has identified the intermolecular interactions that enable the stacking of molecular chains of PPN networks; however, there is a lack of understanding of the adjustment methods for the microstructure arrangement of resorcinol-based polyphthalonitrile networks. The molecular arrangement of the PPN network is also a key factor determining the microstructure characteristics of the PPN-derived carbon materials, which was generally overlooked in previous literature. Furthermore, it should be noted that no published literature on gas permeation behavior or gas separation performance of polymeric or carbonaceous membranes based on PPN is available. This study aims to provide a fundamental understanding of the gap between the

microstructure characteristics and gas permeation behavior of PPN and the derived carbon membranes.

Chapter 3

Experimental Methodology

Resorcinol-based polyphthalonitrile and its derived carbon materials were developed in the context of membranes to investigate their gas permeation behavior. Furthermore, various characterization techniques were adopted to understand the roles of thermal, chemical, and microstructure in adjusting microstructure characteristics of membrane materials based on PPN. This chapter summarizes the chemical synthesis, membrane fabrication, and carbonization methods and briefly introduces the characterization techniques for identifying the properties of PPN-based polymeric and carbon materials.

3.1 Design of Experiments

The adjustment of microstructure characteristics of polymeric and carbon materials largely determines the gas permeation behavior of the membranes. The first part of this study focuses on the adjustability of microstructure arrangement and gas permeation behavior of PPN and its derived carbon materials by means of metal-ion doping or curing treatment. The second part of this study investigates the relationship between microstructure characteristics and gas permeation behavior of PPN-based polymeric and carbon molecular sieve membranes. The third part of this study explores the potential of PPN as an advanced membrane material to modify microstructure characteristics and the gas separation performance of typical polymeric gas separation membranes.

The experiments start with testing the hypothesis that the microstructure arrangement and gas permeation behavior of resorcinol-based phthalonitrile and its derived carbon materials can be adjusted via metal-ion doping or thermal treatment. Following this, the PPN precursors subjected to various thermal histories were fabricated into carbon molecular sieve membranes to demonstrate the effect of the molecular arrangement of the precursor on the microstructure characteristics of the derived carbon materials. Lastly, PPN was incorporated into polyimide to investigate its electron donor/acceptor properties on modifying microstructure characteristics and gas separation performance of the blend membranes. Thermal treatment on the blend membranes was also carried out to investigate the extent of adjustability of PPN as an advanced membrane material for gas separation.

3.2 Chemical and reagents

3.2.1 Synthesis of resorcinol-based phthalonitrile monomer (1,3-bis(3,4-dicyanophenoxy)benzene)

Resorcinol-based phthalonitrile monomer (1,3-bis(3,4-dicyanophenoxy)benzene, 362.34 g/mol) was synthesized from a modified literature method [3, 6]. Briefly, monomers of resorcinol (99%, 110.11 $g \cdot mol^{-1}$) and anhydrous potassium carbonate (99%, 138.21 $g \cdot mol^{-1}$) from Sigma-Aldrich, and 4-nitrophthalonitrile (98%, 173.13 $g \cdot mol^{-1}$) from Tee Hai Chemical, at a molar ratio of 1:3:2, were added into dimethyl sulphoxide (DMSO, 99%, Sigma-Aldrich) and stirred for at least 24 hours under a inert atmosphere at ambient temperature, followed by precipitation from dilute hydrochloric acid solution (Tokyo Chemical Industry) and purification by washing with deionized water at least three times.

3.2.2 Prepolymer synthesis

Polyphthalonitrile (PPN) was synthesized using a solvent-based polymerization method, and the detailed steps can be found in the literature [109]. In brief, PPN was synthesized from 1.0 mol of resorcinol-based phthalonitrile monomer and 0.03 mol of diamine catalyst, 1,4-bis(4-amino phenoxy)benzene (98%, Tokyo Chemical Industry), in N-methyl-2-pyrrolidone (NMP, 99%, Sigma-Aldrich) at 190 °C. The obtained PPN mixture was purified with a 0.45 um polytetrafluoroethylene syringe filter, adjusted to 15 wt% in NMP, and stored in ambient condition before further use. The synthesis of metal-ion-doped PPN prepolymer followed the same synthesis protocol with the predetermined ion-to-monomer ratio of 1:4.

3.2.3 Preparation of supported PPN membranes, supported PPN-CMS membranes and free-standing thin-films

To enhance the mechanical robustness of carbon thin-films derived from polymeric precursors [9, 110], a porous alumina substrate has been utilized to provide mechanical support for the membranes [100, 110, 111]. The supported PPN membrane was fabricated by coating the PPN solution on a disc-shaped porous alumina substrate (Fraunhofer Institute for Ceramic Technologies and Systems, thickness: 1.0 mm, diameter: 3.0 cm, mean pore size: 200 nm) using a spin coater (LEBO science) (**Figure 3.1**). The spinning rate was controlled at 1500 rpm, and a spinning time of 10 mins was used. The spin coating was repeated 3 times to prevent any pinhole or crack that led to a non-selective carbon membrane [112]. The samples were vacuum-dried at 80 ℃ overnight to obtain the supported PPN membranes. PPN and PPN-CMS membranes were fabricated in a continuous and progressive heating protocol modified from the literature in a tube furnace (Carbolite Inc.) with argon as the protective atmosphere at a flow rate of 200 cm^3(STP)/min [5, 9, 49]. Briefly, the PPN membranes were progressively cured at 220 ℃, 250 ℃, and 280 ℃. The cured PPN membranes were named by their final curing temperature; for instance, PPN280 for the membrane obtained at 280 ℃. The PPN280 was further cured at 325 ℃ to obtain PPN325, followed by curing at 400 ℃ to obtain PPN400. The soaking time for each curing step was 120 mins. The ramping rate was controlled at 5.0 ℃/min below 400 ℃. The supported PPN-CMS membranes were directly carbonized after the curing steps of the PPN membranes in the tube furnace. In order to prevent any cracks from the supported carbon membranes [100], slow temperature ramping rates were programmed at 1.0 ℃/min from 400 ℃ to 475 ℃, and

0.5 ℃/min above 475 ℃ without any soaking until reaching the final pyrolysis temperature at 550 ℃ or 750 ℃. The soaking time at the final pyrolysis temperature was 120 mins. The PPN-CMS membranes were named by their final carbonization temperature; for instance, PPN280-CMS550 for the PPN280 membrane pyrolyzed at 550 ℃. The membranes were collected after naturally cooling down to room temperature. The metal-ion-doped PPN and PPN-CMS composite membranes were cured and pyrolyzed as described above. The PPN thin-films were obtained by casting the PPN solution on an aluminum foil plate. The center part of the thin-films with uniform thickness (~130 μm) was used for further thermal treatment and characterization. PPN and PPN-CMS thin-films were cured and pyrolyzed as described above.

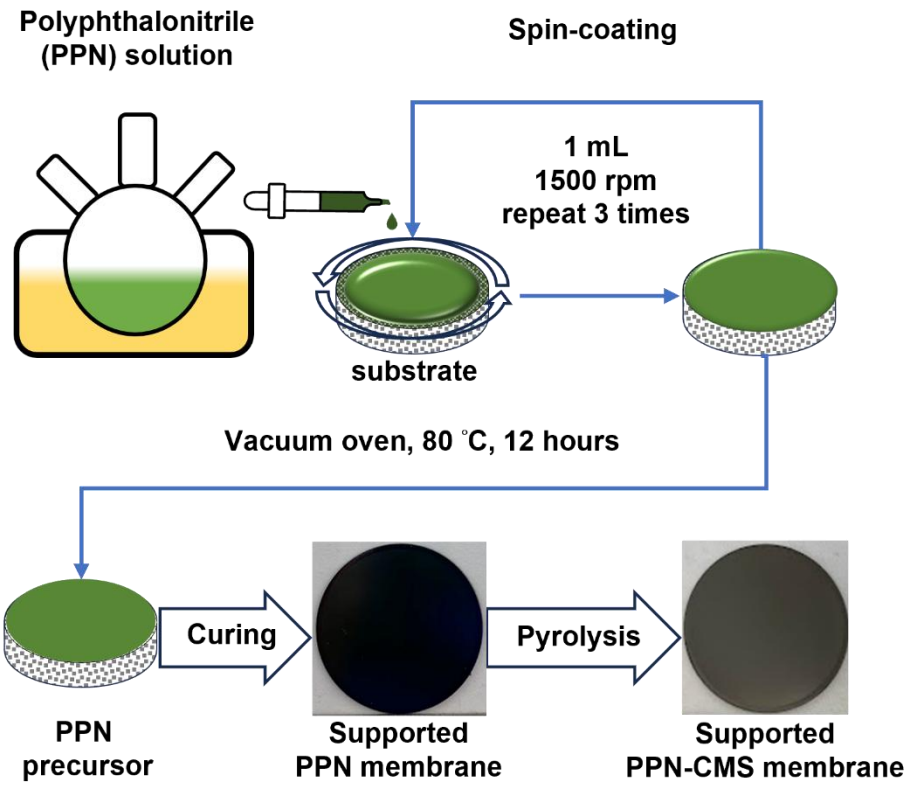

Figure 3.1 Schematic diagram of the fabrication process of supported PPN and PPN-CMS membranes.

3.2.4 Preparation of free-standing membranes

Free-standing dense membranes were fabricated from blends of high-performance commercial polyimide (PI, Matrimid 5218, Alfa Aesar) via the solvent evaporation method. Briefly, 15 g PI was first dissolved in 85 g NMP, followed by mechanical stirring for 24 hours at ambient temperature. The obtained 15 wt% PI solution was degassed by sonication for 1 hour and placed stationary for at least 24 hours. A different amount of 15 wt% PPN solution was added to the PI solution and vigorously stirred for 24 hours to form a homogeneous PPN/PI blend mixture. The mixtures were degassed again and kept for another 24 hours. The doping solution was cast on a smooth glass substrate by a casting knife with a 500 μm gap. The transparent film was carefully placed in a dry oven at 80 ℃ for 48 hours. After the evaporation of most of the NMP, the film was placed into deionized water until it was detached from the glass plate. The membranes were then punched into round thin films of 3.5 cm diameter. All the samples were secured and sandwiched between two PTFE-glass fiber plates with a 1 mm gap for further trace solvent removal at 140 ℃ under vacuum for 48 hours. The blend membranes were then thermally annealed in a box oven for a sequence of predetermined temperatures, i.e., 220 ℃, 250 ℃, 280 ℃, and 325 ℃ for 2 hours at each stage. The thermally treated membrane was named as PPNx/PIy-z; x is for the composition of PPN, y is for the composition of PI, and z is for the final thermal treatment temperature.

3.3 Instrumentation and Characterization Techniques

The main experimental approach is to perform gas permeation analysis to obtain ideal gas permeability and selectivity properties of membranes. The theoretical background for this experimental approach has been discussed in the literature review. The specific details of the experiment will be discussed in this chapter. This article will also briefly review other instrumentation and techniques used to characterize the microstructure properties of membrane materials.

3.3.1 Rheometer

The viscosity (apparent shear viscosity) of the PPN solution was measured by a rheometer (TA instrument, Discovery HR-3) using the parallel plate method. The viscosity was obtained as a function of shear rate in ambient conditions. The viscosity represents the internal flow resistance of the fluid (polymer solution). For the parallel plates method, the shear rate (1/s) is defined as the velocity of the mobile plate divided by the gap between parallel plates. The shear stress (N/m^2 or Pa) is defined as the force applied to the mobile plate divided by the area of the plate. The viscosity (Pa·s) is obtained from the shear stress divided by the shear rate.

3.3.2 Gel Permeation Chromatography (GPC)

Gel permeation chromatography analysis (1260 Infinity, Agilent Technologies) was utilized to obtain molecular weight distribution of PPN prepolymer using polystyrene as

standard. A gel permeation column contains molecular sieves with tortuous pathways. The smaller molecules or polymer chains can travel into the extra pathways, but the molecular sieves reject the larger ones. As such, the larger molecules come out the permeate side first, followed by smaller ones. A molecular weight distribution can be obtained from GPC analysis for a polymer system containing numerous molecules with various molecular weights. A number or weight average molecular weight can be used to represent the molecular weight of the polymer. The number average molecular weight (M_n) is defined as the arithmetic average of the molecular weights of the individual molecules. The weight average molecular weight (M_w) prioritizes the mass fraction of molecular weight, and it can be defined as the summation of the product of the mass fraction to the molecular weight of each molecule. The mass fraction represents the ratio of the total mass of each type of molecule (with different molecular weights) to the total mass of the polymer. The molecular weight distribution (polydispersity, PDI) of a polymer is defined as the ratio of M_n to M_w.

3.3.3 Fourier-transform Infrared Spectroscopy with attenuated total reflectance (FTIR-ATR)

The Fourier transform infrared (FTIR) spectrum is obtained by absorbing appropriate infrared light energy from various molecular bonding structures in materials that produce intermolecular vibration and rotation modes. FTIR can obtain the vibrational spectrum of compounds from the Fourier transform of the interference spectrum.

The position of the measured wavenumber can indicate the functional group of a polymer. The measured wavenumber range of the infrared spectrometer is from 4000 cm^{-1} to 400 cm^{-1}. The wavenumber ranges from 4000 to 1300 cm^{-1} and is known as the 'functional group region', which is mainly the stretching vibration of single bonds containing hydrogen atoms, various double bonds, or triple bonds. The wavenumber range from 1300 to 400 cm^{-1} is called the 'fingerprint area.' Except for isomers, each compound has its own specific spectra pattern, like a human fingerprint. Based on the same principle, FTIR-ATR uses an attenuated total reflectance technique to characterize the chemistry of bulk membrane samples or thin-film composite membranes at the near-surface region without breaking the membrane structure.

3.3.4 UV-Vis spectrometer

UV-Vis spectrometer (Lambda 950, Perkin Elmer) was utilized to characterize the optical properties of membranes. The electrons in molecular substances can absorb the energy of light to jump from molecular orbitals with lower energy to ones with higher energy, resulting in characteristic absorption peak(s) for the material. The change in the energy gap can cause a shift in the absorption peak position(s) of the substance. In the UV-Vis spectrum, the higher wavenumber (lower frequency) of light indicated the lower energy absorbed by the molecular substance. A shift in the position of the absorption peak in the spectrum reflects a change in molecular interactions associated with electronic energy gaps.

3.3.5 Gravimetric Analysis

The gel fraction of the membranes was studied using the gravimetric method. A given amount of thin film was weighted (W_i) before being immersed in NMP for three days. The residue of the membranes was filtered out, dried in an oven, and weighed with filter paper. Gel fraction was calculated from the residue's net weight (W_o) from the Eq. (3.7):

$$Gel\ fraction\ (\%) = \frac{Wi - Wo}{Wi} * 100\ \% \quad (3.7)$$

3.3.6 Thermogravimetric Analysis (TGA)

Thermogravimetric analysis is to study the thermal degradation behavior of a material. Generally, the thermal degradation behavior can be described as the function of sample mass against temperature. Q500 thermogravimetric analyzer (TGA, TA Instruments) with software was utilized to reveal the thermal degradation behavior of polymeric materials. An inert atmosphere, such as nitrogen, can prevent exaggerated oxidation of polymeric materials during the analysis. That is to say, the analysis revealed the pyrolysis behavior of the polymer in carbonized materials. The analysis was performed with a 5 ℃/min heating rate at a temperature range from 50 to 900 ℃ in a nitrogen atmosphere with a 50 ml/min flow rate.

3.3.7 Dynamic Mechanical Analysis (DMA)

Dynamic mechanical analysis (DMA) is a convenient technique that can be utilized to estimate molecular chain mobility or rigidity of polymers in terms of glass transition temperature. The glass transition temperature of a polymer can be defined as the maximum tangent delta, the ratio of storage modulus over loss modulus, of a polymer under stress oscillation mode. Dynamic mechanical analyzer (DMA Q800, TA Instruments) was conducted with the heating rate of 5 C/min up to 500 ℃ under ambient conditions for determining the glass transition temperature of polymeric thin-films.

3.3.8 Polarized Light Microscopy (PLM)

A polarized light microscope (PLM, Olympus TH4-200) was utilized to visualize the miscibility behavior of the PPN and polyimide blend membranes. The light filter (polarizer) allows light to be polarized at a given planar axis when randomly oriented incident light passes through. The polarized incident light can distinguish the molecular arrangement of polymeric materials at the micrometer level. Generally, the randomly distributed molecular arrangement for amorphous polymeric materials allows lights in all orientations to pass through, showing no strong interference of polarized incident light. This is the same case for homogeneous polymer blends containing miscible polymers due to the randomly distributed molecular chain arrangement of the blend. Specifically, for heterogeneous polymer blends containing partially miscible or immiscible polymeric materials, differences in molecular arrangement due to the incompatibility of polymer chains can create distinct orientations and, thus, induce strong interference and

differences in light intensity. Therefore, the polarized light can depict the phase separation behavior of heterogeneous polymer blend materials.

3.3.9 Field Emission Scanning Electron Microscopy (FESEM)

Scanning electron microscopy (SEM) is an important and simple method for observing the structural characteristics of membranes. SEM technique can directly observe the surface and cross-section of the membrane to visualize morphological properties, such as pore morphology, film symmetry, and skin layer thickness of membranes. Field Emission Scanning Electron Microscopy (FESEM, JEOL JSM-6340F) was utilized to observe the microstructure of the membranes.

Due to the plastic nature of polymer materials, it is easy to destroy the original shape of the film subjected to mechanical treatment (i.e., cutting, slicing, or fracturing), resulting in the inability to observe the true structural form. In order to mitigate the issue, the polymeric membranes were immersed in liquid nitrogen to rigidify the polymer matrix at low temperatures, and the sample was directly fractured for further use. It should be noted that the polymer materials themselves are not conductive. The polymeric membrane is typically prone to charge accumulation, leading to morphological distortion. Meanwhile, the membrane is affected by high-energy electron beams, which may also lead to changes in the physical and chemical structure of polymer materials. Therefore, prior to SEM analysis, a thin layer of conductive metal, i.e., platinum, was sputtered on the surface of the polymeric specimen to eliminate those effects. Besides, slicing and

breaking must be performed during sample preparation when using SEM to observe the cross-sectional structure of the membrane.

3.3.10 Transmission Electron Microscopy (TEM)

Transmission Electron Microscopy (TEM, JEOL 2100F) with an accelerating voltage of 200 kV was utilized to observe the microstructure. Polymer and carbon thin-films were shattered and dispersed in ethanol. The specimen was prepared by collecting the fine powders on a copper grid with carbon mesh. In principle, TEM utilizes a beam of high-voltage electrons to hit a specimen. This allows the electrons with small de Broglie wavelength to reveal the molecular or atomic arrangement of materials at the sub-nanometer level. When the beam of electrons transmits through the solid material, some electrons bump with atoms of the specimen to create a transmission image. The transmitted electron image can reflect the molecular arrangement of a specimen, of which the more atom distribution allows the less transmitted electrons to generate less intensity region, and vice versa.

3.3.11 X-ray Diffraction (XRD)

X-ray diffraction scattering analysis (XRD) was utilized with a D8 Advance X-ray diffractometer (Bruker) to identify microstructure characteristics of the membrane. Diffraction occurs when X-rays enter neatly repeating arrangements of atoms. When the X-ray beam enters different crystal planes, optical path difference is formed from the different X-ray traveling paths. Assume that the crystal plane distance is *d*, and the

incident angle θ is the angle between the incident light and the crystal plane. When the incident light is reflected by the upper and lower crystal planes, the two reflected lights have an optical path difference $2dsin\theta$. When the optical path difference is equal to an integer multiple of the X-ray wavelength, the constructive interference of X-rays is formed. For amorphous polymeric or carbon materials, the intermolecular space between molecular chains can be described by Bragg's law, which was applied to calculate the average molecular chain distance or d-spacing values [49, 98]:

$$d = \frac{n\lambda}{2sin\theta} \tag{3.3}$$

where d refers to the average molecular chain distance (d-spacing value), n is a natural integer (equal to 1 for amorphous polymer), λ equal to 1.5418 Å is the wavelength of Cu-Kα radiation source, and θ is the degree of diffraction angle.

3.3.12 Positron Annihilation Lifetime Spectroscopy (PALS)

Positronium (Ps) is a combined state of a positron and an electron. Ps are like atoms that have many unique properties and some that are similar to hydrogen. Importantly, their atomic radius derived from the Schrödinger equation is exactly the same as that of hydrogen atoms. Ps include 1^1S_0 (para-positronium, p-Ps) and 1^3S_1 (ortho-positronium, o-Ps), two ground states. Since the wave functions of electrons and positrons overlap to a certain extent, Ps has a probability of self-annihilation. The p-Ps annihilation releases two γ photons, and the o-Ps annihilation releases three γ photons. The intrinsic lifetime of p-

Ps and o-Ps are 0.125 ns and 142 ns, respectively. The lifetime of o-Ps in condensed materials is only a few nanoseconds, which is much shorter than its intrinsic lifetime. In other words, the positron and the electron in the material annihilate to release two gamma photons. When a positron enters a substance, the positron self-annihilation (free positron annihilation) occurs when it is close to the electron. Characteristic γ-rays will be produced after the annihilation, a typical phenomenon of mass conversion into energy—the more defects in the material, the greater the rate of positrons being captured by defects. Because the positron annihilation rate is proportional to the electron density at the annihilation site, it is very sensitive to electron density distribution. Since the defect in the material lacks a positively charged atom, it is electronegative so that positrons will be more easily captured in the defect. Therefore, the positron lifetime is related to the defect size (< 1 nm). The larger the hole, the lower its electron density, and the chance of positron annihilation is relatively reduced. Positron annihilation lifetime spectroscopy (PALS) can be used to detect the size, number, and distribution of defects in materials. PALS is one of the positron annihilation spectroscopic analysis techniques. It uses the radioactive source ^{22}Na to perform β^+ decay to generate positrons. The generated positrons enter the sample and are captured by holes or free volumes in the sample, resulting in annihilation. The lifetime of a positron from generation to annihilation is closely related to the size of the hole in the material. PALS can be used to explore the number, size, and size distribution of micropores or free volumes within gas separation membranes. PALS analysis characterizes the annihilation of o-Ps to obtain free volume characteristics and pore size distribution of the polymeric or carbon materials [49, 100, 113-115]. The theoretical diameter of positronium is the same as that of a hydrogen atom

(1.06 Å), which is much smaller than that of the gas molecule (i.e., N_2 or CO_2) for gas adsorption analysis [116].

Briefly, a ^{22}Na (20 μCi) positron source with Kapton foil support was used between two specimens (~ 1 mm thickness) for the collection of 1.0×10^6 counts to obtain the positron annihilation lifetime (PAL) spectrum. Positron lifetime components and intensities were obtained by fitting the PAL spectrum using PATFIT software, while MELT software was employed to analyze the PAL spectrum for positron lifetime and pore size distribution. The o-Ps lifetime (τ_3) was correlated with the cavity radius (R) of the CMS by the semiempirical formula based on the infinitive potential spherical model [113, 115, 117]:

$$\tau_3 = 0.5 \times \left[1 - \frac{R}{R+\Delta R} + \frac{1}{2\pi}\sin\left(\frac{2\pi R}{R+\Delta R}\right)\right]^{-1} \quad (3.4)$$

3.3.13 Gas Adsorption and Porosity Analyzer

The gas adsorption method is a relatively mature and widely used method to determine the pore size distribution of mesopores and micropores. CO_2 adsorption analysis at 273 K and cryogenic N_2 adsorption analysis at 77 K were carried out using a gas sorption and porosimeter analyzer (ASAP 2020, Micromeritics) with software provided. Based on the adsorption characteristics of gas on the solid surface, microstructure characteristics of the membranes on the pore size and pore distribution of mesoporous and microporous materials can be obtained. The gas adsorption method porosity distribution measurement utilizes the capillary condensation phenomenon and the principle of volume equivalent

substitution, that is, the amount of condensed gas in the measured hole is equivalent to the volume of the hole. The adsorption theory assumes that the shape of the pores is a cylindrical tubular single distribution or a molecular sieve slit-shaped wide distribution. Different shapes are assumed to have different gas adsorption and desorption behaviors, thereby establishing a capillary condensation model. The pore size distribution of carbon membranes was evaluated using density functional theory (DFT) by assuming a slit pore in the microporous carbon.

The inert N_2 has become the most commonly used adsorbate because it is easy to obtain and has good reversible adsorption characteristics. The N_2 adsorption method is generally suitable for testing mesopore and micropore materials between 0.5 and 300 nm. It uses the isothermal adsorption characteristic curve of nitrogen to determine pore size distribution. At the liquid N_2 temperature, the amount of N_2 adsorbed on the solid surface depends on the relative pressure of nitrogen (P/P_0). P is the partial pressure of N_2, and P_0 is the saturated vapor pressure of N_2 at liquid N_2 temperature. When the P/P_0 value increases, the pore radius where condensation can occur also becomes larger. Owing to the CO_2 molecule having a much smaller kinetic diameter than N_2, the CO_2 molecule can easily access smaller micropores or ultramicropores. Besides, the high saturate pressure of CO_2 allows the analysis to be operated at higher temperatures (273K), giving the high diffusion ability of CO_2 molecules into micropores. These advantages make CO_2 adsorption analysis suitable for characterizing microporous carbon materials with abundant ultramicropores.

3.3.14 Gas Sorption Analyzer

The gas sorption test for hydrogen, nitrogen, and carbon dioxide was carried out using a setup containing a temperature-controlled stainless steel cell with microbalance (Cahn D200) [49]. The polymer thin-films with 0.1 cm^3 in volume were loaded onto a carrier pan. The same volume of the aluminum plate was placed on another carrier pan to correct the buoyancy effect. The test was conducted at a given temperature of 35 ℃ and absolute pressure of 2 atm, the same as the gas permeation test. Before starting the gas sorption experiment, the cell was vacuumed for at least 8 hours after loading to ensure the complete removal of dissolved gases in the samples. The selected gas was then purged into the cell, and the weight was recorded after the gas sorption at equilibrium. The solubility coefficient (*S*) was derived from the Eq. (3.5):

$$S = \frac{C}{p} \tag{3.5}$$

where C is referred to gas sorption amount (cm^3(STP))/(cm^3), and p is to the applied pressure. According to the solution-diffusion model, the diffusivity coefficient (*D*) can be calculated from the Eq. (3.6):

$$D = \frac{P}{S} \tag{3.6}$$

where *P* is referred to the gas permeability in a commonly used gas unit, Barrer ($1 \cdot 10^{10}$ Barrer = 1 cm^3(STP) ·cm/cm^2·s·cmHg), and *S* is described above.

3.3.15 Gas Permeation Analyzer

Gas permeation analysis was based on constant pressure and variable volume method [100]. Due to the relatively low permeance of polymeric membranes, a gas permeation analyzer (GTA-11MH, Yanaco) equipped with gas chromatography (G2700, Yanaco) was employed to determine the pure gas permeability (P) of N_2, O_2, CO_2 ,and H_2 for the free standing or supported polymeric membranes [100]. The permeability of supported carbon membranes were measured in a customized testing cell (effective membrane area of 3.8 cm^2) using a soap film flowmeter (SCal Plus) [56, 118]. The membranes were tested freshly to avoid physical or chemical aging effects. The following equation determines the permeability:

$$P = \frac{q \cdot k \cdot l}{\Delta p \cdot A \cdot t} \tag{3.1}$$

where P is described above, q to the amount of permeate gas volume (cm^3), k is the correction factor, l to the selective layer thickness of the membrane (cm) (determined by SEM), A to the effective membrane area (cm^2), t to collection time (s) in the steady-state of permeation, the analysis was conducted at 25 ℃ under a pressure difference (Δp) of 152 cmHg (2.0 atm). The H_2/CO_2 (50:50 mol%) mixed-gas permeation analysis was performed at 35 ℃ and the pressure difference in the 2 - 8 atm range. Permeability values were expressed in Barrer (SI unit: 10^{-10} cm^3 (STP) cm/(cm^2·s·cmHg)). Ideal gas selectivity or permselectivity (S) was calculated as the ratio of permeability coefficients,

and its relationship to solubility selectivity (the ratio of solubility coefficients) and diffusivity selectivity (the ratio of solubility coefficients) can be described as follow:

$$S_{1/2} = P_1/P_2 = \frac{S_1}{S_2} \cdot \frac{D_1}{D_2} \quad (3.2)$$

3.4 Sources of Experimental Errors

The uncertainty in this article mainly comes from the measurement of the samples during the permeation study. It mainly involves the unpredictable random permeability variations generated by gas permeation analysis [119]. If the gas permeability of a membrane was low (i.e., N_2 permeability of PPN membrane), the gas permeability measurement requires sufficient sampling time for permeate gas collection. Any gas leakage during this stage could affect the measured result. In order to minimize the uncertainty, vacuum grease was applied to the sealing rubber that directly contacted the membrane in the testing cell to prevent gas leakage from the edge of the membrane. The gas permeability was measured three times from individual samples, with uncertainties expressed as ± standard deviation (σ). Systematic errors can be minimized by carefully calibrating the instrument before taking measurements. To be specific, standard polyethylene terephthalate free-standing thin film with a known permeability was utilized to identify the accuracy of the gas permeation analyzer. The gas permeation analyzer was calibrated to the level of uncertainty within a 10% difference of the standard thin film.

Chapter 4

Adjusting microstructure of PPN and the derived microporous carbon

This chapter demonstrated the adjustment of microstructure characteristics and gas permeation behavior of PPN and its derived carbon materials via metal-ion doping. It was identified that the doping of metal ions can facilitate the formation of more graphitic-like stacking molecular arrangements in PPN networks. The formation of metal-ion-doped heterocyclic phthalocyanine rings was the main reason for the subtle change in the microstructure arrangement of the thermosetting polymer network. Interestingly, the intermolecular stacking distance of the PPN network could be adjusted by different types of metal ions. It was also found that the gas permeation behavior of PPN and the derived microporous carbon membranes largely depend on the microstructure arrangement of the PPN network adjusted by metal ions. This chapter provided new understandings and insights into the adjustability of microstructure arrangement and gas permeation behavior of the PPN network.

4.1 Introduction

The thermosetting resorcinol-based PPN resin has been developed into many high-performance thermal resistant polymers and functional carbon materials since Keller *et al.* [6] first demonstrated the outstanding thermally stability and processibility of resorcinol-based PPN resin in 2005 [3, 5, 13, 17, 120]. The remarkable high char yield of the resin is mainly attributed to the heterocyclic moieties, i.e., isoindolenine, triazine, and phthalocyanine, formed from the addition-polymerization of phthalonitrile moieties [8, 120, 121]. Tay [7] proposed that PPN may possess microporosity, which benefits the formation of microporous carbon materials derived from resorcinol-based phthalonitrile resin. However, Liu [9] demonstrated that the resorcinol-based phthalonitrile network may possess limited or no microporosity due to the interpenetration of linear polymer chains via molecular dynamic simulation. Nonetheless, there was no direct evidence of the existence or absence of microporosity in the resorcinol-based PPN network. A fundamental understanding of the microstructural characteristics of polymer networks is critical for extending PPN-derived polymers or carbonaceous materials into their new applications, such as gas barriers or separation membranes.

Researchers have intensively investigated the microstructure characteristics of various PPN networks and their derived carbon materials. Snow *et al.* [15] demonstrated the aromatic-aromatic stacking nature of a metal-ion-free PPN network. McKeown's group further identified that this kind of stacking generally exists in many polyphthalonitrile systems due to aromatic-aromatic intermolecular interactions between neat phthalocyanine moieties [33-35]. The microstructure arrangement of polyphthalonitrile

can be adjusted by molecular structure design. They demonstrated that silicon-doped phthalocyanines with axial dendritic substituents could enlarge the intermolecular distance of phthalocyanine stacking to 14 Å [122]. It was further identified that incorporating a rigid and twisted (nonlinear) backbone in a PPN network could largely prevent the stacking of phthalocyanine from creating intrinsic microporosity in the polymer systems [35]. The creative molecular design was even able to overcome the stacking of metal-ion (Cu^{2+}, Co^{2+}, or Zn^{2+}) doped phthalocyanine moieties, which possess stronger intermolecular interaction (cation-aromatic interaction) than that of metal-free ones [123]. The carbonization of polymer networks into amorphous carbonaceous materials can produce abundant microporosity. However, previous investigations on PPN-derived carbon materials were not sufficient enough to reveal their microstructure characteristics, which will be discussed in ***Chapter 5.1***. In short, though the molecular arrangement and microporosity of polymer network constructed by phthalocyanine had been widely studied, there is a lack of understanding of microstructure characteristics of PPN network and its derived carbon materials.

This work investigated the adjustability of the microstructure characteristics and gas permeation behavior of the phthalonitrile-derived polymer network (using resorcinol-based PPN as a model) via doping different types of metal ions (i.e., Cu^{2+}, Co^{2+}, and Zn^{2+}) with the predetermined ion-to-monomer ratio of 1:4. It was hypothesized that the doping of different types of metal ions in phthalocyanine moieties could adjust their molecular arrangement and, thus, the gas permeation behavior of the polymeric and carbon membranes derived from the resorcinol-based PPN network containing phthalocyanine, triazine, and isoindolenine. For the first time, this study revealed the

intrinsic microstructure characteristics, gas permeation properties and the microstructural-property relationship of PPN and the derived carbon membranes,. This study not only closed the gap between the hypothesized microporous molecular arrangement of PPN networks and the evolution of microporosity of the derived microporous carbon materials, but also paved the way for the further development of polymeric and carbonaceous membranes based on heterocyclic PPN resins.

4.2 Result and discussions

4.2.1 Chemical, thermal, and microstructure properties of neat PPN and metal-ion-doped PPN networks

The resorcinol-based phthalonitrile resin-derived PPN400 network comprises isoindolenine, triazine, and phthalocyanine moieties as confirmed by FTIR-ATR analysis (**Figure 4.1(a)**). The phthalonitrile groups underwent addition-polymerization to form the heterocyclic moieties [8]. Similarly, the metal-ion-doped PPN400 also produced the same heterocyclic species (i.e., isoindolenine and triazine), while the metal ions could be hosted in phthalocyanine rings [33]. Specifically, the doping of metal ions resulted in smaller wavenumbers of isoindolenine moieties. It was also observed that the peak position and intensities of triazine groups varied with the doped species of metal ions. These phenomena might be due to the introduction of cation-aromatic interactions in the PPN400 network [123]. Interestingly, no apparent difference in peak position was observed in phthalocyanine moieties. However, the UV-Vis spectrum (**Figure 4.1(b)**) further revealed the success of doping metal ions in the phthalocyanine rings. Specifically, the phthalocyanine ring of neat PPN400 exhibited a maximum absorbance

peak at 582 nm. The doping of metal ions resulted in a shift in the absorption peak positions of phthalocyanine [124, 125]. Specifically, the order of absorption peak positions (ZnPPN400 (602 nm) > CoPPN400 (585 nm) > PPN400 (582 nm) > CuPPN400 (582 nm)) is in good agreement with that of neat and metal-ion doped phthalocyanines (ZnPc (687 nm) > CoPc (678 nm) > Free Pc (673 nm) > CuPc (623 nm)) reported in literature [126]. The difference in absorption peak position between the PPN networks and molecular phthalocyanines with or without metal-ion doping might be due to the complex molecular structure of the PPN network in this study, resulting in essential differences in the electronic energy gaps. Nonetheless, the results supported the successful doping of metal ions (i.e., Cu^{2+}, Co^{2+}, and Zn^{2+}) in the PPN400 network.

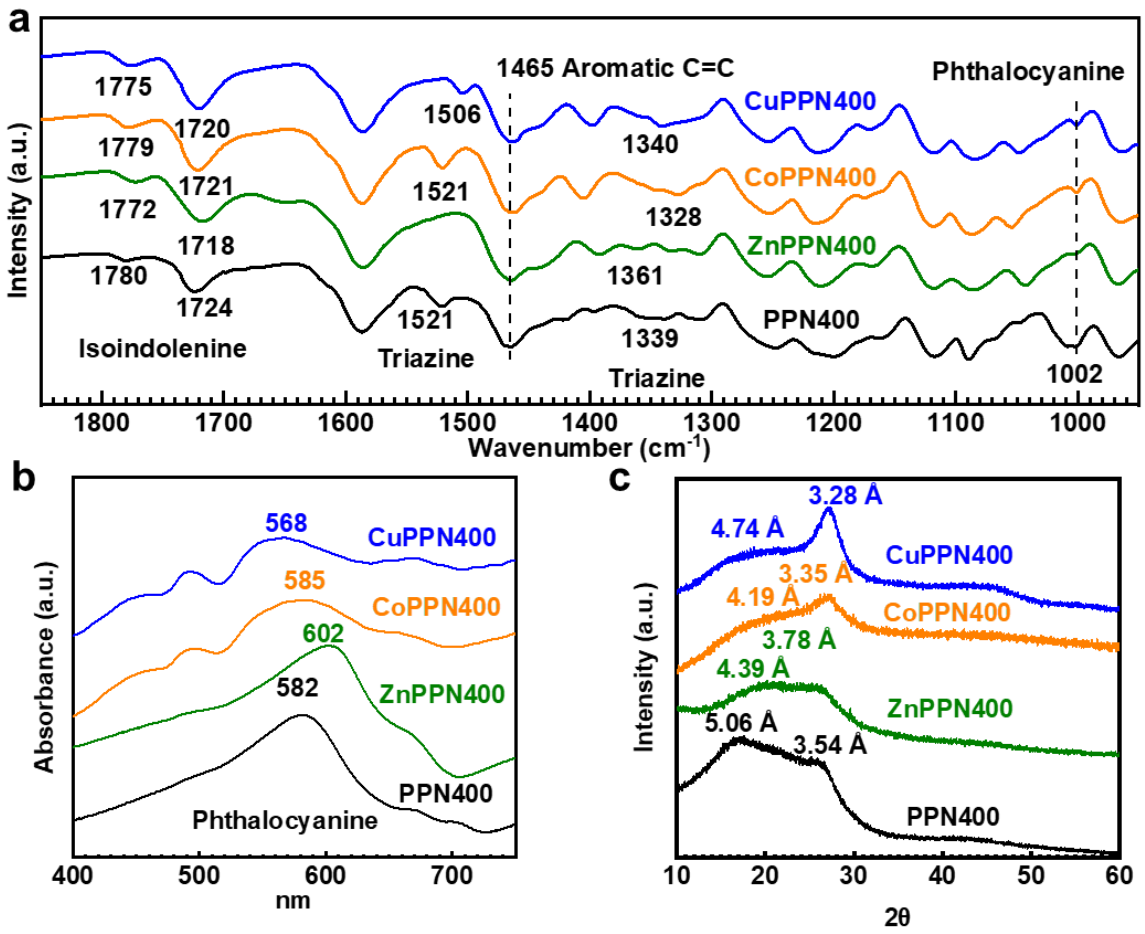

Figure 4.1 Thermal and microstructure properties of neat and metal-ion-doped PPN. (a) FTIR-ATR spectrum of PPN400, CuPPN400, ZnPPN400, and CoPPN400. (b) UV-Vis spectrum, and (c) XRD spectrum of PPN400, CuPPN400, ZnPPN400, and CoPPN400.

It was hypothesized that the doping of metal ions can adjust the molecular arrangement of the PPN network. XRD analysis revealed the general amorphous nature of neat and metal-ion-doped PPN network (**Figure 4.1(c)** and **Table 4.1**). Notably, no sharp and narrow crystalline peak was observed from CuPPN400, CoPPN400, and ZnPPN400. The results indicated that the reaction of PPN monomer with different types of salts was able to form uniform metal-ion-doped phthalocyanine. The neat PPN400 network was observed to have an amorphous region with a d-spacing value of 5.06 Å and a graphite-

like stacking (semicrystalline) region with a d-spacing value of 3.54 Å [5]. Interestingly, the doping of metal-ion in the PPN400 network decreased d-spacing values in the amorphous region compared with the neat PPN network. A plausible reason for the phenomenon was the cation-aromatic interactions introduced in the metal-ion-doped PPN400 networks, resulting in a narrower intermolecular distance. It was also observed that the effect of metal ion types might play a dominant role in adjusting the molecular arrangement of the PPN400 network. The doping of Cu^{2+} and Co^{2+} gave more intense peaks with an average intermolecular distance of 3.28 Å and 3.35 Å, respectively, representing the semicrystalline-like stacking of the derived polymer networks. These results were in good agreement with the d-spacing values of Cu-doped (3.3 Å) phthalocyanine crystal [127] and Co-doped (3.3 Å) phthalocyanine covalent organic framework [128]. However, the doping of Zn^{2+} produced a board hump peak with a d-spacing value of 3.78 Å. The result agreed with the d-spacing value of Zn-doped phthalocyanine thin-film (3.85 Å) in literature [129]. The narrowing of the intermolecular distance of PPN networks doped with Cu^{2+} or Co^{2+} was mainly attributed to the promoted stacking of planar phthalocyanine moieties. In contrast, the nonplanar nature of Zn-doped phthalocyanine might be the reason for the less efficient intermolecular stacking than the other metal-ion-doped PPN400 networks [130]. It was concluded that the molecular arrangement of the PPN network could be adjusted via the doping of metal ions.

Table 4.1 Average intermolecular distance of neat PPN400 and metal-ion-doped PPN400 networks and their derived microporous carbon materials.

Membrane	Precursor		CMS550
	d-spacing (Å)		d-spacing (Å)
	Amorphous	Semicrystalline	
CuPPN400	4.74	3.28	3.46
CoPPN400	4.19	3.35	3.47
ZnPPN400	4.39	3.78	3.90
PPN400	5.06	3.54	4.12

Thermal stability is one of the important factors for PPN-based polymers and carbonaceous materials. All metal-ion-doped PPN400 networks exhibited excellent thermal stability at the same level as neat PPN at 600 ℃ (**Figure 4.2**). This result was mainly due to the formation of thermally stable heterocyclic moieties derived from phthalonitrile groups. Specifically, all metal-ion-doped PPN networks exhibited a more exaggerated thermal degradation around 650 ℃ to 750 ℃. This effect was mainly because of the decomposition of phthalocyanine moieties containing metal ion species [131]. The transition metal ions could be reduced to metallic substances at elevated temperatures, facilitating the decomposition of the metal-ion-doped PPN400 network. Specifically, CoPPN400 showed a more aggressive decomposition above 800 ℃. This might be attributed to the catalytic decomposition of pyrolytic carbon. Overall, both neat and metal-ion-doped PPN400 networks showed sufficient thermal stability in high char yield (> 70%) at moderate pyrolysis temperatures below 800 ℃.

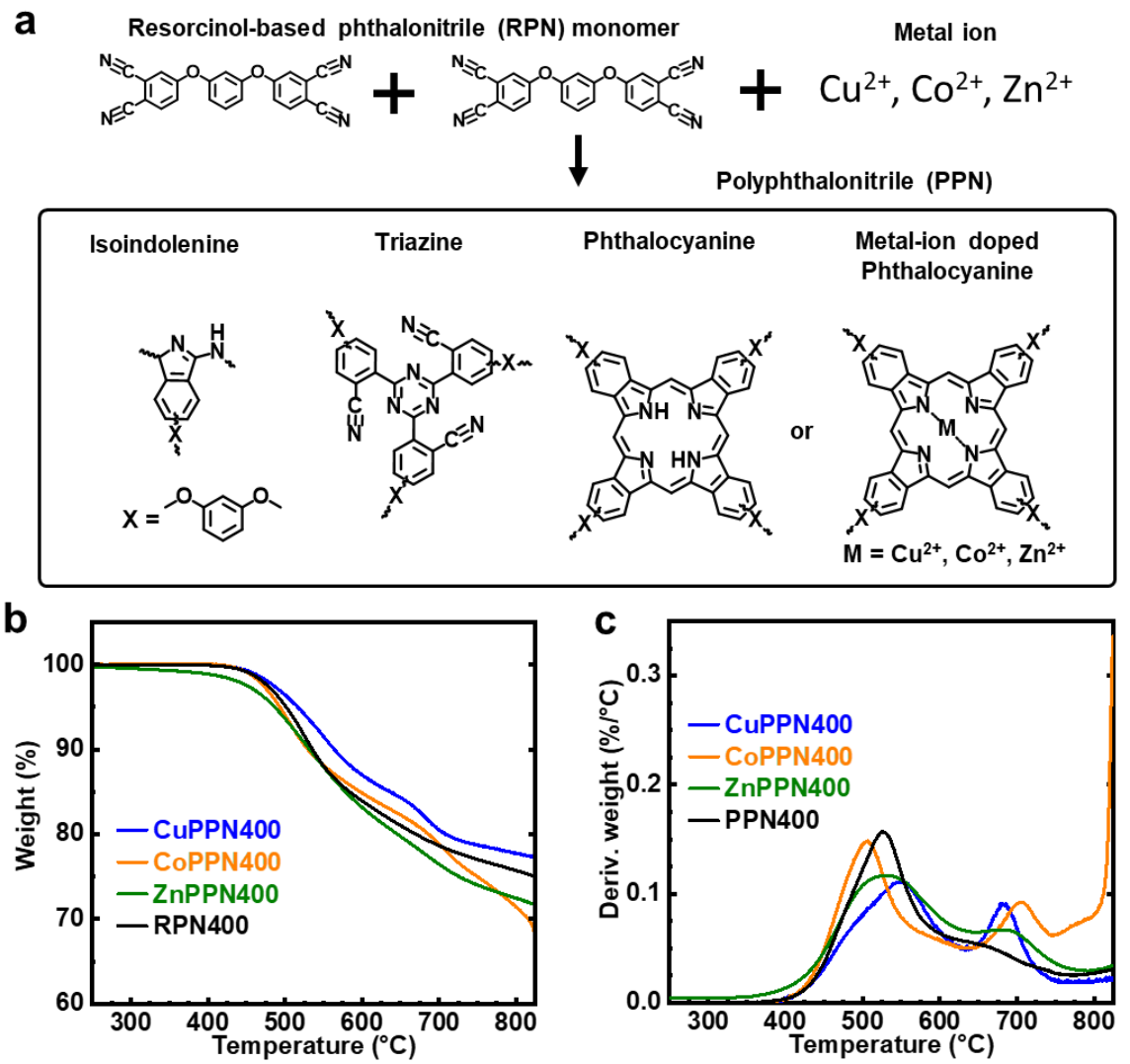

Figure 4.2 Molecular structure and thermal properties of neat and metal-ion-doped PPN400 networks. (a) Schematic diagram of synthesized neat PPN400 and PPN400 doped with Cu^{2+}, Co^{2+}, or Zn^{2+}. (b) TGA and (c) DTG of neat PPN400 and PPN400 doped with Cu^{2+}, Co^{2+}, or Zn^{2+}.

4.2.2 Microstructure characteristics of carbonized membranes derived from neat PPN and metal-ion-doped PPN networks

Table 4.2 Micropore volume of neat PPN400, metal-ion-doped PPN400, and the derived microporous carbon materials from CO_2 adsorption analysis at 273K.

Membrane	Micropore volume (cm^3/g)		
	Precursor	CMS550	CMS750
CuPPN400	0.005	0.074	0.034
CoPPN400	0.005	0.053	0.017
ZnPPN400	0.010	0.093	0.129
PPN400*	0.013	0.080	0.143

The carbonization of neat PPN400 and metal-ion-doped PPN400 networks produced amorphous carbon materials at the pyrolysis temperature of 550 ℃. Interestingly, it was observed that the XRD patterns of carbon materials derived from PPN400 or metal-ion-doped PPN400 networks were somewhat similar to their polymeric precursors (**Figure 4.1(c)** and **Figure 4.3(a)**). Specifically, CuPPN400-CMS550 and CoPPN400-CMS550 possessed a more ordered carbon arrangement with a d-spacing value of about 3.46-3.47 Å (**Figure 4.3(a)** and **Table 4.1**), which might be derived from the semicrystalline polymer chain arrangement of CuPPN400 and CoPPN400 precursors. In contrast, PPN400-CMS550 and ZnPPN400-CMS550 exhibited an entirely amorphous carbon arrangement, similar to amorphous polymer networks of neat PPN400 and ZnPPN400 precursors. The high thermal stability (glass transition temperature > 500 ℃) of neat PPN400 and metal-ion-doped PPN400 networks might be the main reason for this microstructure conversion from polymeric to carbonaceous materials. During thermal

treatment at moderate pyrolysis temperature, the high polymer chain rigidity of the PPN400 network might restrict the movement or rearrangement of the polymer chains, thereby largely inheriting the microstructure arrangement of polymeric precursor in carbonized materials. Hu *et al.* [49] observed similar behavior in the microstructure evolution of microporous carbon materials derived from polyimides with high glass transition temperatures (325 ℃ - 390 ℃). However, it was confirmed that the PPN precursors showed apparently limited or no microporosity from CO_2 sorption analysis (**Table 4.2** and **Figure 4.4**). The results supported the interpenetrating crosslinked PPN network obtained from the molecular dynamic simulation done by Liu [9]. However, the carbon materials derived from neat PPN400 and metal-ion-doped PPN400 networks exhibited bimodal-distributed micropore and ultramicropore structures (**Figure 4.3(b)**). This finding was against the hypothesis proposed by Tay [7] that the microporosity of PPN resin could be converted into the microporosity of the derived carbon materials. In fact, the formation of microporosity of phthalonitrile-based resin might more likely come from the thermal decomposition of functional groups [25]. Meanwhile, the packing of carbon nanosheets converted from PPN might also be beneficial in constructing micropores and ultramicropores of the PPN-derived microporous carbon materials, which will be discussed in ***Chapter 5***. Interestingly, the incorporation of Cu^{2+} and Co^{2+} seemed to narrow the ultramicropore distribution, whereas the doping of Zn^{2+} broadened the ultramicropore distribution in comparison to neat PPN400-CMS550 (**Figure 4.3(b)**). This might be due to the large intermolecular distance of the semicrystalline region of the ZnPPN400 network, leading to the inefficient packing of the derived carbon nanosheets [130, 132]. It shall be noted that pore size distribution analysis via CO_2 sorption had a physical minimal limitation in pore size about 4 Å [133]. Though the true microstructure

evolution of PPN to microporous carbon required further investigation, it was concluded that the microstructure arrangement of carbon materials derived from PPN could be adjusted by the doping of metal ions.

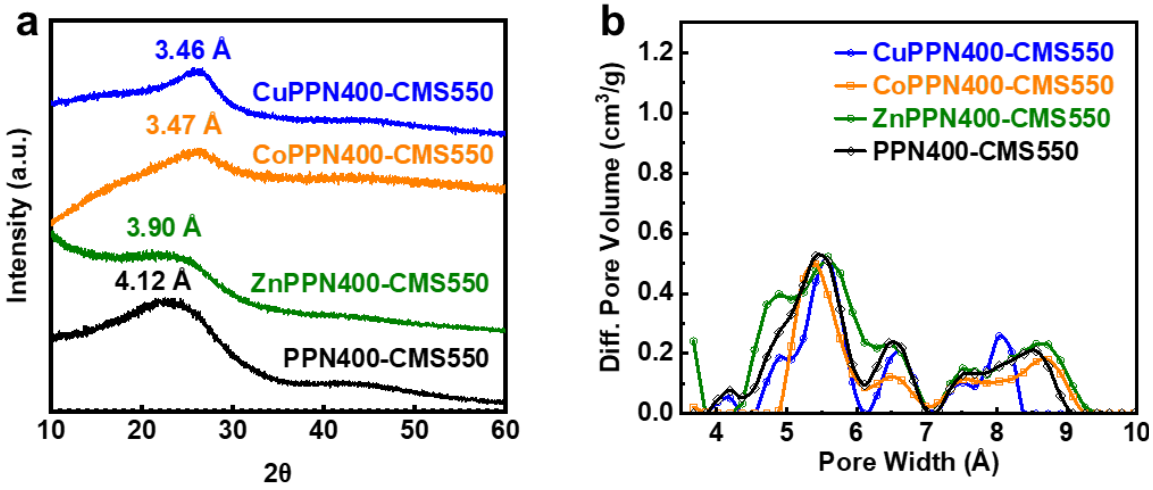

Figure 4.3 Microstructure characteristics of neat PPN400 and metal-ion-doped PPN400 derived microporous carbon materials. (a) XRD pattern and (b) pore size distribution of metal-ion-doped PPN400-CMS550 membranes in comparison to metal-ion-free counterpart.

The pyrolysis temperature largely determines the microstructure characteristics of carbon materials [69]. The pyrolysis of neat PPN400 and metal-ion-doped PPN400 at 750 ℃ led to the decomposition of phthalocyanine, as evidenced by UV-vis analysis (**Figure 4.5**) in the phthalocyanine moieties disappeared. For CuPPN400-CMS750, the existence of two sharp peaks ($2\theta = 43.59^{\circ}$ and 50.70°) indicated that a nanocrystal structure was formed in the amorphous carbon matrix (**Figure 4.4(e)**). The crystalline structure might be Cu nanoparticles with d-spacing values of 2.08 Å (1 1 1) and 1.80 Å (2 0 0) due to the reduction of Cu^{2+} at the elevated pyrolysis temperature [134]. For CoPPN400-CMS750 and ZnPPN400-CMS750, the appearance of small but sharp peaks indicated a certain

extent of crystallization occurred in the respective carbon matrix despite the representative species being unable to be identified. For CoPPN400-CMS750, it could be possible that the carbonization of PPN formed nanostructures similar to multi-wall carbon nanotubes with the aid of Co^{2+} [24]. The doped metal ions could be released from destroying phthalocyanine rings into carbon matrix and participate in complicated thermal reactions at high pyrolysis temperatures. Pore size distribution analysis revealed the micropore distribution of carbonaceous materials derived from neat PPN400 and metal-ion-doped PPN400 networks at 750 °C (**Figure 4.4(f)**). The pore size distribution of ZnPPN400-CMS750 was apparently similar to that of PPN400-CMS750, possessing both abundant micropores and ultramicropores. However, the formation of microporosity of CuPPN400-CMS750 and CoPPN400-CMS750 seemed to be suppressed (**Table 4.2**). This was plausibly due to metal nanoparticles or clusters formed after the decomposition of metal-ion-doped phthalocyanine moieties, resulting in blocking effect in the microporous carbon [135, 136]. Though the detailed mechanism on microstructure formation via each type of metal ions required future studies, it could be concluded that the microstructure of PPN-derived carbon materials could be controlled by the type of metal ion and pyrolysis temperature.

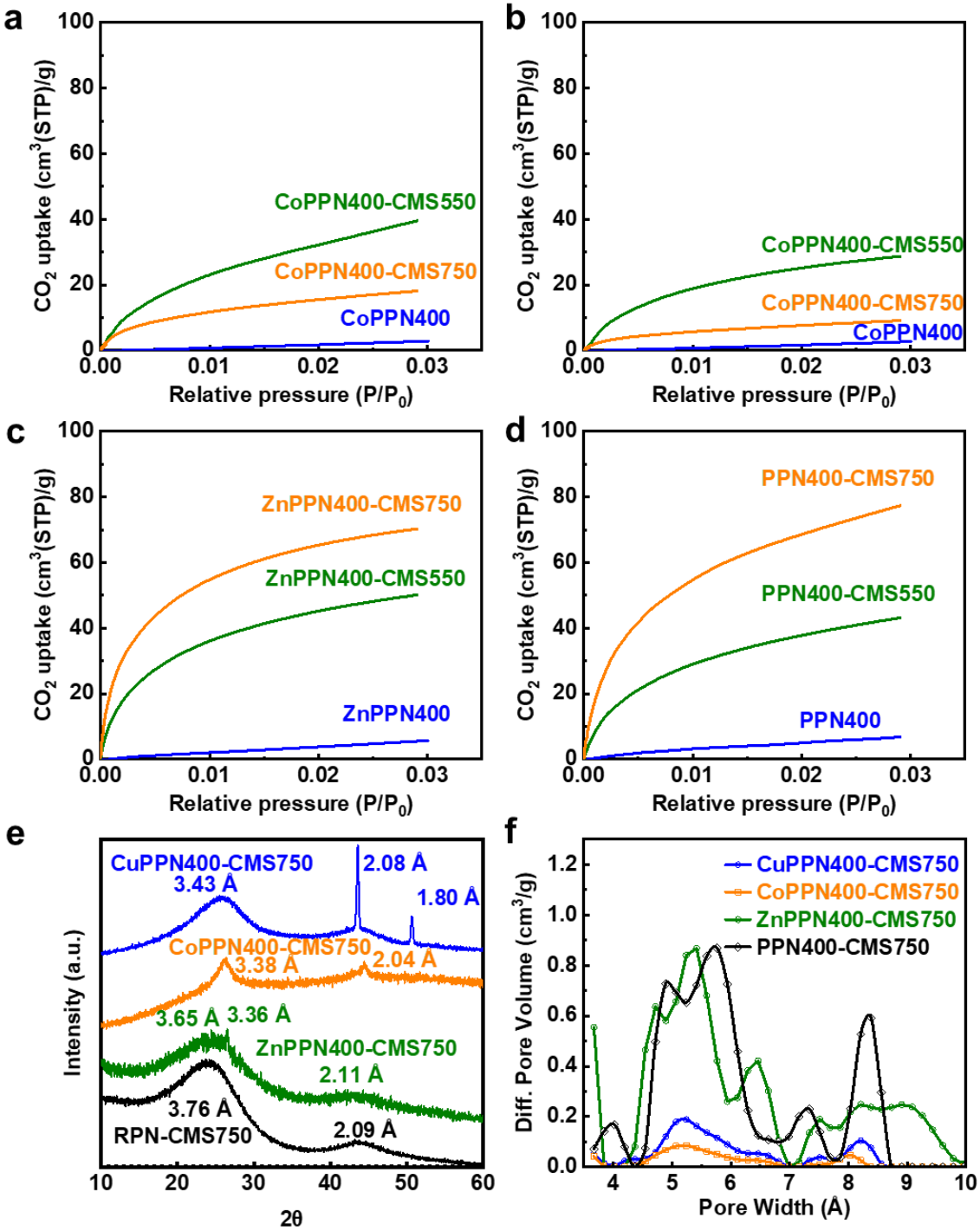

Figure 4.4 CO_2 isothermal uptake plot, pore size distribution, XRD pattern of neat PPN, metal-ion doped PPN, and the derived carbon. (a-d) CO_2 isothermal uptake plot of the PPN network and the derived carbon obtained at 550 and 750 °C. CuPPN, (b) CoPPN, (c) ZnPPN, and (d) neat PPN; (e) XRD pattern, and (f) Pore size distribution of PPN-derived carbon pyrolyzed at 750 °C.

Neat PPN400 and metal-ion-doped PPN400 supported membranes were fabricated on a porous ceramic substrate for gas permeation analysis, which will be discussed in ***Chapter 4.2.3***. It shall be noted that PPN was brittle due to its rigid and crosslinked polymer network. Both neat PPN400 and metal-ion-doped PPN400 could form a defect-free dense polymeric layer on the top of the porous substrate (pore size ~200 nm). The thickness of the polymeric layer could be feasibly controlled by solution concentration, spinning rate, and coating cycle [9, 100]. It was observed that neat PPN400 and metal-ion-doped PPN400 networks could form defect-free layers with a 2.1 to 2.5 μm thickness (**Figure 4.6**). Even tiny pinholes would lead to membrane gas selectivity loss [137]. Based on the microstructure analysis results, the carbonization of neat PPN400 and metal-ion-doped PPN400 supported membranes was therefore designed to occur at a predetermined moderate pyrolysis temperature of 550 ℃ to study the PPN-derived carbon matrices as homogeneous materials. After carbonization, the polymeric layer was converted into amorphous carbon with a 1.4 to 1.7 μm thickness. It was observed that the carbonized PPN400 and metal-ion-doped PPN400 layer on porous substrates maintained a defect-free feature. The result agreed with the supported PPN and carbonized thin-films on a nonporous silica substrate made by Liu [9]. In short, both neat PPN and metal-ion-doped PPN networks could be fabricated into defect-free supported polymeric and CMS membranes.

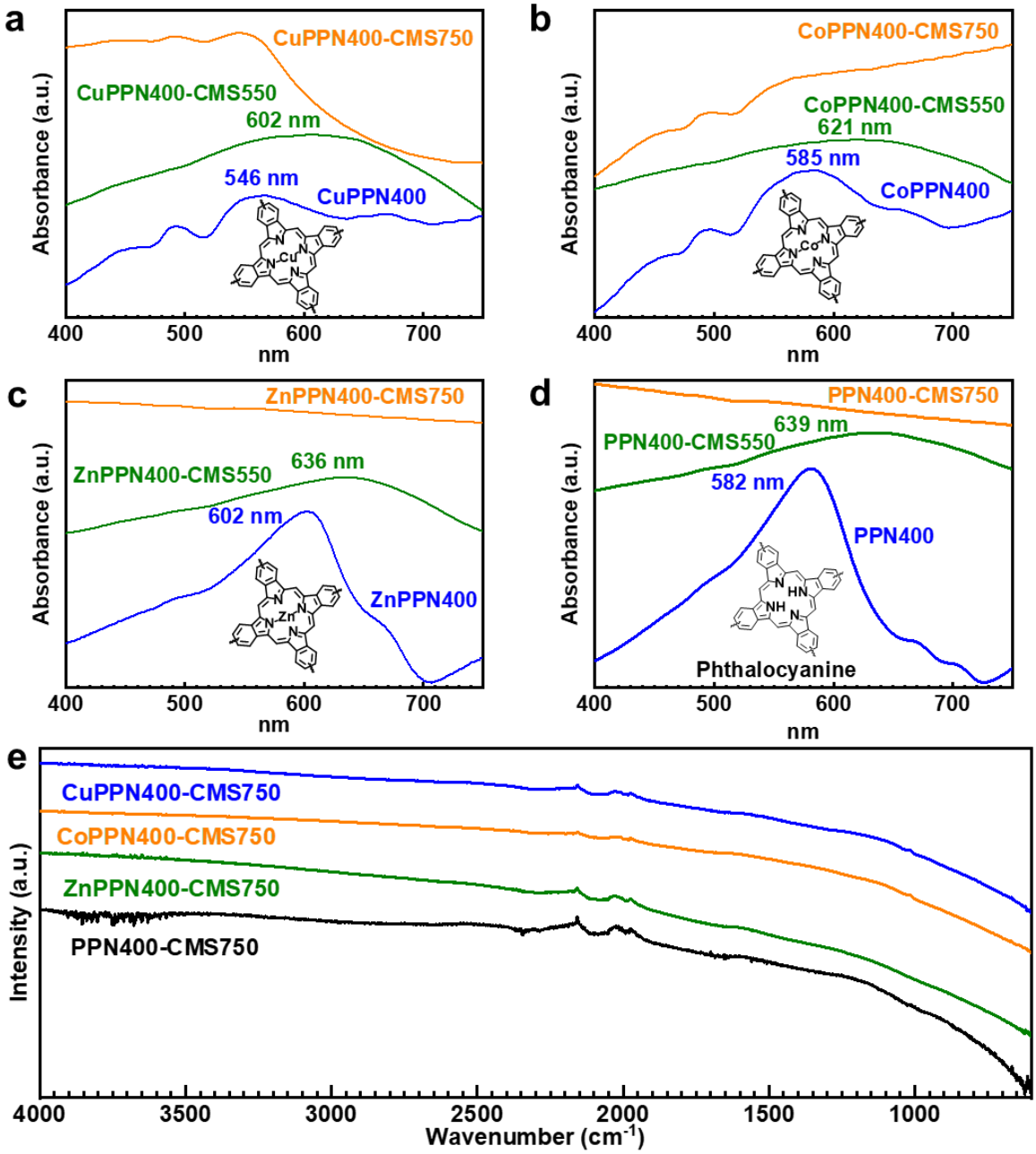

Figure 4.5 Thermal degradation of neat and metal-ion-doped phthalocyanine moieties in PPN network. (a) UV-Vis spectrum of CuPPN, (b) CoPPN, (c) ZnPPN, and (d) neat PPN network. (e) FTIR-ATR spectrum of neat and metal-ion-doped PPN network after pyrolysis at 750 °C.

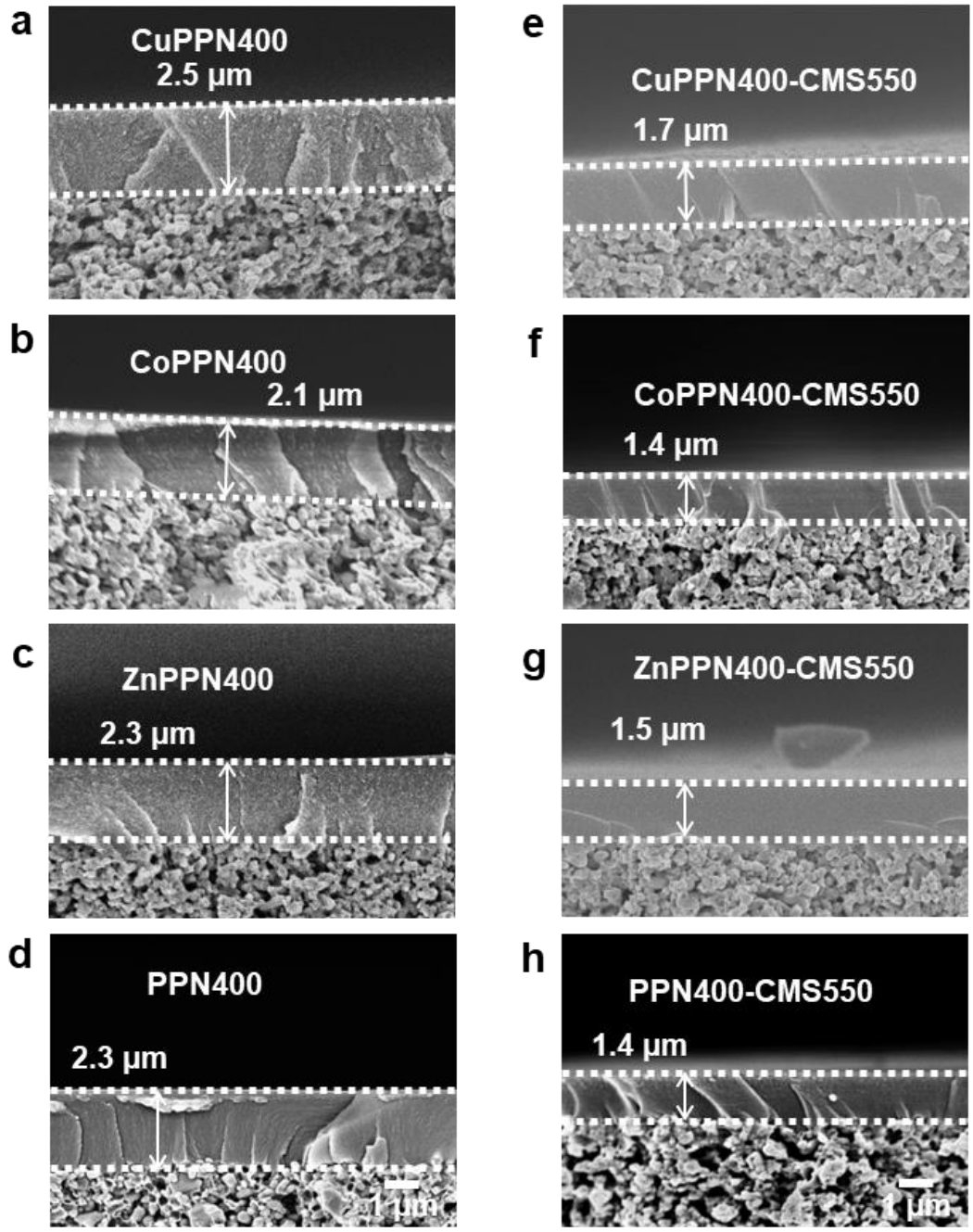

Figure 4.6 Membrane thickness of PPN-based precursor membranes and the derived carbon molecular sieve membranes pyrolyzed at 550 °C. (a) CuPPN400, (b) CoPPN400 (c) ZnPPN400, and (d) PPN400 membranes before pyrolysis. (e) CuPPN400-CMS550, (f) CoPPN400-CMS550, (g) CuPPN400-CMS550, and (h) PPN400-CMS550 membranes after carbonization.

4.2.3 Gas permeation analysis on supported membranes of neat PPN, metal-ion-doped PPN, and the derived carbon membranes

Gas permeation analysis revealed the gas permeation behavior of neat PPN400 and metal-ion-doped PPN400 membranes and the derived microporous carbon membranes (**Table 4.3**). As expected, the gas permeance of gas molecules followed the reverse order of gas molecules in kinetic diameter: CO_2 (3.3 Å) > O_2 (3.46 Å) > N_2 (3.64 Å). This phenomenon was because the glassy polymer with exceptional chain rigidity favors the diffusion of small molecules over larger ones. The gas permeability of metal-ion-doped PPN400 membranes was in the same magnitude as that of neat PPN400 membranes. It was expected that the trend of gas permeability of PPN400 and metal-ion-doped PPN400 membranes might follow the average intermolecular distance of the polymers due to the size-sieving effect in the glassy polymer networks. The O_2 and N_2 permeabilities of the polymeric membranes followed the order of d-spacing values of intermolecular stacking (semicrystalline) regions (**Table 4.1** and **Table 4.3**). It might be possible that the intermolecular stacking of the PPN400 network has the dominant effect on gas permeation behavior. An exception was the CO_2 permeability of the polymeric membranes, which did not follow the trend of d-spacing values in either amorphous or semicrystalline regions. Specifically, the CoPPN400 membrane exhibited the highest CO_2 permeability among the polymeric membranes. This might be attributed to the doping of Co^{2+} favoring the transport of quadrupolar CO_2 molecules [138, 139]. Though further characterization might be required to identify true reason for the phenomenon, the overall low-to-moderate gas permeability of neat and metal-ion-doped PPN400 membranes again indicated the nonporous nature of the PPN400 resins with or without

the doping of metal ions. After the carbonization of the membranes at 550 ℃, however, the gas permeability of both neat and metal ion-doped PPN-CMS550 membranes significantly increased (**Table 4.3**). This effect was mainly attributed to the formation of micropore and ultramicropore structures in the PPN-derived carbon. As expected, the trend of gas permeability of the carbonized membranes was in good agreement with the trend of d-spacing values (**Table 4.1** and **Table 4.3**). The results indicated that the larger average intermolecular space between carbon nanosheets could provide a more efficient gas transport pathway to gas molecules. The relatively low gas permeability of the CoPPN400-CMS550 membrane was an exception, probably because of its lower micropore volumes than the other PPN-derived CMS membranes (**Table 4.2**). Interestingly, the neat PPN400-CMS550 membrane improved by about four orders of magnitude compared to the precursor counterpart. In contrast, incorporating metal ions increased the gas permeability of the carbonized metal-ion-doped PPN membranes by about 1-3 orders of magnitude. Another plausible reason for the significant difference in gas permeability of the PPN-derived microporous carbon membranes was that the metal ion inside the microporous carbon acted as an impermeable "block" that hindered gas transport through the carbonized membranes [136]. Given the complicity of pyrolysis, the true reason for the different enhancement in gas permeation properties of PPN network with and without metal ion doping after carbonization requires further investigation and characterization. Nonetheless, the results indicated that the microstructure characteristics of PPN-derived microporous carbon materials could be effectively adjusted by the design of the precursor network, thus adjusting the gas permeation behavior of the obtained microporous carbon membranes.

Table 4.3 Gas permeability of neat and ion-doped PPN and the derived carbon molecular membranes.

Membrane	Precursor (Barrer)			CMS550 (Barrer)		
	CO_2	O_2	N_2	CO_2	O_2	N_2
CuPPN400	2.4 ± 0.2	0.48 ± 0.03	0.10 ± 0.01	62.1 ± 10.8	24.0 ± 2.99	10.9 ± 2.5
CoPPN400	4.7 ± 0.1	0.76 ± 0.02	0.12 ± 0.03	38.9 ± 3.7	6.4 ± 0.6	2.0 ± 0.2
ZnPPN400	3.8 ± 0.1	1.3 ± 0.2	0.46 ± 0.05	396 ± 77	197 ± 42	126 ± 30
PPN400	4.4 ± 0.3	1.1 ± 0.2	0.20 ± 0.02	7623 ± 166	2625 ± 52	1082 ± 46

It was hypothesized that the adjustment on the microstructure arrangement of the PPN network is close to the kinetic diameter of gas molecules to improve the gas selectivity of the polymeric membrane. In comparison to the neat PPN400 membrane with intermolecular stacking at a d-spacing value of 3.54 Å, the CuPPN400 membrane with a much narrower stacking of 3.28 Å showed slightly increased CO_2/N_2 selectivity of about 9% (**Table 4.1** and **Table 4.4**). This could be attributed to the more ordered and narrowed intermolecular stacking, leading to the improved size-sieving ability of smaller gases (CO_2) to larger ones (N_2). Similarly, the PPN400 membrane possessed both higher CO_2/N_2 and O_2/N_2 selectivity than the ZnPPN400 membrane with a broader stacking of 3.78 Å. Interestingly, the CoPPN400 membrane with promoted intermolecular stacking of 3.35 Å exhibited improved CO_2/N_2 and O_2/N_2 selectivity by about 77% and 13%, respectively, in comparison to the PPN400 membrane. A possible reason was that the narrowly stacked molecular arrangements favored the transport of small gas molecules rather than the larger ones. Another plausible explanation might be that incorporating Co^{2+} in phthalocyanine moieties might facilitate the transport of CO_2 and O_2 over N_2,

thereby enhancing CO_2/N_2 and O_2/N_2 selectivity [138, 139]. This phenomenon is because the Co^{2+} complexes could provide additional sorption sites and diffusion pathways to the membrane by reversible reactions with polar gas species (CO_2 or O_2) instead of nonpolar ones (N_2) [139, 140]. Though the gas transport mechanism of the CoPPN400 network might require further studies, it was confirmed that the adjustment of the average intermolecular distance of the semicrystalline region played an essential role in the gas permeation behavior of membranes based on the PPN network.

Table 4.4 Ideal gas selectivity of neat and ion-doped PPN and the derived carbon molecular sieve membranes.

Membrane	Precursor		CMS550	
	CO_2/N_2	O_2/N_2	CO_2/N_2	O_2/N_2
CuPPN400	24.0 ± 2.7	4.8 ± 0.6	5.7 ± 1.6	2.2 ± 0.6
CoPPN400	39.2 ± 9.4	6.3 ± 1.5	19.5 ± 3.0	3.2 ± 0.5
ZnPPN400	8.3 ± 0.8	2.8 ± 0.5	3.1 ± 0.9	1.6 ± 0.5
PPN400*	22.1 ± 2.6	5.6 ± 1.1	7.0 ± 0.3	2.4 ± 0.1

After carbonization at 550 ℃, the gas selectivity of all carbon membranes was lower than the polymeric precursor counterparts (**Table 4.4**). This result could be attributed to the competition between the molecular sieving effect and Knudsen diffusion transport [141]. The trend of gas selectivity of carbonized PPN400 and metal-ion-doped PPN400 membranes agreed with that of the precursor counterparts. However, it was observed that the trend of gas selectivity of carbonized membranes did not entirely follow that of d-spacing values. In fact, the XRD analysis was powerful for depicting intermolecular

distance instead of resolving micropore and ultramicropore distribution of microporous carbon materials [98]. For carbon molecular sieve membranes, the size and distribution of ultramicropores largely dominated their size-sieving ability for small gas molecules [69, 141, 142]. However, typical gas (CO_2) sorption analysis at 0 ℃ could not fully resolve the pore size distribution below 4 Å in the ultramicropore region [98]. Gas permeation analysis using small gas molecules as "probes" could reveal the accessible ultramicropores of the microporous carbon membranes [133]. Specifically, though the PPN400-CMS550 membrane showed broader ultramicropore distribution in the range of 4 to 7 Å, the carbon membrane without the doping of metal ions possessed both superior gas selectivity as well as permeability than the CuPPN400-CMS550 membrane. It was inferred that the ultramicropores below 4 Å constructed by intermolecular stacking involved metal-ion-doped phthalocyanine might be hindered by the doped metal ions, and therefore become relatively difficult for gas transport even for small CO_2 molecules. Indeed, the PPN400-CMS550 membrane showed both higher gas permeability and selectivity of CO_2/N_2 and O_2/N_2 than ZnPPN400-CMS550 membrane. This could be mainly attributed to the more accessible and narrowly distributed ultramicropores of the PPN400-CMS550 membrane. The metal-ion block effect could be the main reason for the superior ideal gas separation performance of neat PPN400-CMS550 membranes compared to that of CuPPN400-CMS550 and ZnPPN400-CMS550 membranes. Interestingly, the CoPPN400-CMS550 membrane exhibited higher CO_2 and O_2 selectivity but lower gas permeability than PPN400-CMS550 and the other metal-ion-doped carbon membranes. Apart from the block effect leading to the low gas permeability, the presence of Co^{2+} in CoPPN400-CMS550 membrane might be beneficial to facilitate the transport of CO_2 and O_2 rather than N_2, resulting in the high CO_2/N_2 and

O_2/N_2 selectivity [138, 139]. Nonetheless, it could be concluded that the neat PPN400-CMS550 membrane possessed more accessible ultramicropores to small gas molecules than metal-ion-doped carbon molecular sieve membranes.

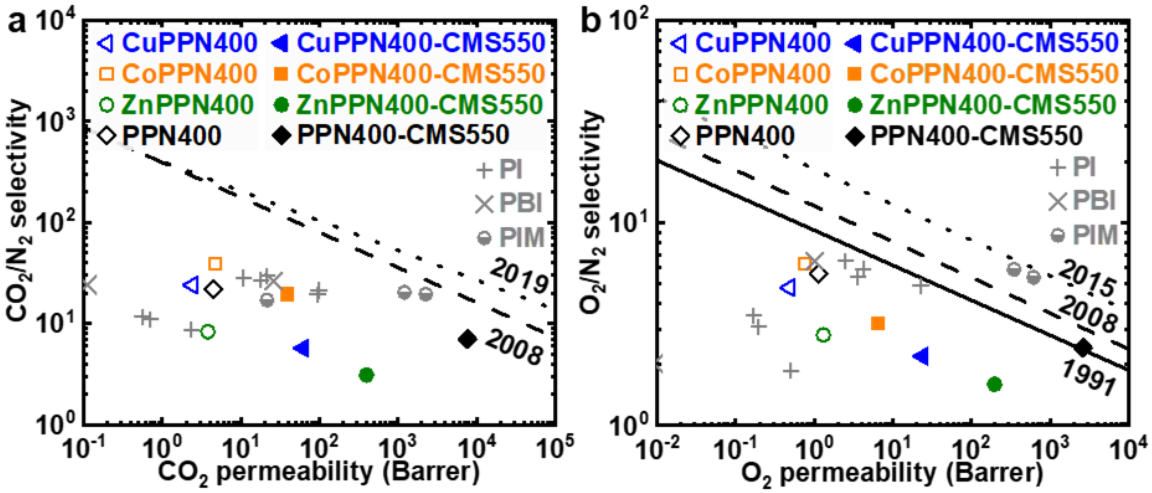

Figure 4.7 Ideal gas separation performance of PPN, metal-ion-doped PPN, and the derived carbon molecular sieve membranes in comparison to Robeson upper bound relationships [49, 143-148]. (a) CO_2/N_2 selectivity versus CO_2 permeability; (b) O_2/N_2 selectivity versus O_2 permeability. (PPN: resorcinol-based phthalonitrile resin; PI: polyimide; PBI: polybenzimidazole; PIM: polymer of microporosity)

The Robeson upper bound relationship plots visualized the ideal CO_2/N_2 and O_2/N_2 separation performance of PPN400, metal-ion-doped PPN, and the derived carbon molecular sieve membranes in comparison to that of the state-of-the-art polymeric membranes (**Figure 4.7**) [60, 63, 69, 149, 150]. Specifically, the empirical straight lines established by Robeson in 1991 and 2008 indicated the trade-off relationship between gas permeability and ideal selectivity of conventional nonporous polymeric membrane materials, including heterocyclic polyimide (PI) and polyimidazole (PBI) [60, 63]. More recently, the 2015 and 2019 upper bound lines were defined by polymers of

microporosity (PIM) membranes with superior gas separation performance than nonporous polymeric membranes [149, 150]. The ideal gas separation performance of both neat PPN and metal-ion-doped PPN membranes is located among well-developed PI and PBI membranes, indicating the nonporous nature of the PPN400 network. Interestingly, the doping of Co^{2+} slightly improved both CO_2 permeability and the ideal CO_2/N_2 selectivity of the CoPPN400 membrane, making the ideal gas separation performance of the membrane located near the trade-off lines. Notably, the carbonization of the neat PPN400 network considerably improved the CO_2 and O_2 permeability of the membrane despite a moderate reduction in gas selectivity. This result was mainly attributed to the formation of a bimodal-distributed microporous structure that brought the ideal gas separation performance of PPN400-CMS550 membranes to the state-of-the-art Robeson upper bound lines. In contrast, the incorporation of metal ions in microporous carbon derived from PPN400 resulted in suppression in gas permeability of the membranes due to the metal ion block effect, which could be potentially beneficial to designing low-temperature pyrolyzed carbon-based barrier for small molecules [151]. In short, this study revealed the effect of metal-ion doping on the microstructure characteristics and gas permeation behavior of the PPN network and the derived microporous carbon materials in the context of the membrane, which will be further discussed in ***Chapter 5***.

4.3 Conclusion

This work demonstrated a novel adjustment method on the microstructure arrangement of resorcinol-based phthalonitrile resins and the derived carbon materials via metal-ion

doping. The thermal analysis revealed that the metal-ion-doped PPN network had excellent thermal stability similar to the neat counterparts below 600 ℃. The microstructure analysis confirmed that the doping of metal ions could adjust the average intermolecular distance of the PPN network. The exaggerated thermal decomposition of metal-ion-doped phthalocyanine moieties was observed, resulting in the formation of inhomogeneous crystalline structures in an amorphous carbon matrix pyrolyzed at 750 ℃. However, the carbonization at 550 ℃ of the non-microporous PPN network produced homogeneous microporous carbon materials of which pore size distribution could be adjusted by doping metal ions. For the first time, gas permeation analysis revealed the influence of graphite-like stacking (semicrystalline) region of neat PPN and metal-ion-doped PPN network on the gas permeation behavior of the membranes. The doping of metal ions in phthalocyanine moieties could effectively adjust the average intermolecular stacking distance, thereby adjusting the gas permeation behavior of the PPN membranes. Besides, it was observed that the gas permeability and selectivity of PPN-derived microporous carbon membrane at 550 ℃ approached Robeson's upper bounds, indicating the potential of PPN-derived carbon materials on gas separation. Furthermore, it was concluded that the doping of metal ions could significantly modify the ultramicropores smaller than 4 Å to suppress gas permeation through the PPN-derived microporous carbon membranes. This work demonstrated the adjustability of microstructure characteristics of PPN and its derived carbon materials, paving the way for further development of PPN-derived advanced materials for gas separation.

Chapter 5

Microstructure evolution and gas permeation behavior of PPN-CMS membrane

Carbon molecular sieve (CMS) membranes hold great promise for energy-efficient gas separation, contributing to mitigating greenhouse gas emissions. Exploring new types of microstructurally tunable polymeric precursors is critical for understanding the evolution of carbon microstructure arrangement and adjusting the gas permeation behavior of CMS membranes. As a precursor for CMS membranes, polyphthalonitrile (PPN) resin with both tunable intermolecular distance and π-π stacking arrangement is reported for the first time. It was demonstrated that the aforementioned two key features of the thermally crosslinked PPN network are beneficial to forming PPN-CMS membranes with enlarged intermolecular distance and small-sized, narrow-distributed ultramicropores (<7 Å), thereby improving gas permeability and ideal selectivity. This study provides new insights into the microstructure evolution of PPN-derived microporous carbon materials. Owing to its excellent thermal stability, tunable microstructure arrangement, and flexibility of chemical synthesis, PPN represents a promising class of polymeric precursor materials for fabricating CMS membranes.

5.1 Introduction

One of the global challenges in mitigating climate change is the excessive energy consumption from chemical separation processes, including gas separation [145, 152, 153]. Conventional distillation or adsorption/absorption gas separation requires additional energy on phase transition or adsorbent/adsorbent regeneration [153-155]. In contrast, membrane separation technology has emerged as a competitive energy-efficient solution in pre- and post-combustion scenarios (i.e., oxygen enrichment (O_2/N_2) and carbon capture (CO_2/N_2), respectively) to reduce greenhouse gas emissions [37, 46, 145, 155, 156]. Polymeric materials are commonly used in fabricating gas separation membranes due to their low cost, good processability, and excellent scalability [59]. However, there is usually a trade-off between gas permeability and selectivity of polymeric membranes [60, 63, 149, 150, 157]. Carbon molecular sieve (CMS) membranes are promising for gas separations due to their outstanding gas separation performance surpassing the trade-off relationship of polymeric membranes [68, 69, 158]. Besides, CMS membranes have gained wide research interest due to their excellent thermal and chemical stability, and tailorable carbon microstructures [68, 69].

CMS membranes are commonly derived from thermally stable polymeric precursors, such as polyimide (PI) [49, 67, 70, 100, 143-146, 159], polyacrylonitrile (PAN) [160, 161], polybenzimidazole (PBI) [142, 146, 147], poly(furfuryl alcohol) (PFA) [162-164], phenolic resin (PR) [110, 111, 165-167], and polymer of intrinsic microporosity (PIM) [143, 148]. Among these precursors, polyimide is widely used to obtain CMS membranes due to its various molecular structures, good membrane formability, and excellent

thermal stability [59, 145]. The flexibility of the chemical synthesis of polyimides enables versatile microstructure design of precursors to intensively study the microstructure evolution of amorphous carbon that determines the gas separation performance of CMS membranes [59, 67-69]. Hu *et al.* [49] demonstrated that the CMS membranes derived from the polyimide with rigid and bulky bisaminophenylfluorene moieties exhibited a greater amount of effective ultramicropores with narrowed distribution for gas permeation, resulting in enhanced CO_2 permeability (about 238%) with maintained CO_2/N_2 ideal selectivity, in comparison to the CMS membranes derived from the Matrimid polyimide. Liang *et al.* [144] demonstrated that the CMS membranes derived from the polyimide with planar benzimidazole moieties promoted more π-π stacking, thereby improving the CO_2/N_2 and O_2/N_2 ideal selectivities to 53 and 12.5, respectively; however, the gas permeability was compromised compared with those derived from conventional polyimides at the pyrolysis temperature of 800 ℃. Thermal crosslinking of polymer chain arrangement has also been explored to enhance the gas separation performance of CMS membranes [69, 168]. Recently, Liu *et al.* [145] investigated CMS membranes derived from a molecularly engineered 6FDA-based polyimide with a kinked structure and a crosslinkable carboxyl group. The crosslinking of the carboxyl group at 400 ℃ resulted in an increase in the average intermolecular distance of the CMS membrane obtained at 550 ℃, leading to a 56% improvement in pure CO_2 permeability despite a moderate compromise in the CO_2/CH_4 ideal selectivity about 30%. More recently, a few studies have been reported, which were focused on modifying the microstructure and gas separation performance of CMS membranes via thermal rearrangement induced π-π stacking of PIM precursors [143, 148]. Zhao *et al.* [143] proposed that the polyimide with Tröger bases ladder-like moieties, which

underwent thermal rearrangement into pyridine structure above 450 ℃, could promote the π-π stacking of the polymer chain that further transformed into the π-π stacking of carbon sheets at 600°C, thereby improving gas permeability and selectivity of the derived CMS membranes. In short, the microstructure characteristics and gas separation performance of CMS membranes can be adjusted through the microstructure design of the polymeric precursor [69, 169]. The development of microstructure design of thermally stable polymeric precursors for CMS membranes might be advanced by adopting organic materials requiring facile synthesis and fabrication procedures [38, 40]. Therefore, it is essential to explore thermally stable precursor materials with flexible tunability in microstructure to develop CMS membranes.

Polyphthalonitrile (PPN), also known as phthalonitrile prepolymer, is recognized as a unique class of thermosetting polymeric materials due to its facile chemical synthesis, versatile molecular design, and excellent thermal properties [2, 6, 8, 12, 22, 121]. Its high thermal stability is due to the formation of the crosslinked network composed of heterocyclic moieties (i.e., isoindolenine, triazine, and phthalocyanine) via amine-catalyzed addition-polymerization of phthalonitrile above 220 ℃ (**Figure 5.1(a)**) [6, 8, 9, 15, 170]. Specifically, its high char yield positions the polymeric precursor as an ideal candidate for developing high-performance carbon materials [2, 6, 8, 12, 22]. Moreover, the char yield of PPN can be further enhanced through copolymerization with various types of PPN monomers [11, 171] or polymers [3, 36, 172, 173]. The polymer chain rigidity of PPN, represented by the glass transition temperature, generally increased with higher curing temperatures [8, 9]. Notably, extensively cured PPN resin has been reported to exhibit a glass transition temperature exceeding 450 ℃, indicating its exceptionally

high polymer chain rigidity [9]. It was demonstrated in ***Chapter 6*** that the incorporation of resorcinol-based phthalonitrile prepolymer with polyimide could influence the polymer chain rigidity and microstructure characteristics of the PPN/PI blend membranes. The curing treatment on the blend membranes formed a semi-interpenetrating network via PPN crosslinking, increasing the intermolecular distance as well as the gas permeability of the membranes. Recently, Tian *et al.* [174] reported that poly(aryl ether ketone) crosslinked by phthalonitrile moieties exhibited an ordered segment arrangement of about 3.4 Å. This phenomenon could be attributed to the formation of π-π stacking of the crosslinked phthalonitrile network, which was found by Snow *et al.* [15]. The unique thermal properties and tunable microstructure arrangement position the PPN precursor as an excellent carbon source for designing high-performance carbon materials requiring precise pore size control. To the best of our knowledge, no published studies specifically investigate the relationship between the microstructure characteristics and the gas permeation behavior of PPN and PPN-derived carbon materials.

The carbon structure derived from the PPN has been intensively studied [2-5, 9, 20, 25]. During pyrolysis, the amorphous PPN network converts into an amorphous straticulate carbonaceous structure [4, 5, 20, 25]. Weng *et al.* [4] described the preparation of PPN-based amorphous carbon pyrolyzed from 550℃ to 800 ℃ as a supercapacitor and gas absorbent. It was reported that the potassium hydroxide-activated hierarchical porous carbon pyrolyzed at 650 ℃ exhibited abundant micropores compared with its urea-activated counterpart. Zhang *et al.* [5] reported the design of PPN-derived carbon foam for electromagnetic interference (EMI) shielding. The PPN-derived carbon foam pyrolyzed at 600 ℃ generated an amorphous straticulate carbonaceous structure,

improving EMI shielding effectiveness compared with the cured PPN network. Many studies have been reported on developing the thermally stable PPN network into high-performance porous carbon materials, including hierarchical porous carbon and carbon foam [2, 4, 5]; however, PPN-based materials have never been investigated as a precursor for CMS membranes in the published literature. Gaining insights into the evolution of microstructure arrangement involved in the process from PPN precursors into derived microporous carbon materials is crucial to developing PPN-based CMS membranes.

This study investigates thermally crosslinkable PPN with tunable intermolecular distance and π-π stacking arrangement as a novel precursor for CMS membranes and their potential in gas separation. The primary focus of this research is to understand the microstructure-property relationship of both the PPN and the resulting PPN-CMS membranes, while other effects (e.g., mixed-gas or aging) are beyond the scope of this study. This work demonstrates that the tunability of PPN precursor in both intermolecular distance and π-π stacking is crucial to adjusting microstructure characteristics and gas permeation behavior of the produced PPN-CMS membranes. PPN could be a new class of CMS membrane materials due to its superb thermal properties and tunable microstructure.

5.2 Results and discussions

5.2.1 Thermal, chemical, and microstructure characteristics of PPN precursor

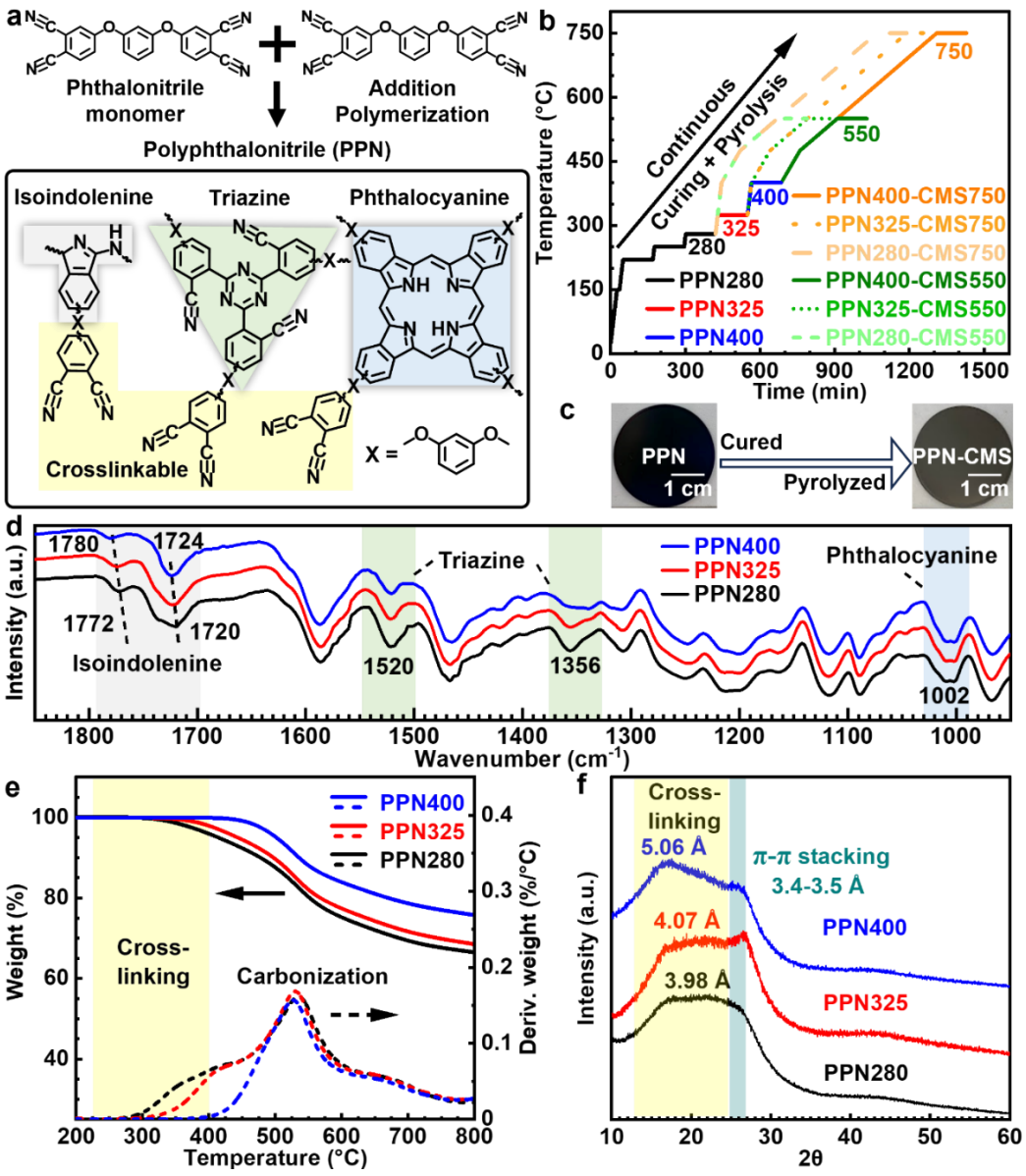

Figure 5.1 PPN precursor and the derived PPN-CMS membranes. (a) Schematic drawing of thermally crosslinkable PPN monomer and prepolymer structure. (b) Thermal curing and pyrolysis protocol for membrane fabrication. (c) Optical images of supported PPN and PPN-CMS membranes. (d) FTIR-ATR spectrum, (e) TGA and DTG patterns, and (f) XRD spectrum of PPN precursors with respect to curing temperature.

The supported PPN membrane was progressively cured into a crosslinked PPN network (**Figure 5.1(a)**), and then it was directly carbonized to obtain the PPN-CMS membrane (**Figure 5.1(b)**). It was worth noting that the thermosetting PPN prepolymer required progressive curing treatment to establish sufficiently high thermal stability [2, 3, 5, 6, 8, 9, 121, 175], thereby enabling the fabrication of defect-free PPN-CMS membrane in this work (**Figure 5.1(c)**). The curing treatment of PPN enabled the crosslinking of phthalonitrile moieties into heterocyclic structures, such as isoindolenine (1772 cm^{-1} and 1720 cm^{-1}), triazine (1520 cm^{-1} and 1356 cm^{-1}), and phthalocyanine (1002 cm^{-1}) (**Figure 5.1(a)** and **Figure 5.1(d)**) [6, 8]. The crosslinked structures might increase the stiffness of the PPN network [6]. Meanwhile, the formation of bulky moieties (i.e., triazine and phthalocyanine) might increase steric hindrance. Consequently, the polymer chain rigidity of the PPN network could be improved by curing treatment. Indeed, the glass transition temperature of PPN increased with higher curing temperatures (**Table 5.1** and **Figure S1**). Compared with the PPN280 precursor, the glass transition temperature of PPN400 increased from 277 ℃ to over 500 ℃, indicating significantly improved polymer chain rigidity. Simultaneously, the thermal stability of the PPN precursors was also improved through the curing process (**Figure 5.1(e)**). The maximum thermal decomposition for all the PPN precursors occurred at around 530 ℃, followed by a secondary decomposition up to 775 ℃. This decomposition sequence was attributed to the pyrolysis of aromatic ester, isoindolenine, and pendant nitrile groups, followed by other thermally stable groups such as triazine and phthalocyanine rings [25, 176]. FTIR-ATR and UV-Vis spectrum confirmed that thermally stable moieties (i.e., phthalocyanine) remained in the PPN-derived carbon at 550 ℃, while the characteristic peaks of residues disappeared after pyrolysis at 750 ℃ (**Figure 5.2**). In comparison to the PPN280

precursor, PPN400 possessed T_{d90} (i.e., decomposition temperature at 90% weight remaining) of 536 ℃ (increased from 478 ℃), and carbon yield (at 800 ℃) of 76% improved (from 66%) (**Table 5.1**). The enhancement of thermal stability of the cured PPN network was well aligned with previous studies on the crosslinking of thermosetting PPN resins due to the crosslinking of the phthalonitrile moieties [2, 6, 8, 9]. It was concluded that the crosslinking of phthalonitrile moieties improved the thermal stability of the PPN network against elevated curing temperature. The high thermal decomposition temperature and glass transition temperature of cured PPN precursors evidenced the potential of this type of polymeric material for fabricating CMS membranes [69].

Table 5.1 Thermal stability, char yield, and polymer chain rigidity of PPN, as well as d-spacing values of PPN and the derived PPN-CMS membranes with respect to curing temperature.

Precursor with curing	T_{d90} (℃)	Char yield @ 800 ℃	T_g (℃)	d-spacing (Å)	d-spacing (Å)	
					CMS550	CMS750
PPN280	478	66%	277	3.98	3.85	3.58
PPN325	497	69%	326	4.07, 3.39	4.01	3.76
PPN400	536	76%	>500*	5.06, 3.54	4.12	3.76

Note: *Equipment temperature limit for DMA instrument.

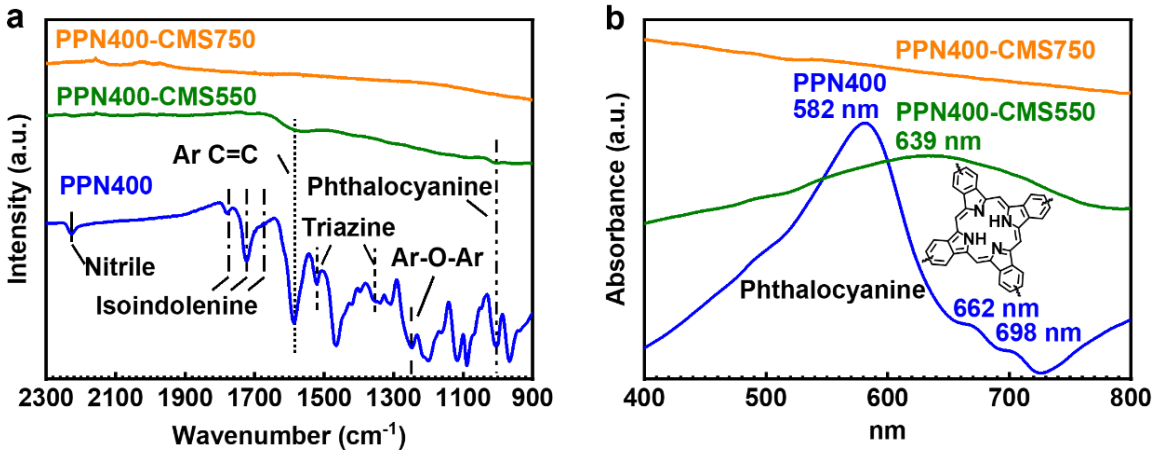

Figure 5.2 Chemical characteristics of PPN-CMS membranes. (a) FTIR-ATR and (b) UV-Vis spectra of supported PPN-CMS membranes with respect to pyrolysis temperature.

The curing treatment of the PPN precursor plays a crucial role in the microstructure arrangement of the PPN network. It was expected that the microstructure arrangement of PPN could be adjusted above its glass transition temperature, allowing movement of the polymer chain. XRD analysis revealed the microstructure evolution of the PPN network against curing treatment. The d-spacing value indicates the average intermolecular distance of the polymeric materials. The PPN280 precursor exhibited a broad peak, suggesting the amorphous nature of the crosslinked PPN network (**Figure 5.1(f)**). Increasing curing temperature gradually enlarged the d-spacing values of PPN400 to 5.06 Å from 3.98 Å, compared with that of PPN280. This effect indicated that the crosslinking of PPN produced more rigid and bulky moieties, such as triazine and phthalocyanine, which resulted in the enlarged average intermolecular distance of the network. Notably, both PPN325 and PPN400 exhibited an obvious peak around $2\theta = 25° - 26°$ (d-spacing = 3.4 Å - 3.5 Å). The result could be mainly attributed to the π-π stacking (3.4 Å - 3.5 Å) of phthalocyanine moieties [15], leading to a more ordered segment arrangement in the

crosslinked PPN network. Interestingly, comparing the FTIR spectrum of PPN cured from 280 ℃ to 400 ℃ (**Figure 5.1(d)**) revealed that the peak positions of isoindolenine shifted from 1720 cm^{-1} to 1724 cm^{-1} and from 1772 cm^{-1} to 1780 cm^{-1}. Meanwhile, the peak intensity of triazine moieties showed a gradual decrease at 1520 cm^{-1} and 1356 cm^{-1} and an increase at 1339 cm^{-1}. It could be possible that isoindolenine and triazine are also involved in the π-π stacking of the PPN network [174, 177]. Given the complicated nature of the crosslinked network, future work would be required to identify the intermolecular interactions between the phthalonitrile-derived heterocyclic moieties. Nonetheless, it was concluded that the thermal curing treatment could simultaneously promote the formation of a larger intermolecular distance and a more ordered π-π stacking arrangement in the PPN network. The microstructure arrangement of PPN might affect the subsequent PPN-derived carbon matrix, providing enhanced molecular sieving ability for gas molecules with similar sizes.

5.2.2 Microstructure analysis on PPN-CMS membranes

5.2.2.1 Effect of pyrolysis temperature on microstructure characteristics of PPN and PPN-CMS membranes

The PPN precursor was coated on a porous ceramic substrate, followed by pyrolysis to obtain a supported PPN-CMS membrane. It was observed from FESEM (**Figure 5.3(a)**) that a porous ceramic substrate supported a thin, uniform, and nonporous layer, which was the carbon layer derived from the PPN precursor. The increased pyrolysis temperature significantly reduced the thickness of the selective layer from 2.3 μm (PPN400) to 1.0 μm (PPN400-CMS750). The thinner selective layer can give lower gas

transport resistance. However, the microstructure characteristics of the carbon layer might dominate the gas transport behavior of the supported PPN-CMS membrane. The PPN-CMS membranes exhibited carbon slit features within the pyrolysis temperature range (550-750 ℃), as evidenced by the TEM images **(Figure 5.3(a))**, which aligned with the previous literature [20]. It is generally believed that the CMS membrane is composed of carbon nanosheets with sub-nano slits, forming micropores (7-20 Å) and ultramicropores (<7 Å) [68, 98, 105]. The microporous carbon structure of PPN-CMS membranes might provide an efficient diffusion pathway and size-sieving ability for gas molecules. The XRD pattern confirmed the amorphous nature of the PPN-derived carbon membranes pyrolyzed at 550 ℃ and 750 ℃ (**Figure 5.3(b)**). The PPN400-CMS750 membrane had a slightly smaller d-spacing value than that of the PPN400-CMS550 membrane, indicating the narrower packing of the carbon matrix (**Table 5.1**). This result was mainly attributed to the further decomposition of thermally stable heterocyclic residues leading to a more narrow-stacked carbon structure at the higher pyrolysis temperature of 750 ℃ [5, 25, 176].

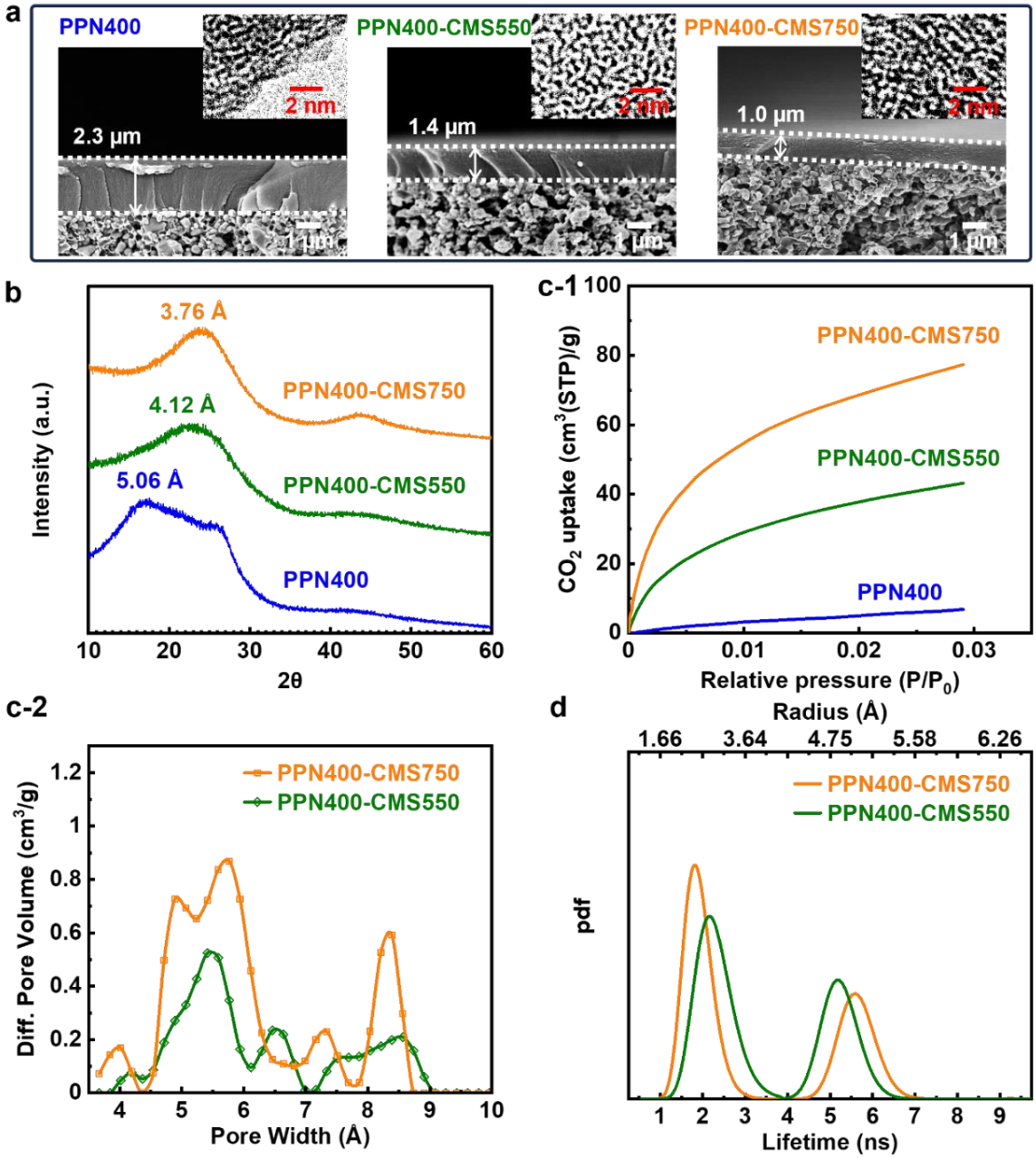

Figure 5.3 Effect of pyrolysis temperature on microstructure characteristics of PPN and the derived CMS membranes. (a) FESEM and (insert) TEM morphology and (b) XRD pattern of supported PPN400, PPN400-CMS550, and PPN400-CMS750 membranes. (c-1) CO_2 adsorption isotherm plots of PPN400, PPN400-CMS550, and PPN400-CMS750 membranes at 273 K. (c-2) DFT (from CO_2 adsorption analysis) and (d) PALS pore size distribution of PPN400-CMS550 and PPN400-CMS750 membranes.

N_2 and CO_2 adsorption analyses were utilized to study the micropore distribution of PPN-CMS membranes (**Figure 5.3(c-1)** and **Figure 5.4**). However, the micropore distribution of the PPN-CMS membranes could not be obtained from the cryogenic N_2 adsorption analysis at 77 K. The result agreed with the recently published work by Weng *et al.* [4] that the PPN-derived amorphous carbon showed limited (or no) micropores. The possible reason might be the existence of small ultramicropores that hinder the access of cryogenic N_2 into the microporous PPN-CMS carbon [4, 98, 178]. Nonetheless, CO_2 adsorption analysis at 273 K was able to reveal the micropore distribution of the PPN-CMS membranes. The result confirmed that PPN-CMS membranes had a bimodal pore size distribution (**Figure 5.3(c-2)** and **Figure 5.5**). The PPN400-CMS750 membrane exhibited a narrower pore size distribution than the PPN400-CMS550 membrane in both the micropore and ultramicropore regions. Notably, the PPN400-CMS750 membrane seemed to have more ultramicropores than the PPN400-CMS550 membrane. These results implied a better molecular sieving ability of the PPN400-CMS750 membrane than that of the PPN400-CMS550 membrane for small gas molecules. It shall be noted that the CO_2 adsorption analysis has limitations on depicting pore size smaller than 4 Å [133]. PALS analysis can characterize pore width (in radius) at a minimum of 2.0 Å (1.0 Å in radius), which enables the analysis of the effect of micropore and ultramicropore distribution on small molecules [49, 69, 113, 114, 133]. The PALS pore size distribution (**Figure 5.3(d)**) fitted from the PAL spectrum (**Figure S2**) further confirmed that the PPN400-CMS750 membrane had a smaller ultramicropore size and a narrower but sharper distribution than the PPN400-CMS550 membrane. The comparison of PPN400-CMS550 and PPN400-CMS750 membranes revealed that the τ_3 (related to pore size) in ultramicropore region reduced by 0.36 ns, indicating ultramicropores radius narrowed by

0.32 Å (**Table 5.2**). Meanwhile, the increase of I_3 (related to pore amount) in ultramicropore region again confirmed the formation of a larger amount of ultramicropore at the higher pyrolysis temperature (750 ℃). These phenomena were attributed to the further decomposition of thermally stable residues, leading to a smaller ultramicropore size with narrower but sharper distribution in the PPN400-CMS750 membrane. In summary, a higher pyrolysis temperature resulted in the supported PPN-CMS membrane with a thinner carbon selective layer thickness, a greater amount of ultramicropores, and a narrower but sharper pore size distribution.

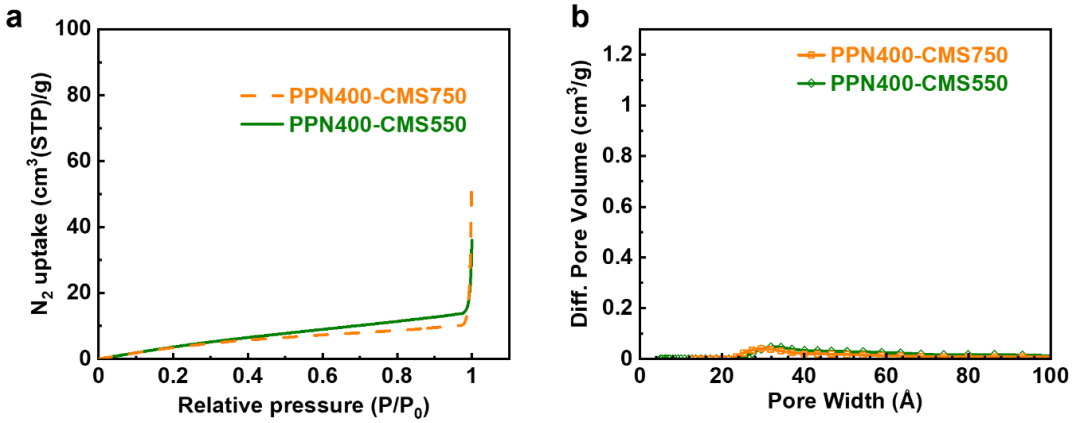

Figure 5.4 Cryogenic N_2 adsorption analysis of PPN-CMS at 77 K. (a) N_2 uptake. (b) DFT pore size distribution assuming carbon-slit structure of PPN-CMS.

Table 5.2 PALS analysis on microstructure characteristics of PPN-CMS with respect to pyrolysis temperature.

Membranes	ultramicropore			micropore		
	τ_3 (ns)	I_3 (%)	Radius (Å)	τ_3 (ns)	I_3 (%)	Radius (Å)
PPN400-CMS550	2.2	7.5	3.03	4.7	6.2	4.61
PPN400-CMS750	1.84	9.4	2.71	4.54	4.8	4.53

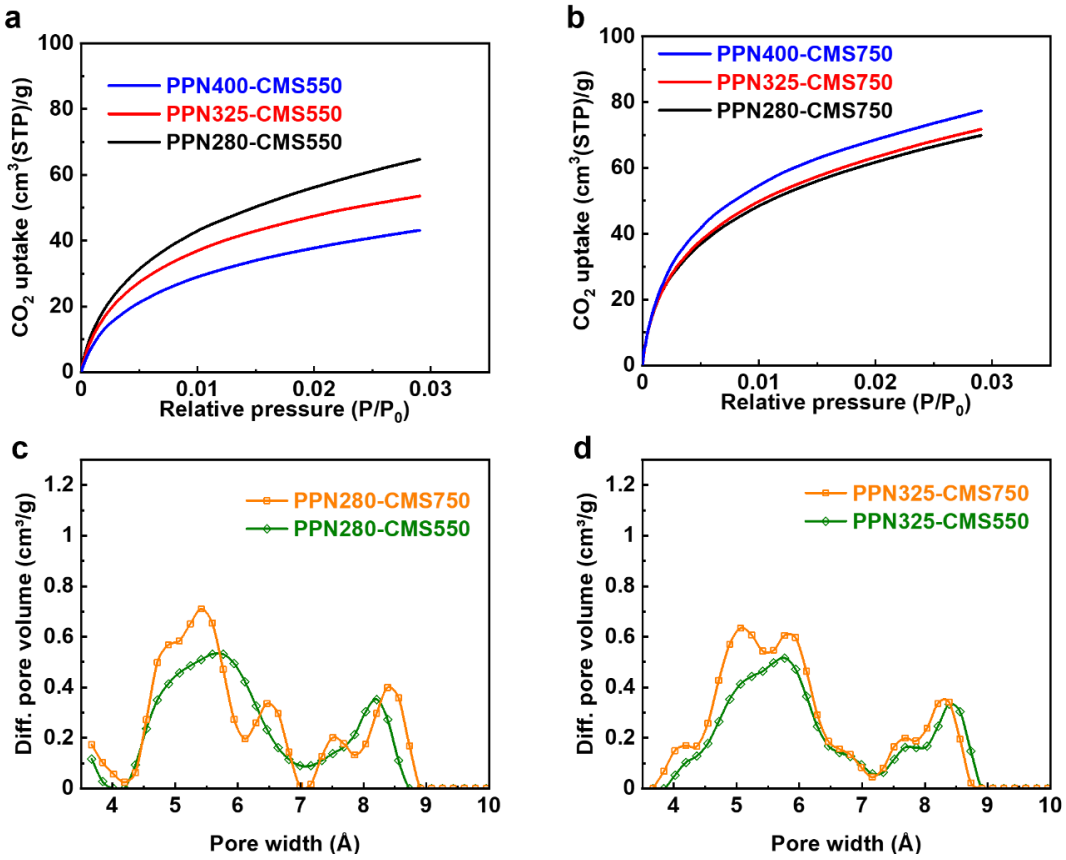

Figure 5.5 CO_2 adsorption analysis of PPN-CMS at 273 K. (a) CO_2 uptake of PPN-CMS550 and (b) PPN-CMS750 with respect to curing temperature. (c) DFT pore size distribution of PPN-CMS derived from PPN280 and (d) PPN325 with respect to pyrolysis temperature.

5.2.2.2 Effect of curing treatment on microstructure characteristics of PPN-CMS membranes

The effect of curing treatment was studied to understand the morphology and microstructure characteristics of the supported PPN-CMS membranes in relationship to curing temperature (**Figure 5.6**). The carbon layer thickness was about 1.4 μm for all the PPN-CMS550 membranes and about 1.0 μm for all the PPN-CMS750 membranes (**Figure 5.6(a)**). It was hypothesized that the cured PPN network with tunable

intermolecular distance and π-π stacking could shape the derived carbon microstructure arrangement. Interestingly, the trends in the d-spacing values of both PPN-CMS550 and PPN-CMS750 membranes agreed with the trends in the d-spacing values and glass transition temperature of the cured PPN precursors with respect to curing temperature (**Table 5.1**). These results indicated that the cured PPN precursors with greater polymer chain rigidness could produce a greater extent of loosely packed region in the PPN-CMS membranes. A comparison of the pore size distribution of PPN-CMS550 membranes also shows an increase in micropore size (**Figure 5.6(b)**). Notably, in contrast to the PPN280-CMS550 membrane, PPN325-CMS550 and PPN400-CMS550 membranes exhibited a narrower pore size distribution in the ultramicropore range (< 7 Å). This phenomenon suggested that the PPN325 and PPN400 precursors with ordered π-π stacking arrangement might promote the formation of small and uniform ultramicropores. Further increasing the pyrolysis temperature to 750 ℃ resulted in the formation of more ultramicropores in the PPN-CMS750 membranes, as mentioned in ***Chapter 5.2.2.1***. In particular, both PPN325-CMS750 and PPN400-CMS750 membranes showed more ultramicropores around 4 Å than PPN280-CMS750 (**Figure 5.6(c)**). The PALS pore size distribution analysis confirmed that PPN325-CMS750 and PPN400-CMS750 membranes exhibited narrowed ultramicropore distribution in contrast to PPN280-CMS750 (**Figure 5.6 (d)**). Furthermore, comparing the PPN400-CMS750 membrane with PPN280-CMS750 membrane, the τ_3 values of ultramicropores reduced to 1.84 ns from 2.15 ns, indicating the ultramicropore radius narrowed to 2.71 Å from 2.99 Å (**Table 5.3**). This result was mainly attributed to the existence of ordered π-π stacking region in the PPN400 network. The π-π stacking region in the polymer precursor is beneficial to the formation of π-π stacking carbon nanosheet region in the carbon matrix [143]. In short,

the cured PPN network with enlarged d-spacing and promoted π-π stacking could generate the PPN-CMS membrane with enlarged average intermolecular distance and small-sized, narrow-distributed ultramicropores.

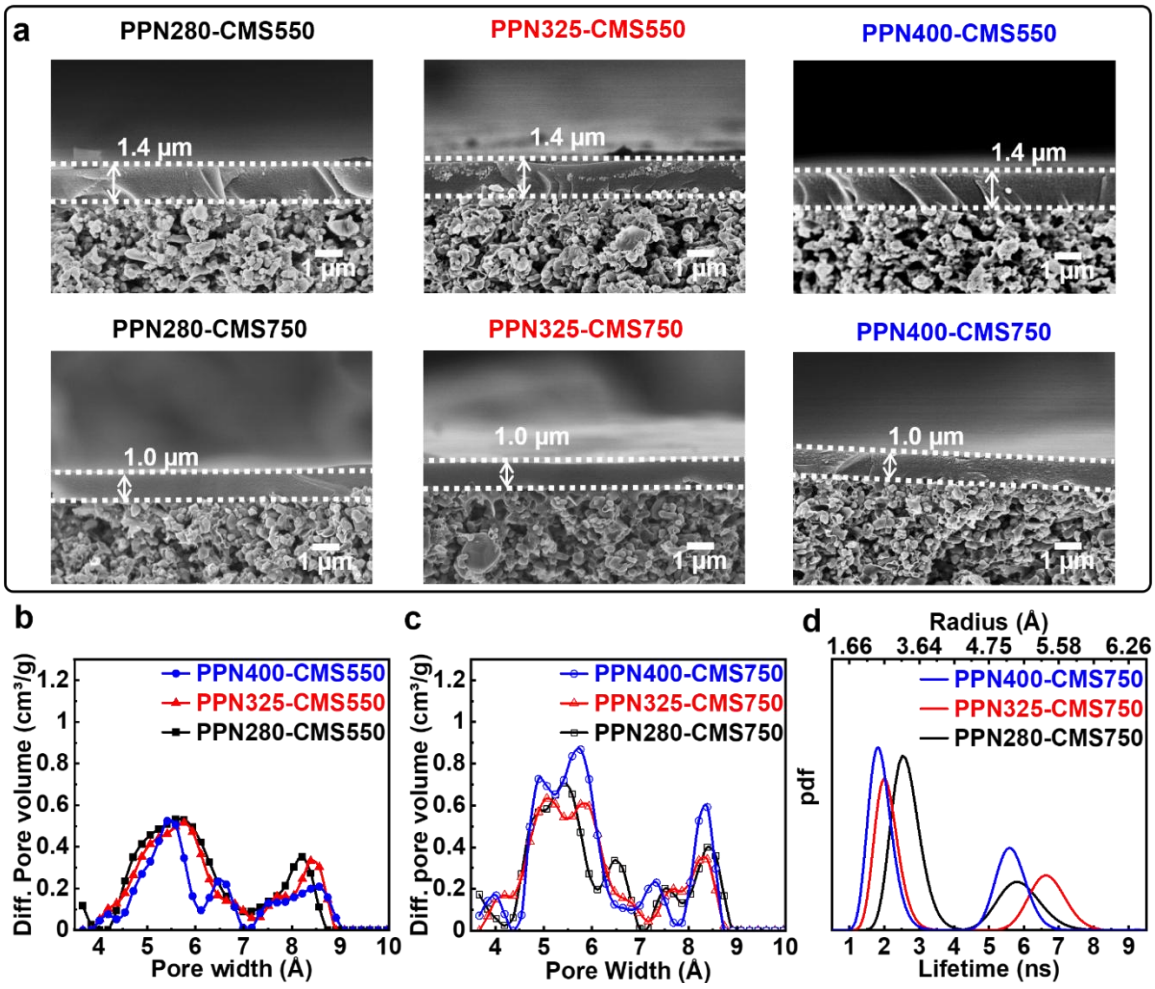

Figure 5.6 Effect of curing temperature on microstructure characteristics of PPN-CMS membranes. (a) FESEM cross-section morphology of supported PPN-CMS550 and PPN-CMS750 membranes. (The value represented mean thickness of the carbon layer with the dashed line as an eye-guide.) (b) DFT pore size distribution of PPN-CMS550 and (c) PPN-CMS750 membranes with respect to curing temperature. (d) PALS pore size distribution of PPN-CMS750 membranes with respect to curing temperature.

Table 5.3 PALS analysis on microstructure characteristics of PPN-CMS with respect to curing temperature.

Membranes	ultramicropore			micropore		
	τ_3 (ns)	I_3 (%)	Radius (Å)	τ_3 (ns)	I_3 (%)	Radius (Å)
PPN280-CMS750	2.15	10.4	2.99	4.15	5.2	4.33
PPN325-CMS750	2.03	8.4	2.88	5.53	5.3	4.99
PPN400-CMS750	1.84	9.4	2.71	4.54	4.8	4.53

5.2.3 Gas permeation analysis on PPN and PPN-CMS membranes

5.2.3.1 Gas permeation analysis on supported PPN membranes

The effect of the microstructure arrangement of the supported PPN and PPN-CMS membranes on their gas permeation behavior was studied. Gas molecules with precision sizes could probe subtle microstructure differences in membranes [133, 179]. As expected, the gas permeability of all the PPN membranes followed the reverse order of gas kinetic diameter: CO_2 (3.30 Å) > O_2 (3.46 Å) > N_2 (3.64 Å). The gas permeability of PPN membranes gradually increased with increasing curing temperature (**Figure 5.7(a)** and **Table 5.4**). This result was attributed to the formation of bulky and rigid phthalonitrile-derived moieties that enlarged the intermolecular distance of the PPN network, providing less gas transport resistance (**Table 5.1**). Specifically, the CO_2/N_2 and O_2/N_2 selectivities of the PPN325 membrane were improved by approximately 30% and 59%, respectively, compared with those of the PPN280 membrane (**Figure 5.7(b)** and **Table 5.4**). This improvement was attributed to a π-π stacking region in the PPN325 network. In contrast to the PPN325 membrane, the CO_2 and O_2 permeabilities of the PPN400 membrane were improved by 7.2 and 6.5 times, respectively. This effect is

because of the increased intermolecular distance of the PPN400 membrane by 0.99 Å. The CO_2/N_2 and O_2/N_2 selectivities of the PPN400 membrane slightly decreased by 4.3% and 9.7%, respectively, compared with those of the PPN325 membrane. The reason might be the increase of intermolecular distance in both amorphous and π-π stacking regions, allowing larger gas molecules to pass through. In a word, the enlargement of average intermolecular distance and the presence of the π-π stacking region benefited both gas permeability and ideal selectivity of the PPN membranes.

Table 5.4 Gas separation performance of supported PPN membranes with respect to curing temperature.

Membrane	Permeability (Barrer*)			Ideal selectivity (α)	
	CO_2	O_2	N_2	CO_2/N_2	O_2/N_2
PPN280	0.43 ± 0.01	0.095 ± 0.006	0.024 ± 0.001	17.8 ± 0.9	3.9 ± 0.3
PPN325	0.61 ± 0.09	0.17 ± 0.01	0.026 ± 0.002	23.1 ± 4.0	6.2 ± 0.6
PPN400	4.4 ± 0.3	1.1 ± 0.2	0.2 ± 0.02	22.1 ± 2.6	5.6 ± 1.1

5.2.3.2 Effect of pyrolysis temperature on gas permeation behavior of PPN-CMS membranes

The supported PPN-CMS membranes derived from the PPN precursors showed significant improvement in gas permeability (**Table 5.5**). The CO_2, O_2, and N_2 permeabilities of the PPN400-CMS550 membrane were 7623 Barrer, 2625 Barrer, and 1082 Barrer, respectively, which were approximately three orders of magnitude (1730 times, 2380 times, and 5410 times, respectively) higher than those of the PPN400 membrane (**Figure 5.7(a)**). Notably, the increased ratio of N_2 permeability of the

PPN400-CMS550 membranes was higher than CO_2 or O_2 permeability, resulting in the lower ideal CO_2/N_2 and O_2/N_2 selectivities, respectively, in contrast to the polymeric precursor (**Table 5.4** and **Table 5.5**). This effect was attributed to the pyrolyzed PPN, which formed a bimodal distribution of micropore and ultramicropore in the carbon matrix, giving different gas transport behavior. The micropores and ultramicropores of PPN-CMS550 membranes were large enough to provide an efficient gas permeation pathway for gas molecules, even ones with larger sizes. As the pore size of carbon membranes was at the micropore level, the effect of Knudsen and surface diffusion became competitive to the effect of molecular sieving in gas permeation [141]. Nonetheless, the effect of molecular sieving dominated the gas transport behavior of the PPN-CMS membranes, resulting in the gas selectivity higher than the Knudsen diffusion selectivity (**Figure 5.7(b)**). Further increasing the pyrolysis temperature to 750 ℃ reduced the gas permeability of the PPN400-CMS750 membrane, in contrast to that of the PPN400-CMS550 membrane. The main reason was the narrowed intermolecular distance of the carbon matrix pyrolyzed at the higher temperature (**Figure 5.3(b)** and **Table 5.1**). Nonetheless, the CO_2/N_2 and O_2/N_2 selectivities of the PPN400-CMS750 membrane were about 7.4 and 4.2 times higher than those of the PPN400-CMS550 membrane (**Figure 5.7(b)**). This improvement was attributed to a greater amount of narrower ultramicropores, providing a greater molecular sieving ability to the PPN400-CMS750 membrane (**Figure 5.3(c-d)**). In contrast to the PPN400 membrane, the PPN400-CMS750 membrane showed a significant improvement in CO_2 and O_2 permeabilities from 4.4 Barrer to 3568 Barrer (810 times), and from 1.1 Barrer to 760 Barrer (690 times), respectively. Furthermore, the CO_2/N_2 and O_2/N_2 ideal selectivities of the PPN400-CMS750 membrane increased to 58.7 and 12.5, respectively, which are

approximately 120% and 170%, respectively, higher than those of the PPN400 membrane (**Figure 5.7(a-b)**). This phenomenon can be explained by the fact that micropores provided high gas permeability, while ultramicropores benefited the molecular sieving ability of CMS membranes. As a result, the carbonization of the PPN membrane realizes an efficient molecular sieving ability of the derived PPN-CMS membrane, whose gas separation performance could be adjusted and advanced via pyrolysis temperature.

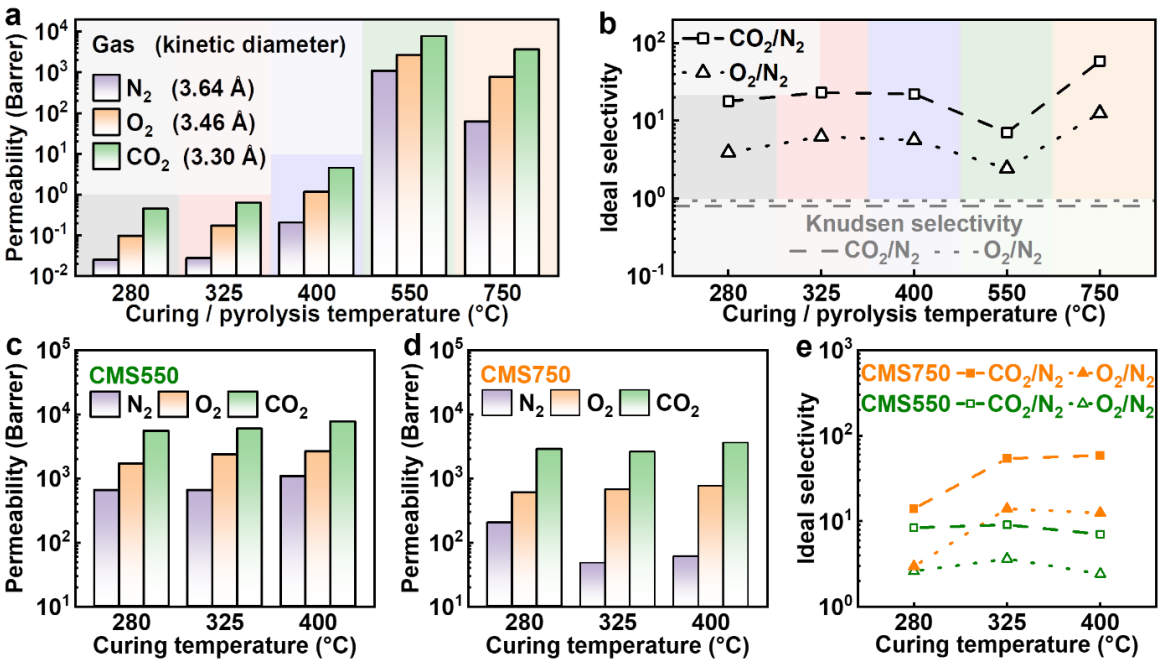

Figure 5.7 Gas permeation of supported PPN and PPN-CMS membranes. (a) N_2, O_2, and CO_2 permeabilities of the supported PPN and PPN-CMS membranes with respect to thermal treatment temperatures. (b) CO_2/N_2 and O_2/N_2 ideal selectivities of the supported PPN and PPN-CMS membranes with respect to thermal treatment temperatures. (c) Gas permeability of PPN-CMS550 membranes. (d) Gas permeability of PPN-CMS750 membranes. (e) CO_2/N_2 and O_2/N_2 ideal selectivities of PPN-CMS membranes.

5.2.3.3 Proposed mechanism on evolution of microstructure arrangement of PPN-CMS membranes with the effect of molecular chain arrangement of PPN precursors

The comparison of the gas permeation behavior of the supported PPN-CMS membranes further reveals the effect of the molecular arrangement of the PPN precursor on the microstructure arrangement of the derived PPN-CMS. For the supported PPN-CMS550 membranes, the gas permeability for all gas species increased with the curing temperature (**Figure 5.7(c)** and **Table 5.5**). This result was consistent with the increasing trend of the d-spacing values of the PPN and PPN-CMS550 membranes (**Table 5.1**). Given the highly rigid nature of the thermally cured PPN network, it was inferred that the polymeric network with a larger intermolecular distance produced the PPN-CMS550 membranes with a looser packing carbon matrix, resulting in higher gas permeability. Notably, the PPN325-CMS550 membranes exhibited higher gas selectivity than the PPN280-CMS550 membranes. This effect was mainly attributed to the narrower ultramicropore distribution derived from a more ordered π-π stacking region in the PPN325 precursor. The PPN400-CMS550 membrane, however, showed higher gas permeability but lower selectivity than both the PPN280-CMS550 and the PPN325-CMS550 membranes (**Table 5.5**). This result agreed with the gas separation performance of CMS membranes pyrolyzed at 550 ℃ obtained from the crosslinkable copolyimide precursors with and without curing treatment at 400 ℃ [145]. The CMS membrane from the crosslinked precursor with a larger intermolecular distance exhibited higher gas permeability but lower selectivity, indicating the permeability-selectivity trade-off behavior [145]. The results indicated that the effect of π-π stacking of the PPN400 network might not be able to fully overcome the effect of intermolecular distance of the precursor on the molecular sieving ability of the

derived PPN400-CMS550 membrane. A plausible reason was that the heterocyclic moieties that formed π-π stacking might not fully convert into a tightly packed carbonaceous structure at the relatively low pyrolysis temperature of 550 ℃.

Table 5.5 Effect of curing temperature and pyrolysis temperature on the gas permeation behavior of supported PPN-CMS membranes.

Membrane	Permeability (Barrer*)			Ideal selectivity (α)	
	CO_2	O_2	N_2	CO_2/N_2	O_2/N_2
PPN280-CMS550	5442 ± 471	1688 ± 239	649 ± 181	8.4 ± 2.5	2.6 ± 0.8
PPN325-CMS550	5917 ± 958	2369 ± 399	652 ± 261	9.1 ± 3.9	3.6 ± 1.6
PPN400-CMS550	7623 ± 166	2625 ± 52	1082 ± 46	7.0 ± 0.3	2.4 ± 0.1
PPN280-CMS750	2836 ± 193	601 ± 72	202 ± 50	14.0 ± 3.6	3.0 ± 0.8
PPN325-CMS750	2583 ± 159	667 ± 60	47.9 ± 7.5	53.9 ± 9.1	13.9 ± 2.5
PPN400-CMS750	3568 ± 326	760 ± 166	60.8 ± 6.9	58.7 ± 8.6	12.5 ± 3.1

The elevated pyrolysis temperature could improve the gas selectivity but reduce the gas permeability of PPN-CMS membranes, as discussed in ***Chapter 5.2.3.2***. As expected, despite the decreased gas permeability of PPN-CMS750 membranes (**Figure 5.7(c-d)**), the ideal selectivity of PPN-CMS750 membranes was consistently higher than that of PPN-CMS550 membranes with respect to curing temperature (**Figure 5.7(e)** and **Table 5.5**). This effect was attributed to more ultramicropores, improving the gas selectivity of the PPN-CMS750 membranes. Interestingly, both CO_2/N_2 and O_2/N_2 selectivities of PPN325-CMS750 and PPN400-CMS750 membranes were improved about three times, while CO_2 and O_2 permeabilities remained at a similar level, in contrast to those of the PPN280-CMS750 membrane (**Figure 5.7(d-e)**). It was inferred that the ultramicropores

with smaller size and narrower distribution of PPN325-CMS750 and PPN400-CMS750 membranes were the dominant effect that hindered the transport of larger gas molecules (N_2) but allowed the smaller gas molecules (CO_2 and O_2) (**Figure 5.6(c-d)**). The small-sized and narrow-distributed ultramicropores were pyrolyzed from the π-π stacking of the cured PPN network, as discussed in ***Chapter 5.2.2.2***. These results supported the hypothesis that the enlarged intermolecular distance and π-π stacking of PPN contributed to improving the molecular sieving ability of PPN-CMS membranes (**Figure 5.8(a)**). Overall, the tunable microstructure arrangement of PPN could effectively adjust the microstructure characteristics and the gas permeation behavior of PPN-CMS membranes.

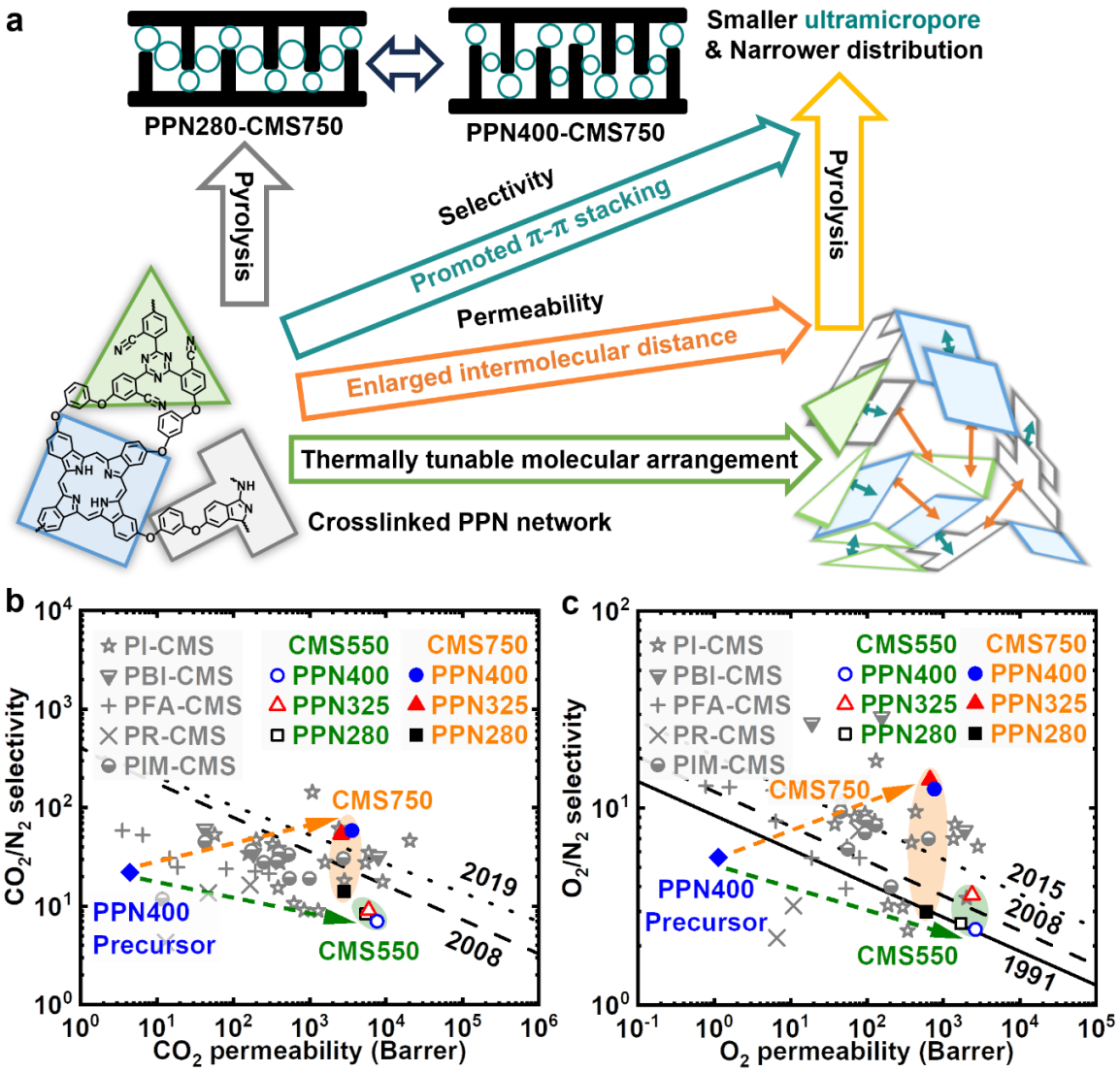

Figure 5.8 Proposed mechanism on PPN-CMS membranes for gas separation. (a) Schematic diagram of the influence of molecular chain arrangement of PPN precursor on evolution of microstructure arrangement of PPN-derived microporous carbon and its gas permeation behavior. (b) CO_2/N_2 and (c) O_2/N_2 Robeson upper bound relationship of supported PPN and PPN-CMS membranes in comparison to CMS membranes derived from various precursors (PI: polyimide [49, 69, 100, 143-146], PBI: polybenzimidazole [146, 147], PFA: poly(furfuryl alcohol) [69, 162, 164], PR: phenolic resin [167], PIM: polymer of intrinsic microporosity [143, 148]).

The relationship between the supported PPN and PPN-CMS membranes was investigated by comparing their ideal gas separation performance to CO_2/N_2 and O_2/N_2 Robeson upper bound relationship for polymeric membranes (**Figure 5.8(b)** and **Figure 5.8(c)**) [60, 63, 69, 149, 150]. Above the upper bounds of polymeric membranes, CMS membranes also exhibited a permeability-selectivity trade-off relationship [69]. Carbonization of the PPN membranes produced the PPN-CMS membranes with significantly improved CO_2 and O_2 permeabilities, either approaching or above the respective upper bounds of polymer membranes. Notably, PPN-CMS membranes possessed superior gas permeability than CMS membranes derived from thermosetting polymeric precursors, such as PFA and PR resins (**Figure 5.8(b-c)** and **Table S1**). This result could be explained by the fact that the high glass transition temperature of the cured PPN network was beneficial to the high gas permeability of PPN-CMS membranes. Specifically, the PPN325-CMS750 and PPN400-CMS750 membranes exhibited improved ideal CO_2/N_2 and O_2/N_2 selectivities while maintaining high CO_2 and O_2 permeabilities compared to those of the PPN280-CMS750 membrane. This result was mainly attributed to the more ordered π-π stacking arrangement of PPN325 and PPN400 precursors, resulting in smaller and narrower ultramicropore size and distribution of PPN325-CMS750 and PPN400-CMS750 membranes. Interestingly, both PPN325-CMS750 and PPN400-CMS750 membranes showed comparable ideal gas separation performance of CMS membranes obtained from high decomposition temperature polymers (PI, PBI, and PIM) (**Figure 5.8(b-c)** and **Table S1**) [69]. It should be noted that the study on the actual gas separation performance of a CMS membrane requires a mixed-gas test and operation conditions close to industrial applications, which is beyond our research scope and instrument capacity in the lab. For the first time, nonetheless, this work evaluated the fundamental gas permeation

behavior of PPN-CMS membranes in comparison to the ideal separation performance of other CMS membranes as a basis for future study. More importantly, this study demonstrated that the thermally tunable intermolecular distance and π-π stacking of PPN precursor are critical factors in adjusting the microstructure characteristics and gas permeation behavior of PPN-CMS membranes. Apart from the thermal treatment process, the flexibility of the chemical synthesis of PPN-based materials offers unique opportunities as a platform for exploring microstructure design at the molecular level for polymeric and CMS membranes [2, 11, 12, 20, 170, 172, 173, 175, 176, 180-184]. Besides, PPN possesses electron donor/acceptor moieties that provide miscibility to polymer blends [109], promising incorporation with other high-performance polymeric precursors (i.e., polyimide) for CMS membrane fabrication. In summary, this work provides new insights into the evolution of the microstructure arrangement of the PPN-derived carbon materials, and elucidates the influence of the microstructure arrangement of PPN precursors on the gas permeation behavior of the PPN-CMS membranes.

5.3 Conclusion

This study demonstrated thermally crosslinkable polyphthalonitrile (PPN) with both tunable intermolecular distance and π-π stacking arrangement as a novel precursor for fabricating high-performance carbon molecular sieve (CMS) membranes. The relationship between the microstructure characteristics and the gas permeation behavior of the PPN-derived CMS membranes was systematically studied. Furthermore, the mechanism of evolution of the microstructure arrangement of the PPN network and PPN-derived microporous carbon was proposed. Thermal analysis revealed that the crosslinked

PPN network possessed high decomposition temperature, glass transition temperature, and char yield. Microstructure analysis revealed the thermally tunable microstructure arrangement of the PPN network, and it was further confirmed by the gas permeation analysis. In contrast to the PPN280 membrane, both PPN325 and PPN400 membranes subjected to higher curing temperatures exhibited more ordered π-π stacking arrangement. Furthermore, the PPN400 membrane showed an enlarged average intermolecular distance owing to the crosslinking of phthalonitrile moieties, while its ordered segment arrangement was retained. Consequently, both CO_2 and O_2 permeabilities of the PPN400 membrane improved approximately ten times, and CO_2/N_2 and O_2/N_2 selectivities enhanced by 24% and 43%, respectively, compared with those of PPN280 membranes. Carbonization of PPN precursors produced PPN-CMS membranes with improved gas permeability due to the formation of a bimodal pore size distribution of microporous carbon. Among all the PPN-CMS membranes, the PPN400-CMS550 membrane exhibited a larger intermolecular distance, leading to its high gas permeability but compromised selectivity. In contrast to the PPN400-CMS550 membrane, the PPN400-CMS750 membrane exhibited a greater amount of ultramicropores and a narrower pore size distribution, resulting in higher CO_2/N_2 and O_2/N_2 selectivities (7.4 and 4.2 times, respectively). It was identified that the ordered π-π stacking arrangement of PPN400 membranes contributed to the formation of small-sized and narrow-distributed ultramicropores of the derived PPN400-CMS750 membranes. Consequently, both CO_2/N_2 and O_2/N_2 selectivities (58.7 and 12.5, respectively) of the PPN400-CMS750 membrane were improved by approximately three times in comparison to those of the PPN280-CMS750 membrane, while its high CO_2 (3568 Barrer) and O_2 permeabilities (760 Barrer) were maintained at the same level. The facile microstructure

tunability of PPN makes this type of polymer a potential candidate for developing CMS membranes.

Chapter 6

Adjustable microstructure and gas transport properties of PPN/PI membrane

The increasing demand for hydrogen production has necessitated the development of H_2-selective membranes. Polyimides are excellent membrane materials for gas separation; however, commercial polyimides generally lack sufficient H_2 selectivity due to their low H_2 affinity. Understanding the relationship between gas transport properties and free volume microstructure is critical to advancing H_2-selective membrane design. Herein, this chapter reports a facile material strategy to adjust the free volume characteristics and H_2 separation performance via blending Matrimid (PI) and crosslinkable phthalonitrile prepolymer (PPN) with electron donor/acceptor properties. The novel PPN30/PI70 membrane exhibits H_2/N_2 and H_2/CO_2 permselectivity of 1637 and 66.4, respectively, with H_2 permeability of 2.7 Barrer in pure gas test, surpassing Robeson upper bounds (2008). The increased H_2 permselectivity of PPN/PI blend membranes was attributed to the narrowed free volume size and distribution, giving rise to the improved H_2 solubility and solubility selectivity. Moreover, thermal treatment can further improve the H_2 permeability of crosslinked PPN30/PI70 membranes. The H_2/CO_2 mixed-gas test revealed the influence of plasticization and competitive sorption on H_2 separation performance of the PPN30/PI70 blend membrane. This study demonstrates a new versatile strategy for designing high-performance hydrogen selective polymeric membranes.

6.1 Introduction

The transition to the hydrogen economy has brought about a tremendous interest in gas separation technologies [72]. In contrast to traditional separation processes like distillation, membrane gas separation holds several advantages, such as low capital cost, excellent processability, and low energy consumption. Membranes based on polymeric materials have been investigated in various gas separation applications, such as carbon dioxide capture, ammonia production, and hydrogen purification[185, 186]. Glassy polymers such as polybenzimidazoles [187, 188], polyethersulfones [188], and polyimides [40, 188-190] have been studied as materials for membrane fabrication. These glassy polymers possess excellent size-sieving abilities because of the rigid and chemically stable molecular chains, making them suitable for membrane separation applications. Gas permselectivity of polymeric membranes can be described as the product of solubility selectivity and diffusivity selectivity [157]. Solubility selectivity depends on the penetrant condensability, penetrant-polymer interactions, and fractional free volume; diffusivity selectivity is mainly affected by the penetrant size, polymer chain flexibility, and interchain distance of the membrane [72]. The glassy polymer with rigid backbones is kinetically favorable to the diffusion of smaller penetrants such as H_2 (2.89Å) compared to larger counterparts such as CO_2 (3.3Å) or N_2 (3.64Å), resulting in desirable H_2 diffusivity selectivity [157]. It is generally believed that the effect of H_2 solubility selectivity often compromises the overall permselectivity of polymeric membranes [72, 185]. This is mainly due to the fact that polymers typically have inherently lower H_2 solubility coefficients because H_2 has weaker condensability (27 K) in comparison to N_2 (71 K) and CO_2 (195 K).

Polyimides are widely used in fabricating gas separation membranes owing to their excellent mechanical properties, processability, and gas permeability. However, the wide free volume distribution of polyimide results in low permselectivity of H_2 over CO_2 and N_2, limiting its potential in hydrogen production [72, 185, 188, 191]. Several methods can adjust the permselectivity of polyimides, including chemical crosslinking [39, 192-194], backbone modification [195], and polymer blending [86, 187, 196, 197]. Using diamine monomer to tailor the microstructure of the polyimide could improve the H_2 permselectivity due to the enhancement in the diffusivity selectivity while maintaining the solubility selectivity [192]. However, Wang *et al.* [198] found that excess pendant amino moiety in the surface-modified polyimide might facilitate CO_2 transport, resulting in compromised H_2/CO_2 permselectivity. Besides, the amino-crosslinked polyimides had a few drawbacks, such as increasing brittleness and the potentially reversible crosslinking reaction at certain operation conditions, which hindered their applications [194, 199, 200]. Designing new types of high-performance polymers, including polyimides, has been proven to be a practical way to improve the solubility selectivity of polymeric membranes to surpass the permeability-selectivity trade-off, particularly in CO_2 capture [59, 157]. Improving solubility selectivity is another approach to improving permselectivity. A few studies focused on improving the H_2 solubility selectivity over other gas species. Recently, Zhang *et al.* [195] proposed that incorporating an alicyclic group into the structure of microporous polyimides could lead to smaller but homogeneous free volume cavity size and distribution, which could be beneficial to H_2 solubility selectivity over other larger gas species. Therefore, improving the molecular chain packing efficiency to generate narrowly distributed free volume microstructure has become a feasible strategy to tackle the problem of limited hydrogen permselectivity of

polyimides. However, the high H_2 solubility selectivity of these polyimides was countervailed by the decreased H_2 diffusivity selectivity, resulting in the moderate improvement of H_2 permselectivity [195].

The blending of polymers is a versatile and practical strategy for designing new polymeric materials for gas separation. From thermodynamical considerations, however, only limited combinations of polymers can form fully miscible blends with stable and predictable gas separation performance [86]. Nevertheless, several partially miscible blend systems have demonstrated that intermolecular interactions between polymers significantly influence the microstructure at the molecular level and influence the gas separation performance of the membrane. Patrício *et al.* [201] postulated that the existence of intermolecular interactions, such as hydrogen bond interaction, between polymethylmethacrylate (PMMA) and polyurethane (PU) contributes to the formation of partially miscible blend. Incorporating 40 wt% PMMA into the PU matrix led to a reduction in the o-positronium lifetime (τ_3) from 2.32 to 2.17 ns (analog to free volume cavity size) and a 125% increase in H_2/N_2 permselectivity compared to pure PU membranes [201]. They concluded that the improvement of H_2 permselectivity was attributed to both phase arrangement and modified microstructure of PMMA/PU blends [201]. Yong *et al*. [196] reported that incorporating a polymer with intrinsic microporosity (PIM-1) with polyimide (Matrimid) resulted in a partially miscible blend due to the formation of an intermolecular charge-transfer complex (CTC) between the two polymers. The addition of 5 wt% PIM-1 to Matrimid increased the fractional free volume (FFV) to 18.3% from 16.5%, leading to a 24 % improvement in O_2 permeability compared to neat Matrimid; additionally, a slight increase in O_2/N_2 permselectivity of 3%

was attributed to the presence of intermolecular CTC [196]. More recently, Mazinani *et al.* [24] proposed that blending 20 wt% polyethersulfone (PES) with polyetherimide (Extem) resulted in substantial enhancement in both CO_2 permeability and CO_2/N_2 permselectivity compared to the neat components. They postulated that the increased polarity of the PES/Extem (20/80) blend favored CO_2 solubility, leading to a remarkable 162% increase in CO_2 permeability; furthermore, the reduced FFV and the enhanced polarity likely contributed to improved CO_2/N_2 diffusivity and solubility selectivity, respectively, resulting in a significant 293% increase in CO_2/N_2 permselectivity compared to pure Extem membrane [202]. In short, the adjustment of free volume microstructure facilitated by intermolecular interactions plays a critical role in the gas separation performance of polymer blend membranes.

It was hypothesized that incorporating the resorcinol-based PPN into polyimide can tailor the intermolecular interactions and microstructure, enabling the adjustment of the hydrogen separation performance. The phthalonitrile prepolymer was chosen for its abundant triazine and phthalocyanine moieties. These moieties have electron donor/acceptor properties that can form intermolecular CTC in their respective covalent organic network thin-films [203-205]. On the other hand, polyimides composed of imide and diamine moieties are known to exhibit intermolecular CTC, which can be further enhanced by thermal treatment [196, 206, 207]. Therefore, it is rational to suggest that the phthalonitrile prepolymer can form the intermolecular CTC with polyimide. Besides, Tay *et al.* [3] found that incorporating resorcinol-based phthalonitrile prepolymer or oligomer (pPN) in polyacrylonitrile (PAN) enabled the formation of homogeneous and defect-free films, whereas the monomers tended to crystallize out of the blend during thermal

treatment. The thermally treated pPN/PAN polymer blend showed superior thermal stability to the pure components owing to the formation of the interpenetrating polymer network (IPN) [3]. To test the concept, the novel charge-transfer PPN/PI blend membranes with unusual hydrogen-selective properties and tunable microstructure at the molecular level was demonstrated. This chapter is focused on the PPN/PI membranes to identify (i) intermolecular interactions between the PPN prepolymer and polyimide, (ii) the free volume characteristics and tunability of the microstructure of PPN/PI blends, and (iii) gas transport properties of the PPN/PI membranes.

6.2 Results and discussions

6.2.1 Characteristics of intermolecular interactions of PPN/PI blends

PPN/PI blends were fabricated by mixing PPN as prepolymer with PI and characterized via FTIR-ATR to identify their chemical composition and intermolecular interactions (**Figure 6.1** and **Figure 6.2(a)**). For polymer blends, intermolecular interactions will result in a shift in frequency or change in intensity of the characteristic peak of the affected moieties. Conversely, if there are no intermolecular interactions between the two components, the new spectrum of the blends is presumably the addition of the two original spectra. The spectra of PI showed transmittance peaks of asymmetric C=O stretching at 1778 cm^{-1}, asymmetric C=O stretching at 1716 cm^{-1}, ketonic group of C=O at 1672 cm^{-1}, aromatic C=C stretching at 1487 cm^{-1}, N-C=O stretching at 1248, 1364, and 1425 cm^{-1}. The spectra of resorcinol-based PPN showed pendant nitrile at 2231 cm^{-1}, isoindolenine at 1770, 1718, and 1669 cm^{-1}, triazine at 1521 and 1358 cm^{-1}, aromatic

C=C stretching at 1471 cm^{-1}, C-O-C of aromatic ether at 1241 cm^{-1}, and phthalocyanine at 1002 cm^{-1} [190].

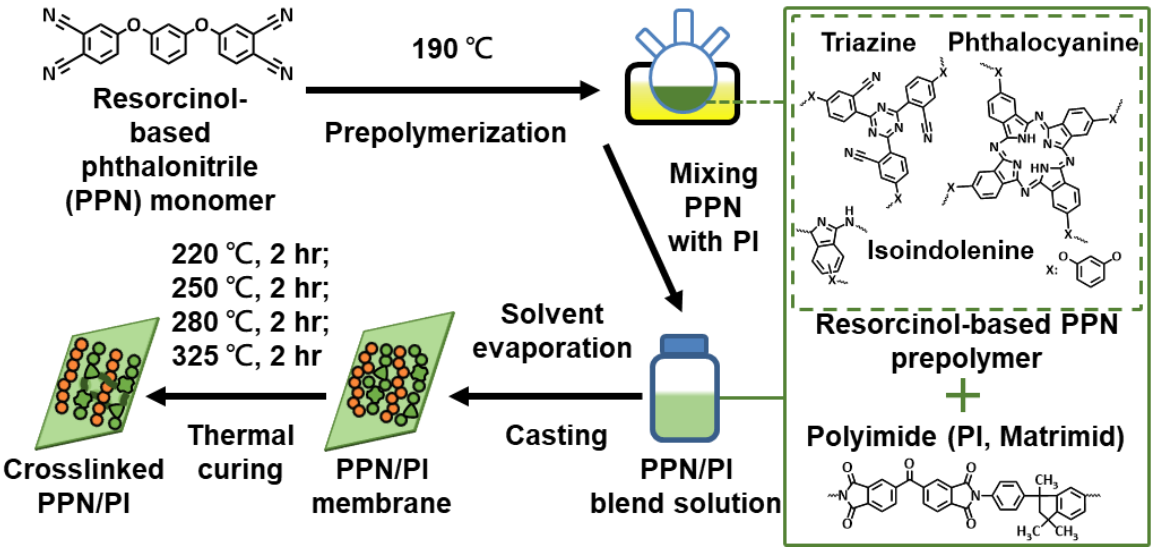

Figure 6.1 Schematic diagram of resorcinol-based phthalonitrile prepolymer/polyimide (PPN/PI) blend membrane fabrication.

Intermolecular interactions in polymers largely affect molecular chain arrangement, which is important for gas transport behavior. For PPN/PI thin films, the peak intensity of the nitrile group at 2231 cm^{-1} increased with the composition of PPN in the blends (**Figure 6.2(a)**). Notably, the triazine group of PPN/PI showed a dramatic decrease in peak intensity at 1521 cm^{-1} and a strong blue shift from 1358 cm^{-1} to 1371 cm^{-1}, exceeding the O=C-N stretching of PI at 1364 cm^{-1}. These results indicate the existence of intermolecular interaction leading to the change in electron cloud density of the triazine group. Besides, peak shift was observed in the range of 1247 cm^{-1} to 1241 cm^{-1}, involving both C-O-C of the resorcinol group and N-C=O stretching of the imide group. It was well known that the dianhydride and diamine moiety of PI have electron-withdrawing and electron-donating properties, respectively [196, 207]. For the PPN, the

triazine group with high electronegativity could serve as an electron acceptor, and the adjacent resorcinol group might be the electron-donating counterpart [208]. It was inferred that the electron donor-acceptor interaction exists in PPN/PI blends. The triazine and the adjacent resorcinol moieties of the PPN might form the intermolecular charge-transfer complex (CTC) with the diamine and dianhydride moieties of the PI, respectively. The formation of intermolecular CTC could affect the polymer chain arrangement of the PPN/PI matrix by narrowing the molecular chain packaging. Indeed, the existence of aromatic-aromatic stacking was observed from the peak shift of the aromatic C=C stretching of PPN/PI.

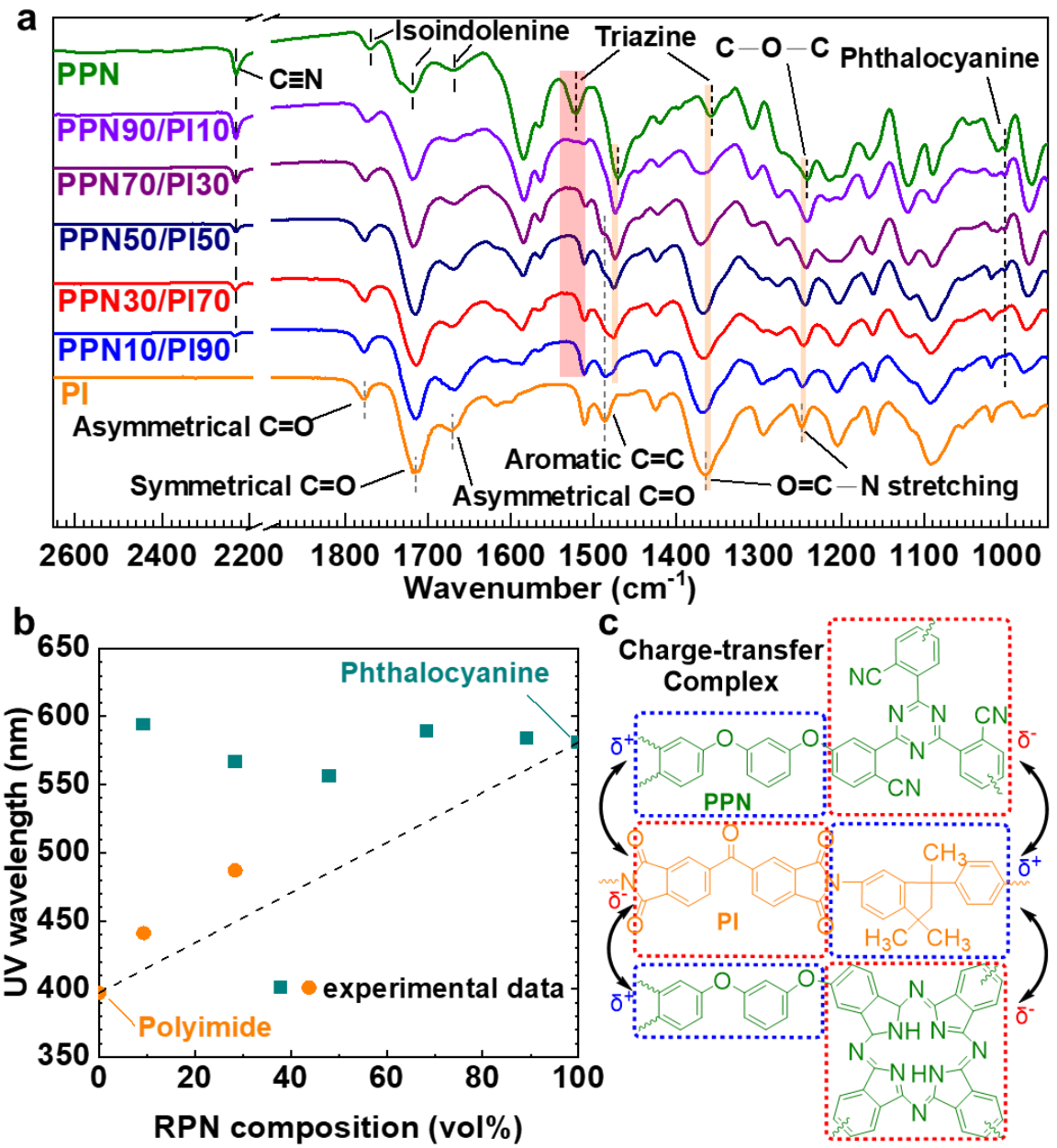

Figure 6.2 The characteristics of intermolecular interactions of PPN/PI blends. (a) FTIR-ATR spectrum (b) UV-Vis absorbance (dash line: additive law prediction to guide eye), and (c) scheme of proposed intermolecular charge transfer complex (CTC) of PPN/PI thin films.

It was further hypothesized that the intermolecular CTC between PPN and PI can also involve the phthalocyanine with the adjacent electron-donating resorcinol moiety. UV

absorbance test was carried out to validate the hypothesis [196]. In general, the change of UV absorbance band in a blend polymer system can be predicted via the additive law as the following equation:

$$\lambda_b = \emptyset_1\lambda_1 + (1-\emptyset_1)\lambda_2 \quad (6.1)$$

where λ_b, λ_1, and λ_2 are referred to as the maximum absorbance of the blend and the pristine polymers 1 and 2, respectively; $\emptyset_1$ is to the volume fraction of the pristine polymer 1. For miscible blends without CTC, the experimental data of the absorbance band of the blends should follow the additive law [196]. The intermolecular interactions enhance the miscibility of the two polymer components despite the presence of an aggregated phase in partially miscible blends [85]. Previous studies have suggested that the shift in the maximum absorbance wavelength of miscible (homogeneous) or partially miscible (heterogeneous) blends may be attributed to the formation of intermolecular CTC between the two polymers [85, 196]. The hypothesis was supported by the fact that the wavelengths of the obtained PPN/PI thin films significantly deviated from the predicted values in all ratios (**Figure 6.2(b)** and **Figure S3**). The UV-vis spectra of the PPN/PI blends exhibited similar characteristics to those of partially miscible polyimide blends, such as PIM/Matrimid blends [196] and c-PIM/Torlon blends [85]. The exact reason for the non-monotonic changes in the peak wavelengths is unclear. It could possibly be attributed to the complex intermolecular CTCs formed between the diamine and imide moieties of PI and the triazine and phthalocyanine groups of PPN. However, the incorporation of 70 and 90 wt% PPN with PI resulted in a significant red shift in the peak maxima, indicating the presence of intermolecular CTC between the PI and the

phthalocyanine moiety of PPN. From FTIR and UV-vis results above, one can safely prove the existence of both aromatic-aromatic interaction and intermolecular CTC between PPN and PI (**Figure 6.2(c)**). These intermolecular interactions will affect both the microstructure and chemical environment of the polymer blends, which can improve the hydrogen separation performance.

6.2.2 Thermal and microstructural properties of PPN/PI blends

6.2.2.1 Effect of chains interaction and thermal treatment on physical characteristics of the PPN/PI blends

DMA was utilized to estimate the glass transition behavior, which closely relates to the polymer chain rigidity that affects polymer chain arrangement and gas transport properties (**Figure 6.3(a)**). The glass transition temperature is defined as the local maximum value(s) of the tan delta, a ratio of loss modulus to storage modulus. Among the membranes, the pure PI showed the highest glass transition temperature of 339 °C due to the rigid backbone. For PPN/PI blends, it was inferred that the incorporation of PPN will increase chain mobility because the oligomer must insert between the backbones of PI to form intermolecular CTC. However, despite the presence of intermolecular CTCs, the effect of the oligomer on improving the flexibility of the polyimide chain could not be overcome, as observed by the decreased glass transition region in the PPN/PI blends. The intermolecular CTC could also contribute to the compatibility between PPN and PI. Polarized Light Microscopy (PLM) (**Figure 6.4**) and Field Emission Scanning Electron Microscopy (FESEM) **(Figure 6.5)** results confirmed that PPN/PI blends are phase-separated. However, the PPN/PI blends exhibited a broad

glass transition region with two distinguishable glass transition temperatures ((**Figure 6.3(a)** and **Table 6.1**). The first and lower glass transition temperatures (178 to 217 °C) may represent the PPN-rich phase, and the second and higher temperatures (252 to 293 °C) may be assigned as the PI-rich phase. The comparison between PPN30/PI70 and PPN10/PI90 confirmed that a higher content of PPN resulted in a lower glass transition region as well as glass transition temperatures. Based on these results, it was concluded that the PPN/PI blends are partially miscible owing to the intermolecular CTCs between PPN and PI. The lower but broader glass transition region provides insights into the influence of the increase in chain mobility on the microstructure of blend films.

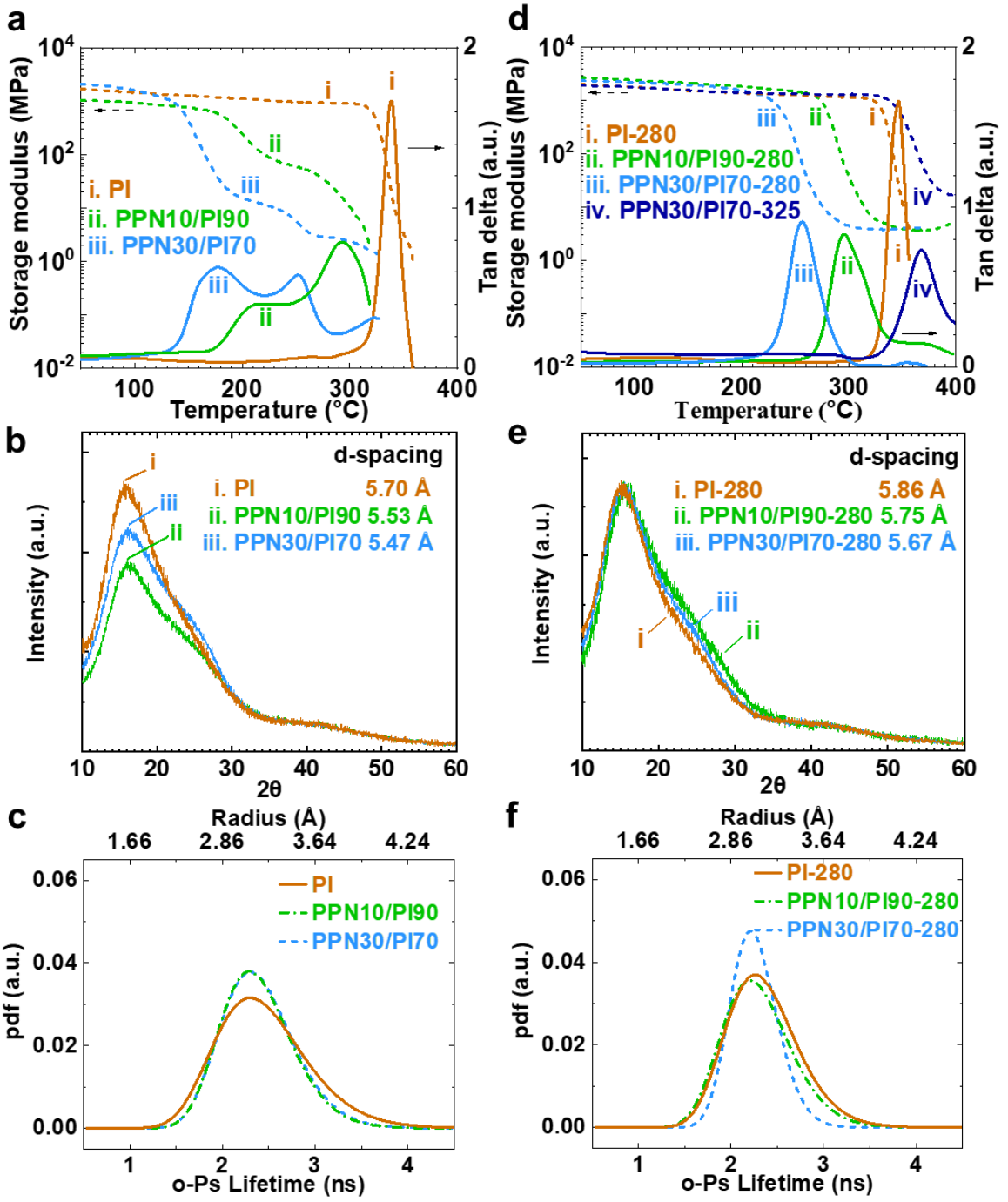

Figure 6.3 The effect of PPN composition on the polymer chain arrangement of (a, b, c) PPN/PI, and (d, e, f) thermally treated PPN/PI membranes. (a, d) Glass transition temperature, (b, e) XRD pattern, and (c, f) free volume distribution of PPN/PI membranes.

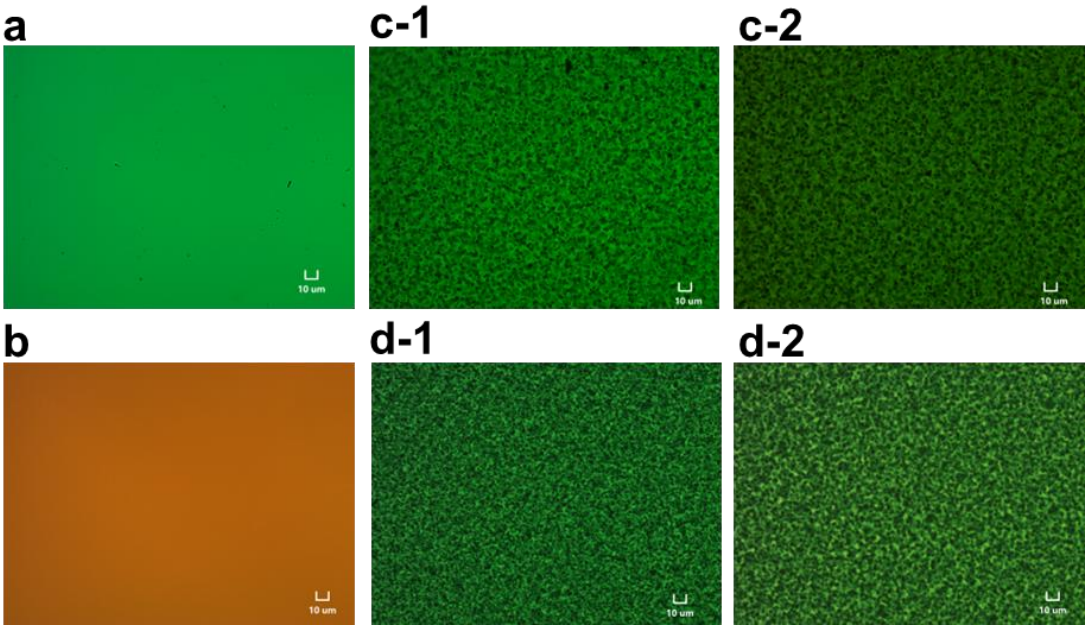

Figure 6.4 PLM microstructural morphologies. (a) PPN, (b) PI, (c-1) PPN10/PI90, (c-2) PPN10/PI90-280, (d-1) PPN30/PI70, (d-2) PPN30/PI70-280 membranes (scale bar: 10 um).

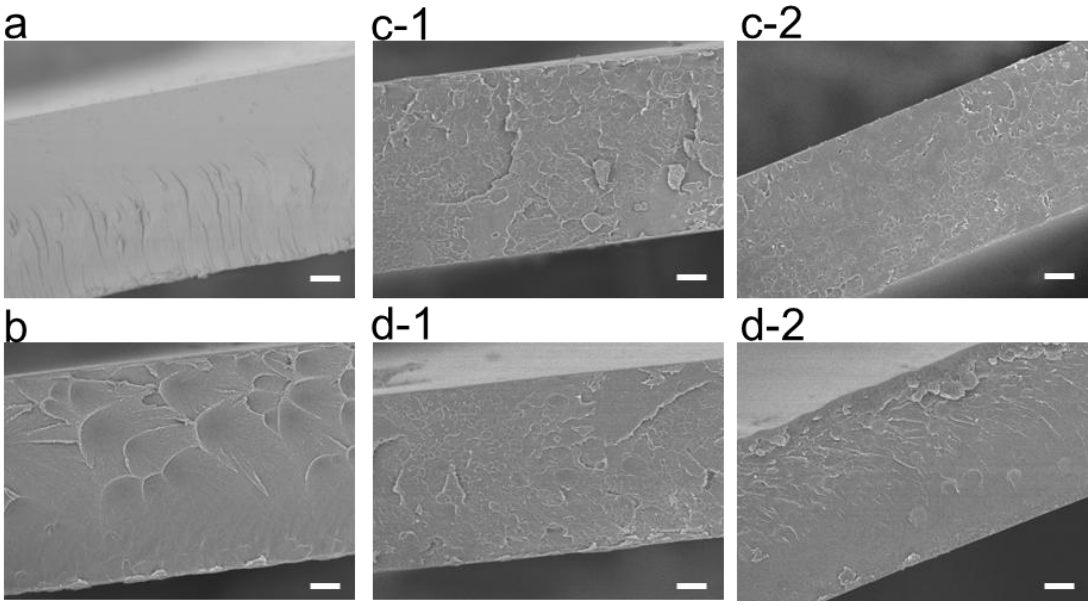

Figure 6.5 FESEM cross-section microstructural morphologies. (a) PPN-280, (b) PI, (c-1) PPN10/PI90, (c-2) PPN10/PI90-280, (d-1) PPN30/PI70, (d-2) PPN30/PI70-280 membranes (scale bar: 10 um).

The nitrile group of PPN in the PPN/PI blends can undergo further reaction above 220 °C, forming a crosslinked polymer network with triazine, phthalocyanine, and isoindolenine units [3]. Since there were no observable characteristics of chemical crosslinking between PPN and PI in FTIR-ATR results (**Figure 6.6**), it is reasonable to infer that the crosslinking may occur exclusively in PPN. Following thermal treatment at 280 °C, the PPN/PI blends transformed into semi-IPN membranes, referred to as PPN/PI-280, which exhibited partial solubility in the solvent (NMP). The fraction of gel content can indicate the degree of crosslinking in the semi-IPN membranes. As expected, a higher content of PPN led to a greater extent of crosslinked polymer network in PPN/PI-280 blends, resulting in a higher fraction of gel content (**Table 6.1**).

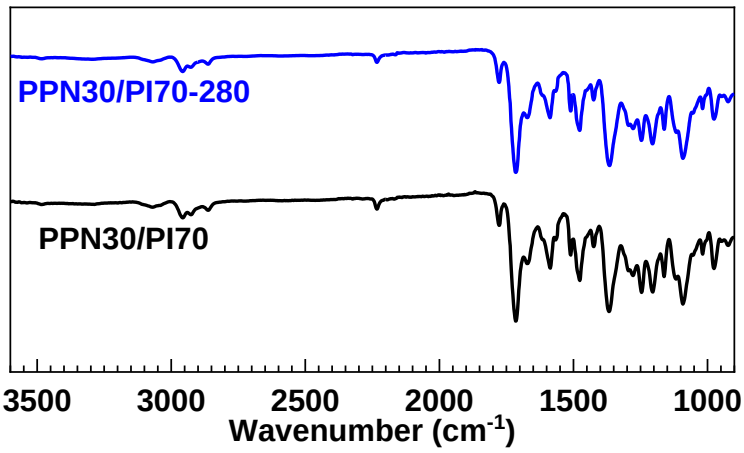

Figure 6.6 FTIR-ATR spectrum of PPN30/PI70 and PPN30/PI70-280 membranes.

Table 6.1 Glass transition temperature, interchain distance, and gel content of PPN/PI and PPN/PI-280 membranes.

Membranes	glass transition temperature	d-spacing	gel content
PI	339 °C	5.70 Å	Soluble
PPN10/PI90	217 °C, 293 °C	5.53 Å	Soluble
PPN30/PI70	178 °C, 252 °C	5.47 Å	Soluble
PI-280	346 °C	5.86 Å	Soluble
PPN10/PI90-280	296 °C	5.75 Å	54 %
PPN30/PI70-280	256 °C	5.67 Å	69 %

It was supposed that the chain rigidity of the PPN/PI matrix could be improved based on the thermally crosslinkable PPN by forming a semi-IPN microstructure after thermal treatment. Thermally treated PPN/PI blends exhibited only one glass transition temperature and a narrowed transition region ((**Figure 6.3(d)** and **Table 6.1**). The higher glass transition temperature of the thermally treated PPN/PI indicates a higher stiffness of the polymer backbone. It was inferred that the rigid linkages (triazine and phthalocyanine), resulting from the crosslinking of PPN, primarily contributed to the significant improvement in the chain rigidity of the PPN/PI semi-IPN blends compared to the untreated blends (**Table 6.1**). Interestingly, the glass transition temperature of PPN30/PI70-325 significantly exceeded that of PI (**Figure 6.3(d)** and **Figure 6.7(a)**). This result suggested that raising the thermal treatment temperature can enhance the chain rigidity of PPN/PI blends through the crosslinking of the oligomer. As expected, the glass transition temperature and thermal stability of PPN30/PI70 increased with thermal treatment temperature (**Figure 6.7(a-b**). Furthermore, the increasing trend of the gel fraction coincided with the trend of thermal stability (**Figure 6.7(d)**). These results

indicated that more rigid and thermally stable linkages were formed as the thermal treatment temperature increased. In contrast, no obvious difference was observed in the phase arrangement (**Figure 6.4** and **Figure 6.5**) and the chemical composition of the PPN/PI before and after thermal treatment (**Figure 6.6** and **Figure 6.7(c)**). Thus, it can be concluded that the increased extent of crosslinking through thermal treatment can enhance the chain rigidity of PPN/PI.

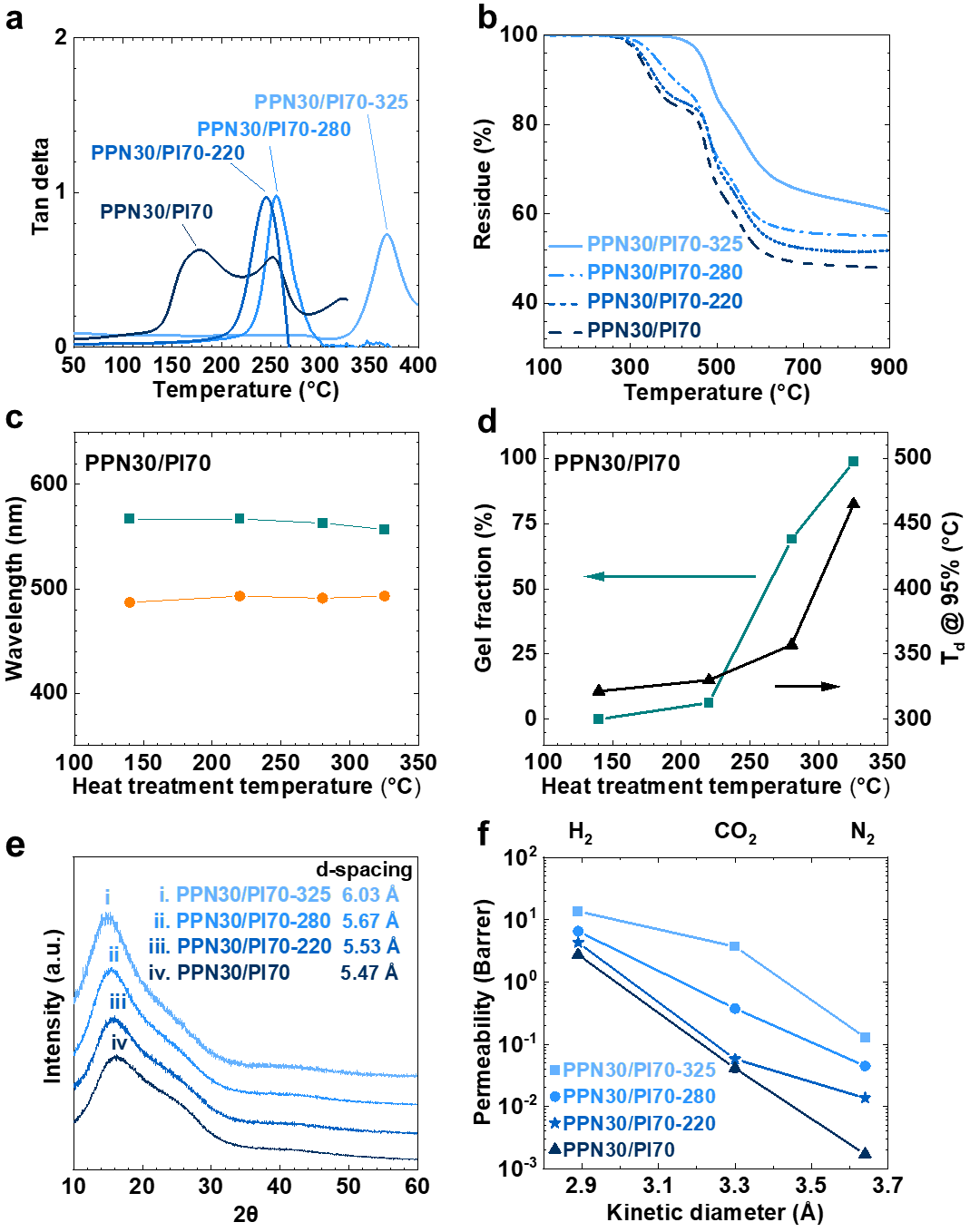

Figure 6.7 The effect of thermal treatment on characteristics of untreated and thermally treated PPN30/PI70 membranes. (a) Glass transition temperature, (b) thermal stability, (c) UV-Vis local maximum wavelength, (d) crosslinking degree correlated to thermal decomposition temperature (Td), and (e) XRD pattern. (f) Gas permeation performance with respect to gas kinetic diameter for untreated and thermally treated PPN30/PI70 membranes.

6.2.2.2 Structural parameters of PPN/PI and the thermally treated membranes

The interchain distance of the polymer is a key factor in the gas separation performance of the membrane. The d-spacing represents the average interchain distance between the backbone of polymeric materials. The XRD pattern of the semicrystalline polyimide showed a typical broad peak with a maximum intensity of 2θ = 15.5 degrees, indicating a d-spacing value of 5.7 Å (**Figure 6.3(b)**). In contrast to pure PI, the narrowed interchain distance of PPN/PI was attributed to the formation of intermolecular CTC, while the reduced peak intensity was due to the disruption of chain arrangement by PPN. Notably, a broad shoulder was observed in the spectra of PPN/PI around 2θ from 24.0 to 27.0 degrees (3.7 to 3.3 Å), indicating the increased extent of aromatic-aromatic stacking region. It was inferred that the densely packed regions of the PPN/PI blend result from intermolecular interactions. Besides, the PPN/PI blends showed higher I_3 values, analogous to the amount of free volume, than pure PI (**Table 6.1**). It was assumed that the PPN oligomer must be inserted between the backbones of PI, causing the increased amount of small free volume cavities. As the intermolecular CTC tightens the interchain distance of PPN/PI, more small free volume cavities are beneficial to form narrower and sharper free volume distribution than pure PI (**Figure 6.3(c)**). Based on the results above, it was concluded that incorporating PPN in PI can cause tightened interchain distance and narrow free volume distribution. The effect of the microstructure on the gas transport properties of the PPN/PI membranes will be discussed in ***Chapter 6.2.3.1***.

Table 6.2 Comparison of structural parameters obtained from PAL analysis of untreated and thermally treated membranes.

Membranes	τ_3 (ns)	I_3 (%)	R (Å)	FFV (%)
PI	2.35	8.4	3.16	2.00
PPN10/PI90	2.32	8.5	3.14	1.98
PPN30/PI70	2.34	9.1	3.15	2.14
PI-280	2.29	7.5	3.11	1.70
PPN10/PI90-280	2.24	7.7	3.06	1.66
PPN30/PI70-280	2.23	7.9	3.06	1.70

All the thermally treated membranes exhibited an increase in average interchain distance compared to their untreated counterparts (**Table 6.1**). This phenomenon might be attributed to the rearrangement of the polyimide chains caused by the thermal treatment, leading to a decrease in 2θ (increase in d-spacing values). Kertik *et al.* [209, 210] and Peydayesh *et al.* [211] independently reported an increasing trend in the interchain distance (decrease in 2θ) of Matrimid membranes with increasing thermal treatment temperature. Peydayesh *et al.* [211] implied that this phenomenon might be attributed to the induction of more crystalline segments in the polyimide after thermal annealing. In this study, this phenomenon is most likely attributed to the increased chain stiffness of PI (**Table 6.1**). It is worth noting that while thermal treatment often causes a decrease in the d-spacing values of a crosslinked polymer network, it can also enlarge the interchain distance. For instance, Qui *et al.* [212] reported an increased d-spacing after the crosslinking of 6FDA-DAM:DABA polyimide. Shi *et al.* [213] proposed that the crosslinking of PI-Im-COOH contributed to the increase in the d-spacing of the polyimide owing to the formation of rigid biphenyl linkages. The enhanced polymer

chain rigidity from crosslinking may contribute to the increase in the interchain distance [212, 213]. Interestingly, the thermally treated PPN/PI-280 membranes showed increased peak intensity compared to their untreated counterparts (**Figure 6.3(b)** and **Figure 6.3(e)**), indicating that the crosslinking of PPN can alter the polymer chain arrangement of PPN/PI blends. Furthermore, it was observed that the difference in the d-spacing value between thermally crosslinked PPN10/PI90-280 to PI-280 membranes (0.11 Å) was slightly smaller than that of the untreated PPN10/PI90 to PI membranes (0.17 Å) (**Table 6.1**). This result implies that the rigid and bulky linkages of crosslinked PPN networks might contribute to the enlargement of the average interchain distance. The PI composition could also be responsible for the increased d-spacing values. However, these effects could not completely counteract the influence of intermolecular CTCs on the polymer chain arrangement in the PPN/PI blends. Therefore, a higher composition of PPN resulted in a narrower average interchain distance in the PPN/PI-280 blends.

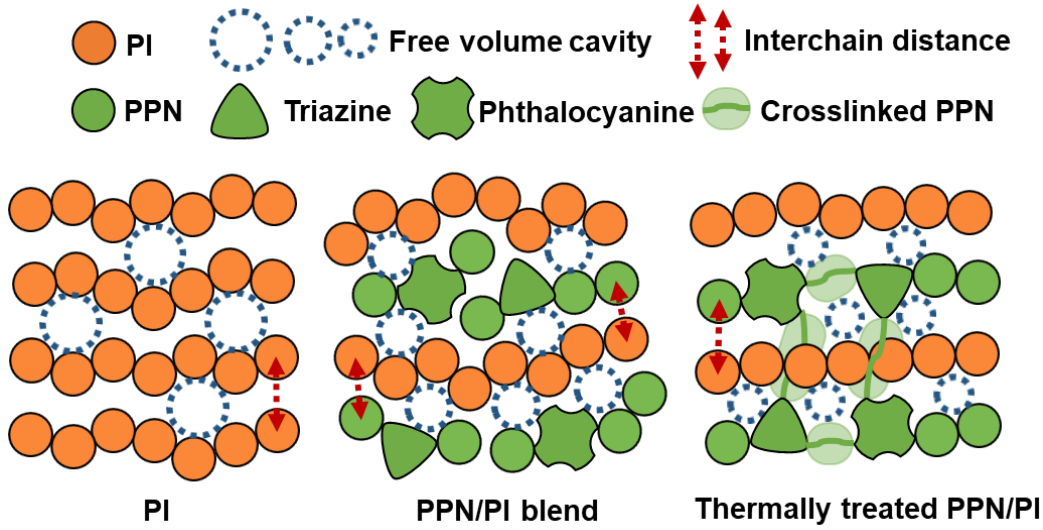

Figure 6.8 Schematic diagram of the effect of thermal treatment on PPN/PI matrix on the interchain spacing and free volume.

It is known that the FFV of glassy polymers decreases upon thermal treatment due to polymer chain relaxation and rearrangement toward its equilibrium state. As expected, a reduction in both the size and quantity of free volume cavities was observed in all the thermally treated membranes (**Table 6.2**). Interestingly, these membranes exhibited a narrower free volume distribution compared to their untreated counterparts (**Figure 6.9**). It was supposed that the thermal crosslinking of PPN can induce a higher fraction of smaller free volume cavities, whereas the larger cavities diminish due to the rigidification of the polymer matrix (**Figure 6.8**). The hypothesis was supported by the fact that the shrinkage of the free volume cavity radius of the PPN/PI-280s was more than that of PI-280 (**Table 6.2**). Meanwhile, the increasing trend of I_3 values is consistent with the composition of PPN under the same thermal treatment condition. Indeed, the higher amount of PPN caused the narrower free volume size distribution of the thermally treated membranes (**Figure 6.3(f)**). Based on the results above, it was concluded that the free volume size distribution of PPN/PI membranes can be narrowed by thermal crosslinking of PPN. However, it should be noted that thermal treatment may not always have the same impact on the FFV and d-spacing values of the membranes. Recently, Dose *et al.* [75] demonstrated that thermally crosslinkable polyimide (6FDA-DAPI/DABA) exhibited an increase in d-spacing but showed no significant change in the quantity of FFV upon thermal treatment. They proposed that despite the slightly enlarged average interchain distances, the thermal treatment narrowed free volume distribution in the polyimide membranes [75]. In the case of PI (Matrimid) membranes, as discussed earlier, moderate thermal treatment can lead to an increase in the d-spacing values. However, it is important to note that the relationship between FFV and d-spacing values of PI-based membranes under thermal treatment remains unclear and requires further investigation.

Understanding the microstructure of polymeric membranes will be crucial for the design of high-performance gas separation membranes.

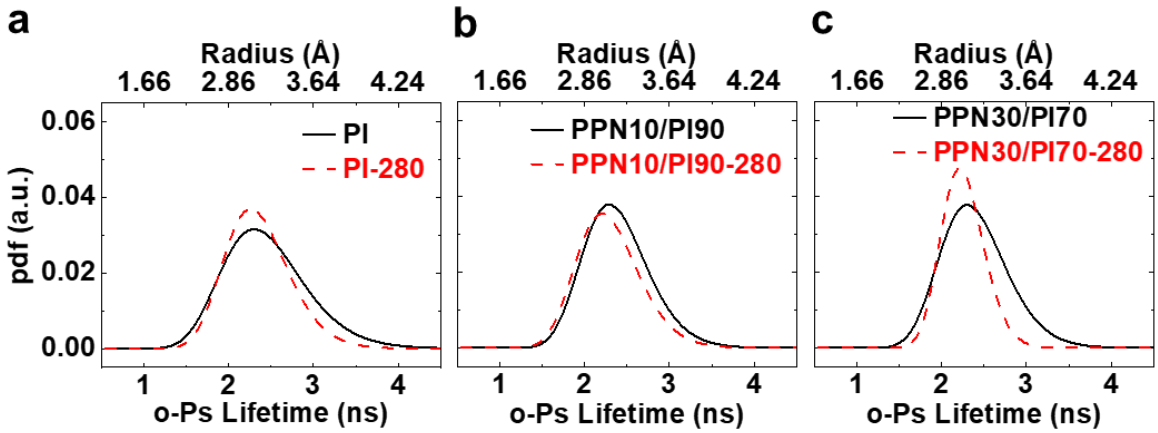

Figure 6.9 The comparison of o-Ps lifetime distributions for thermally treated and untreated membranes. (a) PI and PI-280; (b) PPN10/PPI90 and PPN10/PI90-280; (c) PPN30/PI70 and PPN30/PI70-280.

6.2.3 Hydrogen separation analysis

6.2.3.1 Effect of PPN composition on hydrogen separation properties

In general, gas permeability coefficients of PI and PPN/PI membranes are in agreement with the order of gas kinetic diameters, indicating the size-sieving effect dominated gas transport behavior through membranes (**Figure 6.10(a)**). It was found that the PPN/PI blend or the thermally treated thin-films with an PPN loading of more than 50 wt% were too brittle to undergo testing. With respect to the PPN composition of the membranes, all gas permeabilities decreased with the trend of d-spacing values, which were affected by polymer chain mobility. Meanwhile, intermolecular interactions like CTC contributed to narrowed free volume cavity size and distribution of PPN/PI (**Figure 6.3(c)**), resulting in

the increasing trend of H_2 /CO_2 and H_2/N_2 permselectivity with the increased PPN composition (**Figure 6.10(d)**). Notably, the extent of increase in the permselectivity of the H_2/CO_2 pair with a smaller difference in kinetic diameter (0.41 Å) was greater than that of the H_2/N_2 pair with a larger difference (0.75 Å). This result implies that the contribution of solubility selectivity has a superior influence over that of diffusivity selectivity in adjusting the H_2 separation performance of the PI matrix via incorporating the PPN.

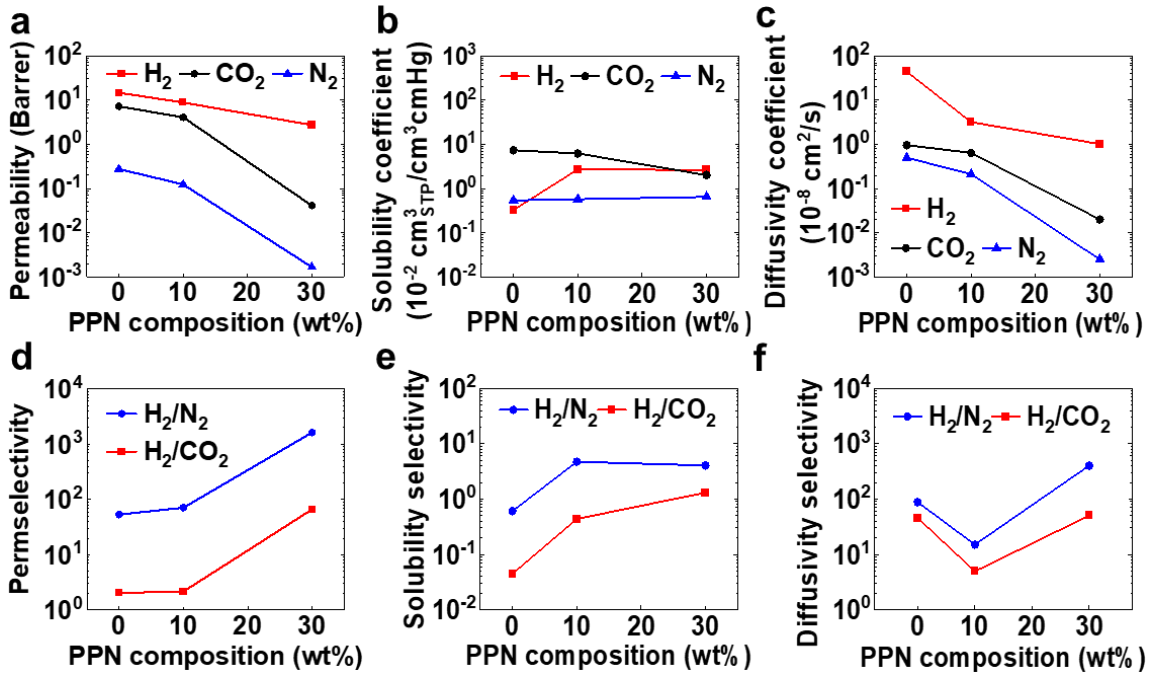

Figure 6.10 Pure gas permeation analysis of PI and PPN/PI blend membranes. (a) Permeability, (b) solubility, (c) diffusivity of H_2, CO_2, and N_2. (d) permselectivity, (e) solubility selectivity, and (f) diffusivity selectivity of H_2/N_2 and H_2/CO_2.

For polymeric membranes, the permeability coefficient can be described as the product of the solubility and diffusivity coefficients, according to the solution-diffusion model [157]. The solubility coefficient was measured by the sorption of each gas species in

equilibrium at the same absolute pressure and temperature condition. The diffusivity coefficient was calculated from D = P/S. On the one hand, polyimides have high solubility to the quadrupolar CO_2 due to the abundant polar carbonyl groups in imide moiety [71]. As expected, the pristine PI showed a higher solubility coefficient of CO_2 than H_2 and N_2. Interestingly, the blending of 10 and 30 wt% PPN in PI caused a gradual decrease in CO_2 solubility of 15% and 73%, respectively, compared to the pristine PI (**Figure 6.10(b)**), despite the introduction of CO_2-philic functional groups in the PPN [38]. The suppression of the CO_2 solubility coefficient can be attributed to the induced electron donor-acceptor complexes, reducing CO_2 affinity to the polymers [214-216]. For nonpolar gases such as H_2 and N_2, the increasing gas solubility coefficient trend agrees with the I_3 values. To our surprise, the incorporation of PPN significantly increases H_2 solubility coefficient of PPN/PI, which is about 8.2 times higher than the pristine PI. Therefore, the PPN30/PI70 showed H_2/N_2 and H_2/CO_2 solubility selectivity about 6.6 and 28.9 times, respectively, higher than the pristine PI (**Figure 6.10(e)**). A possible reason for the higher H_2 solubility of PPN/PI was attributed to the narrower and sharper free volume distribution with the slightly smaller free volume cavity size. Another plausible explanation is that the unique PPN/PI intermolecular CTC contributes to the improvement in H_2 solubility. On the other hand, the pristine PI possesses higher diffusivity coefficients due to its larger interchain distance and free volume than the PPN/PIs (**Figure 6.10(c)**). In contrast, the incorporation of 10 wt% PPN in PI led to decreased H_2 diffusivity coefficient and diffusivity selectivity (**Figure 6.10(f)**). It can be explained that the increasing H_2 sorption of the PPN/PI blends prolonged the H_2 diffusion through the membranes. Another reason might be the phase arrangement affecting the gas diffusion pathway. However, adding 30 wt% of PPN in PI led to higher H_2/N_2 and

H_2/CO_2 diffusivity selectivity than the pristine polyimide. This effect was attributed to the more intermolecular interactions generating a more tightly packed chain arrangement region, which is favorable for the diffusion of hydrogen rather than other larger gases (**Figure 6.10(b)**). Based on the results above, It was concluded that the improvement in both H_2/CO_2 and H_2/N_2 permselectivity of PPN/PI is due to the enhancement in both solubility selectivity and diffusivity selectivity.

6.2.3.2 Hydrogen separation properties of the thermally treated PPN/PI membranes

The measured solubility coefficients of neat PI (Matrimid) and PI-280 membranes are in good agreement with previous literature (**Table 6.3**). Previous literature reported the H_2 solubility of Matrimid membranes falling within the range of 0.16 to 0.21 ($10^{-2}cm^3/cm^3cmHg$). Interestingly, the H_2 solubility coefficients of thermally treated PI-280 remained nearly unchanged in comparison to that of the untreated PI, while the increase in CO_2 and N_2 solubility coefficients was observed. Similarly, the PPN/PI-280 membranes subjected to the same thermal treatment showed nearly unchanged H_2 solubility but increased CO_2 and N_2 solubility coefficients. It was postulated that the increased CO_2 and N_2 solubility in the PI-280 and PPN/PI-280 membranes may be attributed to the thermally induced rearrangement of polymer microstructure, which will be discussed later. However, the thermal treatment protocols in this study appeared to have a negligible impact on the H_2 solubility of both PI and PPN/PI membranes (**Table 6.4**). Moreover, the H_2 solubility of PPN/PI-280 is approximately eight times higher than both PI-280 and PPN-280. These results indicate that the increase in the H_2 solubility of PPN/PI-280 membranes was mainly a result of interactions between PI and PPN rather

than the intrinsic H_2 affinity of the neat components. Therefore, It was concluded that incorporating PPN in the PI matrix helps increase the H_2 solubility of PPN/PI-280 membranes, inheriting the advantage of the untreated PPN/PI membranes.

Table 6.3 H_2, CO_2, and N_2 solubility coefficients of PI (Matrimid), PI-280 and PPN-280 membranes measured in this work compared with data from previous literature.

Membrane components	Solubility†			Solubility selectivity			Note	Ref.
	H_2	CO_2	N_2	H_2/CO_2	H_2/N_2	CO_2/N_2		
Matrimid	0.16	7.8	0.68	0.021	0.24	11.5	time lag	[1]
Matrimid	0.20	24.8	0.78	0.0081	0.26	31.8	time lag	[2]
Matrimid	0.21	31.0	1.1	0.0068	0.19	28.2	direct sorption	[3]
PI	0.33	7.4	0.55	0.045	0.61	13.6	direct sorption	this work
PI-280	0.31	25.2	2.2	0.012	0.14	11.5	direct sorption	this work
PPN-280	0.32	1.14	0.17	0.28	1.9	6.7	direct sorption	this work

† Solubility unit: $1 \cdot 10^{-2} \cdot cm^3(STP)/cm^3 \cdot cmHg$

Table 6.4 Comparison of gas transport coefficients of PPN/PI and PPN/PI-280 membranes in pure gas permeation analysis

Membranes	Permeability (Barrer)			Solubility†			Diffusivity‡		
	H_2	CO_2	N_2	H_2	CO_2	N_2	H_2	CO_2	N_2
PI	14.7	7.2	0.28	0.33	7.4	0.55	44.3	1.0	0.50
PI-280	17.6	10.8	0.34	0.31	25.2	2.2	57.4	0.43	0.15
PPN10/PI90	8.8	4.1	0.12	2.8	6.3	0.58	3.2	0.6	0.21
PPN10/PI90-280	7.8	1.8	0.11	2.7	16.8	2.1	2.8	0.11	0.054
PPN30/PI70	2.7	0.041	0.0017	2.7	2.0	0.66	1.0	0.020	0.0025
PPN30/PI70-280	6.5	0.37	0.045	2.8	12.2	2.0	2.3	0.031	0.022
PPN-280	--[a]	--[a]	--[a]	0.32	1.14	0.17	--[b]	--[b]	--[b]

Note:

† Solubility unit: $1 \cdot 10^{-2} \cdot cm^3(STP)/cm^3 \cdot cmHg$

‡ Diffusivity unit: $1 \cdot 10^{-8}$ cm^2/s

[a] The gas permeability was not measured for the thin-film due to brittleness.

[b] The diffusivity of the thin-film is not available.

Comparing thermally treated membranes to their untreated counterparts, the changes in H_2 permeability coefficients of PI-280 and PPN/PI-280 membranes appeared to be dependent on their H_2 diffusivity coefficients, as their H_2 solubility coefficients were consistent (**Table 6.4**). However, all thermally treated membranes showed significantly increased CO_2 and N_2 solubility coefficients, leading to a decrease in H_2/CO_2 and H_2/N_2 solubility selectivity (**Table 6.5**). This effect coincides with the shrinkage of free volume cavity size, which facilitates gas sorption (**Table 6.2** and **Figure 6.9**). On the other hand, the diffusivity and diffusivity selectivity of the thermally treated membranes showed inconsistent changes with respect to the PPN composition. As discussed in ***Chapter 6.2.2***, thermal treatment reduced the chain rigidity while increasing the interchain distance of

both PI-280 and PPN/PI-280 blends (**Table 6.1** and **Table 6.2**). These results imply that the competition between the effects of polymer chain flexibility and interchain distance affects gas diffusivity and diffusivity selectivity (**Table 6.4** and **Table 6.5)**. Given the complicated nature of thermally treated membranes, the actual reasons require further investigation. It is possible that the decrease in polymer chain mobility could hinder the diffusion of gas molecules through free volume cavities, while the increase in d-spacing may benefit gas transport. However, it is worth noting that the H_2 solubility coefficients of the thermally treated membranes remain consistent with the untreated counterparts (**Table 6.4**). The improved H_2 solubility of the PPN/PI blends was primarily attributed to the incorporation of PPN and is likely independent of the thermal treatment, even if crosslinking of PPN occurs in the semi-IPN membranes. Comparing the solubility coefficients of all membranes, the free volume with a larger number, smaller size, and narrower size distribution in the membrane is in good agreement with the increased solubility of the small gas molecule (hydrogen). This is the main reason for the significant improvement of the hydrogen permselectivity of the PPN/PI membranes.

Table 6.5 Comparison of permselectivity, solubility selectivity, and diffusivity selectivity of PPN/PI and PPN/PI-280 membranes in pure gas permeation analysis

Membranes	Permselectivity (α)			Solubility selectivity			Diffusivity selectivity		
	H_2/CO_2	H_2/N_2	CO_2/N_2	H_2/CO_2	H_2/N_2	CO_2/N_2	H_2/CO_2	H_2/N_2	CO_2/N_2
PI	2.0	53.3	26.1	0.045	0.61	13.6	45.7	87.9	1.9
PI-280	1.6	52.2	31.8	0.012	0.14	11.2	134	381	2.8
PPN10/PI90	2.2	71.2	32.8	0.44	4.7	10.8	5.0	15.0	3.0
PPN10/PI90-280	4.3	67.4	15.6	0.16	1.3	7.9	26.5	52.0	2.0
PPN30/PI70	66.4	1637	24.7	1.3	4.0	3.1	50.6	404	8.0
PPN30/PI70-280	17.4	146	8.4	0.23	1.4	6.1	76.4	106	1.4
PPN-280	--[a]	--[a]	--[a]	0.28	1.9	6.7	--[b]	--[b]	--[b]

Note:

[a] The ideal gas selectivity is not available.

[b] The diffusivity selectivity of the thin-film is not available.

Comparing the gas separation performance of the thermally treated PPN30/PI70 membranes at temperatures ranging from 220 to 325 ℃, it was revealed that the gas permeability coefficients improved with increasing thermal treatment temperatures (**Figure 6.11(a)**). This increasing trend in permeability coincided with the d-spacing values of the thermally treated PPN30/PI70 membranes (**Figure 6.7(e)**). As discussed above in ***Chapter 6.2.2.2***, the enlargement of average interchain distances was attributed to the combined effects of thermal rearrangement of the PI polymer chain and crosslinking of PPN (**Figure 6.7(e)**). Such a phenomenon is responsible for the increase

in the H_2 permeability but the decrease in the H_2 permselectivity. Although the change in thermal treatment temperature will affect the gas permeation properties, the hydrogen separation behavior of all thermally treated PPN30/PI70 membranes exhibited a similar sieving mechanism (**Figure 6.7(f)**). The H_2/N_2 permselectivity gradually decreased with the increase in treatment temperature. However, the H_2/CO_2 permselectivity of PPN30/PI70-220 was higher than the untreated PPN30/PI70 membrane (**Figure 6.11(b)**). It is attributed to the competing factors of the enlargement of interchain distance and the shrinkage of free volume cavity size and distribution. These results demonstrate the potential of tuning the microstructure of crosslinkable PPN/PI blends to enhance the hydrogen separation performance.

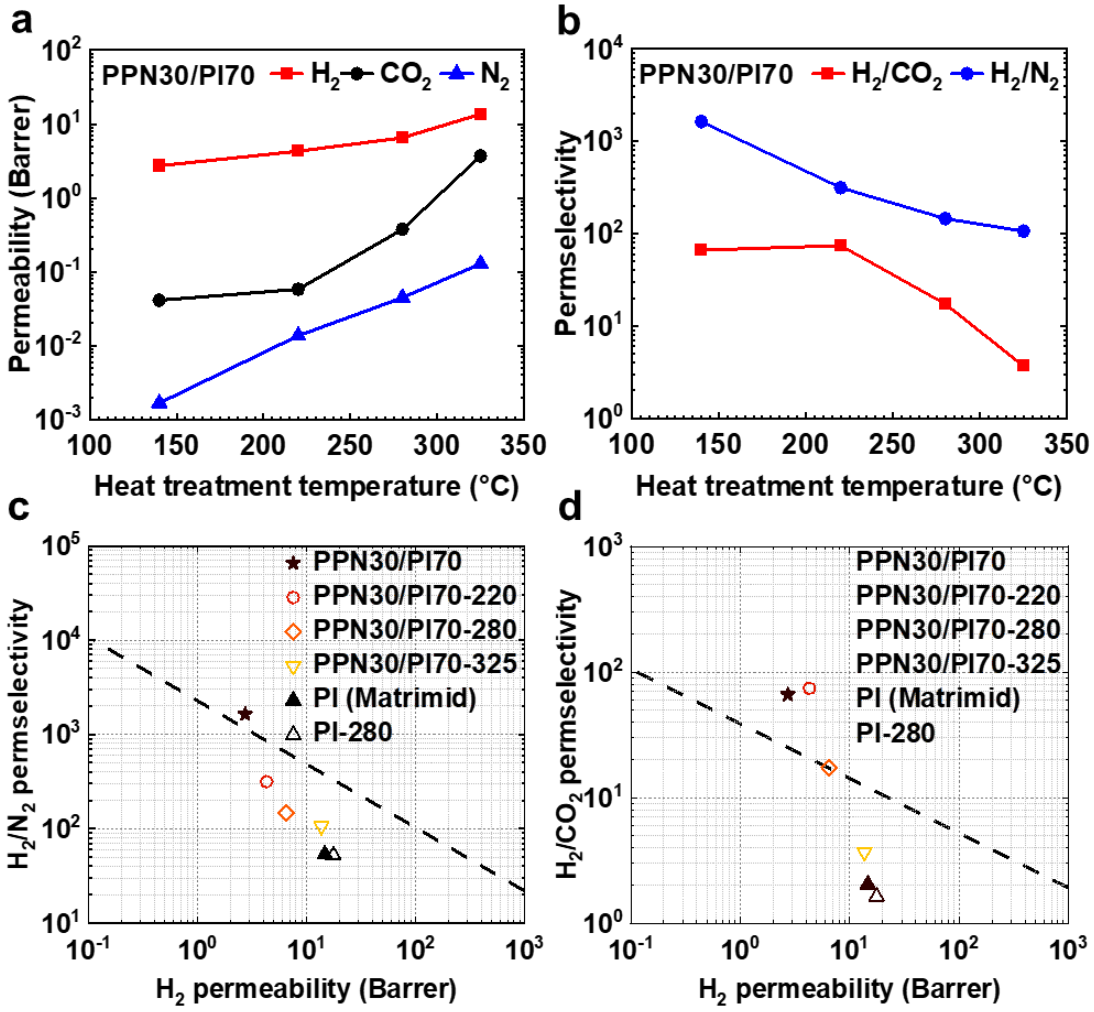

Figure 6.11 Gas separation performance of thermally treated PPN30/PI70 membranes (a) Permeability and (b) permselectivity obtained from pure gas permeation analysis with respect to thermal treatment temperature, and the comparison of (c) H_2/N_2 and (d) H_2/CO_2 separation performance to Robeson upper bound (2008).

The gas permeation performance of the untreated and thermally treated PPN30/PI70 membranes was compared to Robeson upper bound plots (**Figure 6.11(c-e)** and **Table S2**). The incorporation of 30 wt% PPN significantly increased the H_2/N_2 and H_2/CO_2 permselectivity of the PPN30/PI70 membrane, which was about 33.2 times higher than that of the neat PI membrane, while maintaining a comparable H_2 permeability of 2.7

Barrer. Therefore, the H_2 separation performance of the PPN30/PI70 membrane exceeds the H_2/N_2 and H_2/CO_2 trade-off lines. With thermal treatment, the PPN30/PI70-220 membrane exhibited an optimal H_2/CO_2 permselectivity of 74.3 and H_2 permeability of 4.3 Barrer, which were approximately 12% and 59% higher, respectively, than the untreated PPN30/PI70 membranes. This study has demonstrated the feasibility of blending PPN in the polyimide (PI) matrix and employing thermal treatment to adjust the microstructure of the PPN/PI blend membranes for H_2 purification.

6.2.3.3 H_2/CO_2 mixed-gas separation analysis on effects of CO_2 plasticization and competitive sorption

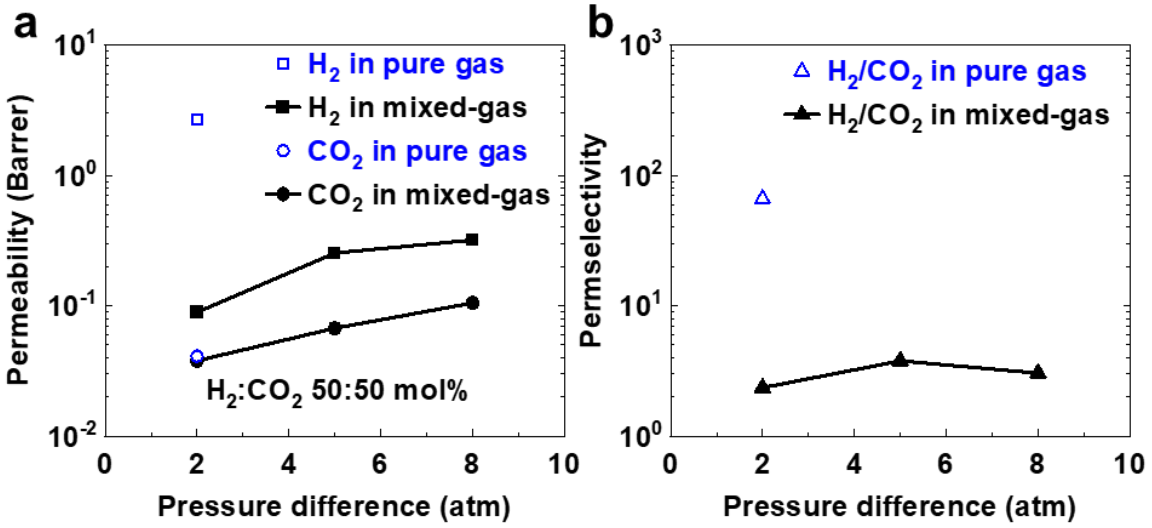

Figure 6.12 Mixed-gas (H_2:CO_2 50:50 mol%) separation performance of PPN30/PI70 membrane with respect to pressure difference. (a) Permeability, and (b) permselectivity.

For glassy polymer membranes, plasticization may take place when the mixed-gas contains condensable gas, such as CO_2, and the plasticization pressure is usually defined

as the pressure with the minimum CO_2 permeability within the applied pressure difference [72, 217, 218]. H_2/CO_2 (50:50 mol%) mixed-gas permeation analysis (**Figure 6.12** and **Table S3**) revealed an increasing trend in both H_2 and CO_2 permeability in H_2/CO_2 mixed-gas within the range of pressure difference. Interestingly, the plasticization pressure within the pressure difference was not observed in the PPN30/PI70 membrane. Since the CO_2 solubility coefficient of the PPN30/PI70 membrane is largely suppressed, the contribution of CO_2 sorption to the CO_2 permeability in H_2/CO_2 mixed-gas might be small at the initial pressure. The increase in H_2 and CO_2 permeability in H_2/CO_2 mixed-gas may be due to the increased contribution of gas diffusion, resulting from the disrupted polymer chain packing by condensable CO_2 molecules [218]. In comparison to the permeability in pure gas, nonetheless, the plasticization effect alone could not fully explain the maintained CO_2 permeability coupled with decreased H_2 permeability in H_2/CO_2 mixed-gas. Considering the quadrupolar properties of CO_2 molecules exhibiting a strong affinity for adsorption in polymers [72], a plausible explanation for this phenomenon is that the CO_2 molecules have stronger interactions with polymer chains within the free volume cavities of PPN30/PI70 than H_2 molecules [72, 195]. It was inferred that the effect of CO_2 competitive sorption in H_2/CO_2 mixed-gas suppresses the inherently high H_2 solubility and solubility selectivity of the PPN30/PI70 membrane. In other words, though the H_2 solubility coefficient of the PPN30/PI70 membrane is higher (1.3 times) than CO_2 solubility, the transport of H_2 molecules through the narrowed free volume cavities might be limited by CO_2 molecules possessing strong interactions with the polymer chain. Future work shall focus on reducing the CO_2 affinity to polymer membranes to alleviate the competitive sorption effect in H_2/CO_2 separation. This study not only advances the

understanding of free volume characteristics and hydrogen transport properties of the PPN/PI blend membranes, but also highlights a facile material strategy for designing charge-transfer polymer blends with tunable microstructure.

6.3 Conclusion

This work demonstrates a novel concept to adjust the characteristics of free volume and hydrogen separation performance of polyimide membranes. It was concluded that the blending of the polyimide (PI) and the resorcinol-based phthalonitrile prepolymer (PPN) with electron donor/acceptor moieties could enable the formation of the intermolecular charge-transfer complex (CTC), resulting in narrowed free volume cavity size and distribution. The adjustment in free volume microstructure has considerably improved the H_2 solubility coefficient of PPN/PI blend membranes about an order of magnitude higher than that of pure PI membrane. The N_2 and CO_2 solubility coefficients were either maintained or suppressed, leading to the desirable H_2/N_2 and H_2/CO_2 solubility selectivity of PPN/PI membranes. Consequently, the PPN30/PI70 membrane showed ideal H_2/CO_2 and H_2/N_2 permselectivity of 66.4 and 1637, respectively, with H_2 permeability of 2.7 Barrer, surpassing the 2008 Robeson upper bounds. Upon thermal treatment, the PPN30/PI70 membrane showed increased gas permeability with the elevated thermal treatment temperature. Remarkably, the PPN30/PI70-220 membrane possessed an ideal H_2/CO_2 permselectivity of 74.3 and H_2 permeability of 4.3 Barrer, 12% and 59% higher than the untreated counterpart. This result was attributed to the balance of enlargement in the interchain distance and the shrinkage in free volume cavity size and distribution.

Further studies using H_2/CO_2 mixed-gas (50:50 mol%) for permeation analysis under pressure difference within the range of 2 to 8 atm confirmed the existence of the CO_2 plasticization effect. The competitive sorption effect of CO_2 molecules was found to suppress the inherently high H_2 solubility and solubility selectivity, compromising the separation performance of the PPN30/PI70 membrane in H_2/CO_2 mixed-gas. This study demonstrated the potential of using the charge-transfer PPN/PI blend with tunable microstructure to design high-performance hydrogen purification membranes.

Chapter 7

Conclusions and Recommendations

The research outcomes in this thesis demonstrate a novel polymeric phthalonitrile-based material for membrane applications and a new material strategy to adjust the microstructure characteristics and gas permeation behavior of membranes. This chapter is to 1) briefly summarize the research works constructed by this thesis, 2) evaluate the degree of validation achieved for the presented hypothesis, and 3) discuss the novelty and research impact of the corresponding studies. Finally, future works are recommended for further in-depth investigation in this research field.

7.1 Summary

Three main objectives were proposed and sequentially accomplished, leading to the completion of this thesis, which investigated the microstructure and gas permeation behavior of PPN and its derived carbon materials.

1) To understand the relationship between microstructure characteristics and gas permeation behavior of PPN and PPN-derived microporous carbon materials in the context of membranes.

   Despite its relevance for material development in many potential industrial applications, no published literature was available on this topic. This study pioneered the investigation of the microstructure characteristics of the PPN network and its influence on the gas permeation behavior of the PPN-derived polymeric and carbon membranes via metal-ion doping and curing treatment methods. The study demonstrated the feasibility of PPN as an advanced membrane material and identified the potential of PPN-derived carbon membranes for gas separation.

2) To provide in-depth insights into the microstructure evolution of the PPN-derived carbon from its polymeric precursor.

   Previous studies mostly ignored the influence of the microstructure arrangement of PPN precursor on the derived carbon materials, though many reports demonstrated impactful structural designs on PPN-derived carbon materials. Furthermore, due to

physical limitations, the conventional gas sorption characterization technique for porosity was not applicable to studies on microporosity less than 0.4 nm. While gas permeation analysis has a limitation in examining materials such as the membrane configuration, it can identify subtle changes in the microstructure of polymeric and carbon materials. The understanding from this study can facilitate the development of PPN-derived polymeric and carbon materials, which may not be limited to the context of membranes.

3) To explore PPN as an advanced membrane material for adjusting the microstructure characteristics of membranes fabricated from commercially available polyimide resin.

The adjustment of microstructure characteristics of commercially available polyimide is an important research topic due to its dominant role in the current and emerging gas separation industry. By utilizing the intrinsic electron donor/acceptor properties of PPN, a novel material strategy to adjust microstructure characteristics and gas transport properties of polyimide was developed. It was demonstrated that the phthalonitrile prepolymer can adjust microstructure characteristics, including free volume, to improve gas solubility (i.e., H_2) and selectivity (i.e., H_2/CO_2 and H_2/N_2) of PPN/PI blend membranes.

7.2 Discussion on hypothesis

This thesis aimed to develop PPN resin as an advanced membrane material. The key hypothesis of this thesis is that the adjustment of microstructure characteristics of PPN resins can alter that of the PPN-derived polymeric and carbonaceous materials and, therefore, adjust the gas permeation behavior of PPN-based polymeric and carbonaceous membranes. The results in ***Chapter 4*** have experimentally supported the hypothesis. The doping of metal ions was able to adjust the molecular arrangement of the PPN networks, thereby adjusting the gas permeation behavior of the PPN-based membranes. Furthermore, it was identified that the microporous carbon derived from the PPN network largely depended on the molecular arrangement of the precursor, although the specific microstructure evolution mechanism of PPN-derived microporous carbon requires further detailed studies.

With the aim of obtaining insights into the developed PPN membrane materials, ***Chapter 5*** investigated the relationship between microstructure characteristics and gas permeation behavior of nea PPN and its derived carbon molecular sieve membranes. It was identified that the ideal gas separation performance of PPN-derived carbon molecular sieve membranes is comparable to the state-of-the-art membranes due to the successful adjustment of microstructure arrangements of the precursor. Furthermore, the key hypothesis was further proved true from the significant improvement of gas separation performance of PPN and the derived microporous carbon membranes subjected to various thermal histories that subtly altered the microstructure arrangements of the PPN network.

The work was extended to the adjustment of commercially available polyimide in ***Chapter 6*** to demonstrate the potential of phthalonitrile resin as an advanced membrane material. It was hypothesized that the electron donor/acceptor properties of the PPN network can alter the microstructure characteristics and the gas permeation behavior of polyimide membranes. The hypothesis was supported by the results because incorporating PPN in polyimide significantly improves the gas (hydrogen) solubility, which is higher than that of both neat PPN and PI materials.

The key hypotheses supported by the results in this work enabled vital insights regarding the microstructure characteristics and gas permeation behavior of PPN-based polymeric and carbon materials. This understanding achieved in this thesis serves as a fundamental basis for developing next-generation PPN-based polymeric and carbon membrane materials.

7.3 Novelty and research impact

The novelty and significance of this thesis drawn from this thesis were listed as follows:

1) Explore the adjustability of microstructure characteristics and gas permeation behavior of PPN and the derived carbon materials.

   The molecular arrangement of PPN can be feasibly adjusted via metal-ion doping or heat treatment. It was demonstrated that Co^{2+} or Cu^{2+}-doped PPN precursor with promoted stacking of molecular chain creates the PPN-derived microporous carbon

materials with graphitic-like stacking microstructure, while the neat PPN precursor generates mainly amorphous carbon at pyrolysis temperature of 550 ℃. The adjustment of the microstructure arrangement of the stacking region in the PPN network could adjust the gas permeation behavior of PPN and the derived microporous carbon membranes. It was further identified that carbon molecular sieve membranes derived from neat PPN precursors have superior gas permeance than ones derived from metal-ion-doped precursors.

2) Demonstrate PPN and the derived carbon materials as promising candidates for gas separation membranes.

Though PPN membranes possess moderate gas permeability and selectivity among heterocyclic polymer materials, the derived carbon molecular sieve membranes showed outstanding ideal gas separation performance beyond the state-of-the-art Robeson upper bounds. Furthermore, the gas separation performance of PPN-CMS membranes is comparable to many CMS membranes derived from highly engineered heterocyclic polymeric materials. Besides, it was demonstrated that incorporating PPN with commercially available polyimide can obtain new types of membrane materials with unique gas transport properties. This study identified the potential of PPN as a promising material for gas separation polymeric and carbon membranes.

3) Propose and test a mechanism for the microstructure evolution of PPN to the derived microporous carbon materials at the angstrom level.

It was identified that microporosity, especially ultramicropores, existed in the PPN-derived carbon materials at various pyrolysis temperatures. The aromatic stacking of the PPN network is a key factor in the ultramicropore distribution of the derived carbon materials. The promoted stacking of PPN can generate small-sized, narrow-distributed ultramicropores of the carbon molecular sieve membranes. The new insights on the microstructure evolution of PPN precursor to the derived microporous carbon materials pave the way for further development of PPN-based materials for various applications.

4) Establish the relationship between microstructure characteristics and gas permeation behavior of PPN and the derived microporous carbon membranes.

Understanding the relationship between microstructure characteristics and the gas separation performance of PPN and the derived carbon enables the development of PPN-based high-performance membrane materials. It was demonstrated that the molecular chain arrangement played a key role in determining the gas separation performance of the derived carbon molecular sieve membranes. The increased intermolecular distance and the promoted stacking of the molecular chain of PPN precursor can improve and increase the intermolecular distance and narrow the ultramicropore distribution of the derived carbon materials. These adjustments in microstructure characteristics of the PPN network resulted in the improvement of the

gas separation performance of PPN-derived carbon molecular sieve membranes pyrolyzed at 750 ℃ to surpass the permeability-selectivity trade-off relationship of gas separation membranes.

5) Identify the impact of incorporating PPN in commercially available polyimide on the microstructure characteristics and gas transport properties of the blend membranes.

The incorporation of PPN in PI was able to adjust free volume characteristics of the blend membranes via the formation of a charge-transfer complex. Furthermore, the H_2 solubility and solubility selectivity of the blend membranes were largely improved due to the narrowed free volume distribution of the blend membranes. The thermal crosslinking of PPN in the PI matrix could increase the intermolecular distance of the blend and further adjust the gas separation performance of the semi-IPN membranes.

7.4 Recommendation for future work

This thesis was purposefully scoped to study resorcinol-based polyphthalonitriles as polymeric and carbon membrane materials on their microstructure characteristics and gas permeation behavior. The PPN-based membrane fabrication study was also limited to the solvent evaporation method. While the new insights and understandings provided more solid research bases in this field, more work can be targeted to extend these findings on different types of phthalonitrile monomer (precursor). Future works will be able to pursue scientific curiosity and the fundamental understanding of nature in fabricating high-quality polymeric and carbonaceous membrane materials for various applications. The

following paragraphs present the recommendations for future scientific investigations with brief justification.

7.4.1 Solvent-free fabrication of PPN-based membranes

Phthalonitrile monomers can be melted by simple thermal processes and fabricated into various configurations of PPN materials, including encapsulants, foams, and coatings. Various phthalonitrile monomers have been developed to provide a wide range of melting process windows without the need for solvents. This unique property gives the heterocyclic polymer resins great opportunities to develop sustainable membrane fabrication processes. In this case, the in-depth understanding of the relationship between molecular structure and transport properties of PPN materials is the key to developing high-performance PPN-based membranes, including polymeric, carbon, and mixed-matrix membranes with functional nanofillers.

7.4.2 PPN-based catalytic hierarchical carbon materials

The high char yield of PPN represents the high productivity of fabricating carbon materials. This work demonstrates the metal-ion-doped PPN-derived carbon materials with adjustable microstructure characteristics on a sub-nanometer scale. Future work may focus on taking advantage of activation, bubble foaming, or other techniques to introduce more extrinsic porosity for developing high-performance PPN-derived porous carbon materials for various applications.

7.4.3 PPN-based gas barrier

The high thermal stability of PPN resins made the materials a promising candidate for many needs of encapsulation, sealing, or barrier applications. This work demonstrated that blending PPN can improve the gas barrier efficiency of commercially available polyimide in terms of suppressed gas permeability. It also revealed that the thermal history of PPN largely determines its microstructure characteristics and gas permeation behavior. This understanding may enable the development of PPN-based gas barriers for carbon dioxide, oxygen, or hydrogen.

Appendix

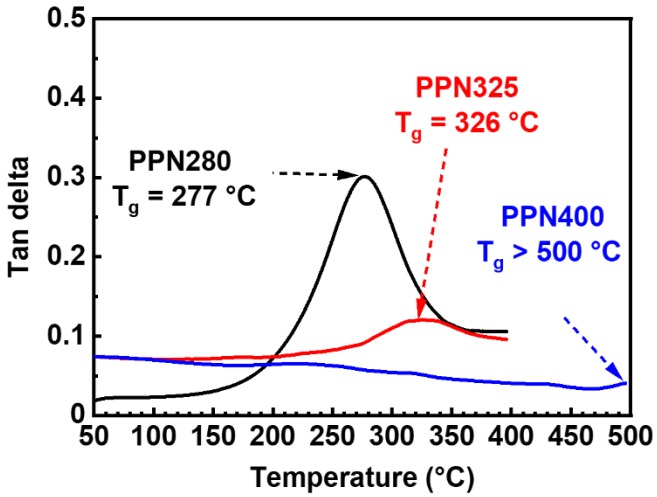

Figure S1 Glass transition temperature of PPN with respect to curing temperature.

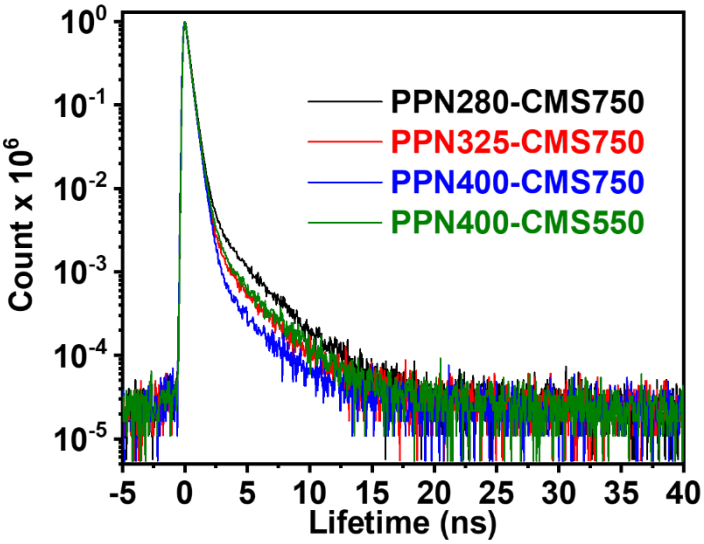

Figure S2 PAL spectrum of PPN-CMS membranes.

Table S1 Pure gas permeabilities and ideal selectivities of supported PPN and PPN-CMS membranes compared to published literature.

Precursor	Membrane	Pyrolysis Temp.; Inert condition	Permeability			Selectivity		Ref
			CO_2	O_2	N_2	CO_2/N_2	O_2/N_2	
PI	Matrimid	--[*]	10.8	2.5	0.4	28.3	6.5	[49]
	MAT-650-Ar	650 ℃; Argon	1592	383	56.9	28.0	6.7	[49]
	Matrimid-CMS700	700 ℃; Argon	390	94	10	39	9.4	[100]
	ODPA-FDA	--[*]	21.4	4.2	0.7	29.7	5.9	[49]
	ODPA-550-Ar	550 ℃; Argon	9011	2006	529	17.7	3.5	[49]
	ODPA-650-Ar	650 ℃; Argon	5379	1354	194	27.7	7.0	[49]
	ODPA-650-Vac	650 ℃; Vacuum	1086	131	7.56	143.6	17.4	[49]
	ODPA-750-Ar	750 ℃; Argon	2423	432	48.4	61.3	9.6	[49]
	6FDA-DAM/DABA(3:2)	--[*]	94.8	--	4.9	19.4	--	[143]
	6FDA-DAM/DABA(3:2)-CMS450	450 ℃; Argon	385.4	--	25.1	15.4	--	[143]

Precursor	Membrane	Pyrolysis Temp.; Inert condition	Permeability			Selectivity		Ref
			CO_2	O_2	N_2	CO_2/N_2	O_2/N_2	
	6FDA-DAM/ DABA(3:2)-CMS600	600 ℃; Argon	2840.0	--	156.1	18.2	--	[143]
	PABZ-6FDA-PI	--*	18.0	3.6	0.67	27	5.4	[144]
	PABZ-6FDA-PI-CMS550	550 ℃; Argon	5915	1410	171	35	8.3	[144]
	PABZ-6FDA-PI-CMS750	750 ℃; Argon	200	46	4.2	47	10.8	[144]
	PABZ-6FDA-PI-CMS800	800 ℃; Argon	57	14	1.1	53	12.5	[144]
	$6FDA_2$:$sBPDA_{0.5}$:$aBPDA_{0.5}$/ $DAM_{1.8}$:$DABA_{1.2}$	--*	98.0	22.5	4.6	21.3	4.9	[145]
	$6FDA_2$:$sBPDA_{0.5}$:$aBPDA_{0.5}$/ $DAM_{1.8}$:$DABA_{1.2}$-CMS550	550 ℃; Argon	20362	2825	441	46.2	6.4	[145]
	Kapton	--*	2.350	0.505	0.270	8.70	1.87	[146]
	Kapton-CMS580	580 ℃; Vacuum	623.6	188.3	58.49	10.7	3.22	[146]
	Kapton-CMS800	800 ℃; Vacuum	324.7	68.9	7.64	42.5	9.02	[146]
	UIP-R	--*	0.696	0.196	0.064	10.96	3.08	[146]

Precursor	Membrane	Pyrolysis Temp.; Inert condition	Permeability			Selectivity		Ref
			CO_2	O_2	N_2	CO_2/N_2	O_2/N_2	
	UIP-R-CMS580	580 ℃; Vacuum	843.3	293.5	93.14	9.1	3.15	[146]
	UIP-R-CMS800	800 ℃; Vacuum	402.6	102.7	11.79	34.2	8.71	[146]
	P84 HT	--*	0.557	0.168	0.048	11.60	3.50	[146]
	P84 HT-CMS580	580 ℃; Vacuum	1291	341.2	142.8	9.0	2.39	[146]
	P84 HT-CMS800	800 ℃; Vacuum	407.6	126.4	14.80	27.5	8.55	[146]
PEI	Ultem1010	--*	2	0.5	0.07	28	6.8	[100]
	Ultem1010-CMS700 (Supported)	700 ℃; Argon	156	37.9	4.56	34.2	8.3	[69, 100]
PBI	PBI	--*	0.112	0.009	0.005	24.15	2.02	[146]
	PBI-CMS580	580 ℃; Vacuum	183.8	155.9	5.35	34.4	29.16	[146]
	PBI-CMS800	800 ℃; Vacuum	42.5	19.0	0.70	60.8	27.11	[146]
	PBI-6F	--*	26	6.5	1.0	26.0	6.5	[147]
	PBI-6F-CMS600	600 ℃; Argon	7920	1905	247	32.0	7.7	[147]
PIM	Trip(Me_2)-TB	--*	2250	620	115	19.6	5.4	[148]
	Trip(Me_2)-TB-CMS500	500 ℃; Nitrogen	992	206	52	19.1	4.0	[148]

Precursor	Membrane	Pyrolysis Temp.; Inert condition	Permeability			Selectivity		Ref
			CO_2	O_2	N_2	CO_2/N_2	O_2/N_2	
	Trip(Me_2)-TB-CMS600	600 ℃; Nitrogen	2760	636	90.5	30.5	7.0	[148]
	Trip(Me_2)-TB-CMS700	700 ℃; Nitrogen	530	130	15.9	33.3	8.2	[148]
	Trip(Me_2)-TB-CMS800	800 ℃; Nitrogen	397	98	11.4	34.8	8.6	[148]
	EA(Me_2)-TB	--*	1206	348	59	20.4	5.9	[148]
	EA(Me_2)-TB-CMS500	500 ℃; Nitrogen	251	56	9	27.9	6.2	[148]
	EA(Me_2)-TB-CMS600	600 ℃; Nitrogen	372	94	13	28.6	7.5	[148]
	EA(Me_2)-TB-CMS700	700 ℃; Nitrogen	173	45	4.7	36.8	9.6	[148]
	EA(Me_2)-TB-CMS800	800 ℃; Nitrogen	42.5	12	0.94	45.2	12.6	[148]
	PI-TB-4	--*	21.4	--	1.3	17.1	--	[143]
	PI-TB-4-CMS450	450 ℃; Argon	11.8	--	1	11.8	--	[143]
	PI-TB-4-CMS600	600 ℃; Argon	542.6	--	28.3	19.2	--	[143]
PFA	SCPFA-500	500 ℃; Argon	293.1	52.9	13.7	21.4	3.9	[162]
	SCPFA-600	600 ℃; Argon	435.5	79.4	14.2	30.7	5.6	[162]

Precursor	Membrane	Pyrolysis Temp.; Inert condition	Permeability			Selectivity		Ref
			CO_2	O_2	N_2	CO_2/N_2	O_2/N_2	
	SCPFA -700	700 ℃; Argon	193.3	54.8	8.5	22.7	6.4	[162]
	SCPFA -800	800 ℃; Argon	80.2	18.9	3.4	23.9	5.6	[162]
	PFA-CMS600 (Supported)	600 ℃; Argon	18.6	6.39	0.747	24.9	8.6	[69, 164]
	PFA-CMS700 (Supported)	700 ℃; Argon	14.7	5.89	0.478	30.8	12.3	[69, 164]
	PFA-CMS800 (Supported)	800 ℃; Argon	6.51	1.58	0.123	52.9	12.8	[69, 164]
	PFA-CMS900 (Supported)	900 ℃; Argon	3.53	0.777	0.0598	59.0	13.0	[69, 164]
PR	CM-20-650 (Supported)	650 ℃; Nitrogen	165.4	78.1	10.1	16.4	7.7	[69, 167]
	CM-20-750 (Supported)	750 ℃; Nitrogen	47.0	10.9	3.4	13.7	3.2	[69, 167]
	CM-20-850 (Supported)	850 ℃; Nitrogen	13.0	6.6	3.0	4.3	2.2	[69, 167]
PPN	PPN400 (Supported)	--[*]	4.4	1.1	0.2	22.1	5.6	This work

Precursor	Membrane	Pyrolysis Temp.; Inert condition	Permeability			Selectivity		Ref
			CO_2	O_2	N_2	CO_2/N_2	O_2/N_2	
	PPN400-CMS550 (Supported)	550 ℃; Argon	7623	2625	1082	7.0	2.4	This work
	PPN400-CMS750 (Supported)	750 ℃; Argon	3568	760	60.8	58.7	12.5	This work

Note: *Polymeric precursor before carbonization.

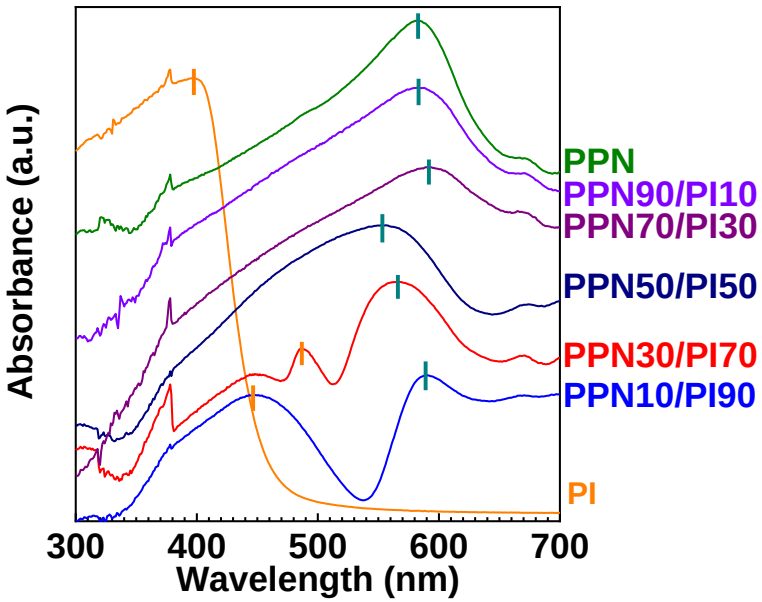

Figure S3 UV-Vis spectrum of PI and PPN/PI blends.

Table S2 Gas permeability and permselectivity (± σ) of PI, PPN/PI, and thermally treated membranes from pure gas permeation analysis in this work.

Membrane	Permeability (Barrer)			Permselectivity (α)		
	H_2	CO_2	N_2	H_2/CO_2	H_2/N_2	CO_2/N_2
PI	14.7 ± 0.8	7.2 ± 0.5	0.28 ± 0.01	2.0 ± 0.2	53.3 ± 3.2	26.1 ± 1.8
PI-280	17.6 ± 0.3	10.7 ± 0.5	0.34 ± 0.02	1.6 ± 0.1	52.2 ± 3.1	31.8 ± 2.3
PPN10PI90	8.8 ± 0.1	4.1 ± 0.4	0.12 ± 0.01	2.2 ± 0.2	71.2 ± 3.9	32.8 ± 3.5
PPN10PI90-280	7.8 ± 0.7	1.8 ± 0.2	0.11 ± 0.01	4.3 ± 0.6	67.4 ± 7.5	15.6 ± 2.1
PRN30PI70	2.7 ± 0.1	0.041 ± 0.005	0.0017 ± 0.0002	66.4 ± 8.4	1637 ± 211	24.7 ± 4.4
PPN30PI70-220	4.3 ± 0.3	0.058 ± 0.004	0.014 ± 0.001	74.3 ± 7.3	316 ± 39	4.2 ± 0.5
PPN30PI70-280	6.5 ± 0.1	0.37 ± 0.06	0.045 ± 0.003	17.4 ± 2.7	146 ± 11	8.4 ± 1.4
PPN30PI70-325	13.6 ± 1.1	3.7 ± 0.2	0.13 ± 0.01	3.7 ± 0.3	106 ± 8	28.9 ± 1.2

Table S3 Comparison of pure-gas and mixed-gas (H_2/CO_2 50:50 mol%) permeability and permselectivity of PPN30/PI70 with respect to pressure difference.

Pressure difference (Δp)	Permeability (Barrer*)		Permselectivity (α)
Pure gas	H_2	CO_2	H_2/CO_2
2.0 atm	2.7 ± 0.1	0.041 ± 0.005	66.4 ± 8.4
H_2/CO_2 50:50 mol%	H_2	CO_2	H_2/CO_2
2.0 atm	0.089 ± 0.006	0.038 ± 0.002	2.3 ± 0.2
5.0 atm	0.25 ± 0.02	0.067 ± 0.004	3.8 ± 0.4
8.0 atm	0.32 ± 0.01	0.11 ± 0.01	3.0 ± 0.3

References

[1] D. Augustine, M.S. Chandran, D. Mathew, C.P. Reghunadhan Nair, Chapter 18 - Polyphthalonitrile resins and their high-end applications, in: Q. Guo (Ed.), Thermosets (Second Edition), Elsevier, 2018, pp. 577-619. https://doi.org/10.1016/B978-0-08-101021-1.00018-6.

[2] H. Gu, C. Gao, A. Du, Y. Guo, H. Zhou, T. Zhao, *et al.*, An overview of high-performance phthalonitrile resins: fabrication and electronic applications, J. Mater. Chem. C 10(8) (2022) 2925-2937. https://doi.org/10.1039/D1TC05715D.

[3] Y.S. Tay, M. Liu, J.S.K. Lim, H. Chen, X. Hu, Phthalonitrile prepolymer and PAN blends: New strategy for precursor stabilization and pyrolytic char yield enhancement, Polym. Degrad. Stab. 172 (2020). https://doi.org/10.1016/j.polymdegradstab.2019.109056.

[4] Z. Weng, K. Zhang, Y. Qi, T. Zhang, M. Xia, F. Hu, *et al.*, Scalable fabrication of heteroatom-doped versatile hierarchical porous carbons with an all-in-one phthalonitrile precursor and their applications, Carbon 159 (2020) 495-503. https://doi.org/10.1016/j.carbon.2019.12.065.

[5] L. Zhang, M. Liu, S. Roy, E.K. Chu, K.Y. See, X. Hu, Phthalonitrile-Based Carbon Foam with High Specific Mechanical Strength and Superior Electromagnetic Interference Shielding Performance, ACS Appl. Mater. Interfaces 8(11) (2016) 7422-30. https://doi.org/10.1021/acsami.5b12072.

[6] T.M. Keller, D.D. Dominguez, High temperature resorcinol-based phthalonitrile polymer, Polymer 46(13) (2005) 4614-4618. https://doi.org/10.1016/j.polymer.2005.03.068.

[7] T. Yu Shan, New organic precursors for carbon material : precursor development and carbonization process, Ph.D thesis, 2021. https://doi.org/doi:10.32657/10356/153306.

[8] S.B. Sastri, T.M. Keller, Phthalonitrile polymers: Cure behavior and properties, J. Polym. Sci., Part A: Polym. Chem. 37(13) (1999) 2105-2111. https://doi.org/10.1002/(SICI)1099-0518(19990701)37:13<2105::AID-POLA25>3.0.CO;2-A.

[9] M. Liu, Aromatic heterocyclic resin: precursor for carbon materials and high temperature foams, Ph.D thesis, 2012. https://doi.org/10.32657/10356/49904.

[10] Y.S. Tay, E.J.R. Phua, Z. Chen, C.L. Gan, Simultaneous Enhancement of Polymerization Kinetics and Properties of Phthalonitrile Using Alumina Fillers, ACS omega 7(37) (2022) 32996-33003. https://doi.org/10.1021/acsomega.2c02667.

[11] M. Gao, T. Li, W. Kong, X. Sun, L. Liu, B. Li, *et al.*, Novel liquid phthalonitrile monomers towards high performance resin, Eur. Polym. J. 191 (2023) 112027. https://doi.org/10.1016/j.eurpolymj.2023.112027.

[12] W. Kong, J. Sun, M. Gao, T. Li, M. Liu, Y. Song, High-performance boron-containing phthalonitrile resins, Polym. Chem. 14(19) (2023) 2317-2325. https://doi.org/10.1039/D3PY00070B.

[13] E.J.R. Phua, M. Liu, B. Cho, Q. Liu, S. Amini, X. Hu, *et al.*, Novel high temperature polymeric encapsulation material for extreme environment electronics packaging, Mater. Des. 141 (2018) 202-209. https://doi.org/10.1016/j.matdes.2017.12.029.

[14] P. Jia Chin, Tunable optical and dielectric properties of metal phthalocyanine based coatings as passive camouflage materials, Nanyang Technological University, 2020.

[15] A.W. Snow, J.R. Griffith, N. Marullo, Syntheses and characterization of heteroatom-bridged metal-free phthalocyanine network polymers and model compounds, Macromolecules 17(8) (1984) 1614-1624. https://doi.org/10.1021/ma00138a033.

[16] J. Hu, P. Yuan, K. Zeng, G. Yang, Study of the curing kinetics of a benzimidazole/phthalonitrile resin system, Thermochim. Acta 590 (2014) 30-39. https://doi.org/10.1016/j.tca.2014.06.006.

[17] J. Zeng, W. Xie, Y. Guo, T. Zhao, H. Zhou, Q. Wang, *et al.*, Magnetic field facilitated electrocatalytic degradation of tetracycline in wastewater by magnetic porous carbonized phthalonitrile resin, Appl. Catal., B 340 (2024) 123225. https://doi.org/10.1016/j.apcatb.2023.123225.

[18] V. Aleshkevich, O. Morozov, A. Babkin, A. Kepman, B. Bulgakov, High-performance C/C composites derived from phthalonitrile matrix CFRP via a few cycles of vacuum-assisted impregnation-carbonization, Compos. Part A Appl. Sci. Manuf. 182 (2024) 108201. https://doi.org/10.1016/j.compositesa.2024.108201.

[19] Y. Lu, J. Hu, K.W.J. Ng, X. Hu, Micro-fabrication of glassy carbon with low shrinkage and high char yield using high-performance photocurable phthalonitrile (PN) resins, Addit. Manuf. 83 (2024) 104053. https://doi.org/10.1016/j.addma.2024.104053.

[20] J. Zeng, W. Xie, H. Zhou, T. Zhao, B.B. Xu, Q. Jiang, *et al.*, Nitrogen-doped graphite-like carbon derived from phthalonitrile resin with controllable negative magnetoresistance and negative permittivity, Adv. Compos. Hybrid Mater. 6(2) (2023) 64. https://doi.org/10.1007/s42114-023-00639-y.

[21] H. Xiao, T. Zhou, J. Lv, X. He, M. Chen, K. Zeng, *et al.*, A High-Mechanical-Strength Carbon/Graphene Porous Composite with Improved EMI Shielding Derived from High Nitrogen-Containing Bio-based Adenine-Containing Phthalonitrile Resin, J. Electron. Mater. 51(9) (2022) 5120-5133. https://doi.org/10.1007/s11664-022-09720-6.

[22] C. Gao, M. Yang, W. Xie, H. Zhang, H. Gu, A. Du, *et al.*, Adjustable magnetoresistance in semiconducting carbonized phthalonitrile resin, Chem. Commun. 57(77) (2021) 9894-9897. https://doi.org/10.1039/D1CC04300E.

[23] C. Yin, L. Sheng, Y. Yang, G. Liang, S. Xing, J. Zeng, *et al.*, Interface conjugation enhances the interface adhesion performance of carbon fiber-reinforced phthalonitrile composites by π–π stacking, RSC Adv. 8(67) (2018) 38210-38218. https://doi.org/10.1039/C8RA07680D.

[24] M. Laskoski, T.M. Keller, S.B. Qadri, Direct conversion of highly aromatic phthalonitrile thermosetting resins into carbon nanotube containing solids, Polymer 48(26) (2007) 7484-7489. https://doi.org/10.1016/j.polymer.2007.11.003.

[25] B. Liang, J. Wang, J. Hu, C. Li, R. Li, Y. Liu, *et al.*, TG-MS-FTIR study on pyrolysis behavior of phthalonitrile resin, Polym. Degrad. Stab. 169 (2019). https://doi.org/10.1016/j.polymdegradstab.2019.108954.

[26] S. Zhang, M. Wu, J. Rong, X. Zhang, W. Han, T. Zhao, *et al.*, Synthesis and Characterization of Pyrimidine-Based Novel Phthalonitrile Resins with Excellent Processing Performance and High Glass Transition Temperature, ChemistrySelect 8(13) (2023) e202204876. https://doi.org/10.1002/slct.202204876.

[27] H. Wang, Z. Zhang, P. Ji, X. Yu, K. Naito, Q. Zhang, Synthesis and properties of a novel high-temperature vinylpyridine-based phthalonitrile polymer, High Perform. Polym. 31(7) (2019) 820-830. https://doi.org/10.1177/0954008318801911.

[28] J. Xu, H. Wang, Z. Zhang, K. Yang, P. Li, X. Chen, *et al.*, Synthesis and properties of a high-performance pyrimidine-containing self-catalyzed phthalonitrile polymer, J. Polym. Sci., Part A: Polym. Chem. 57(23) (2019) 2287-2294. https://doi.org/10.1002/pola.29459.

[29] K. Yang, X. Chen, Z. Zhang, X. Yu, K. Naito, Q. Zhang, Introducing rigid pyrimidine ring to improve the mechanical properties and thermal-oxidative stabilities of phthalonitrile resin, Polym. Adv. Technol. 31(2) (2020) 328-337. https://doi.org/10.1002/pat.4773.

[30] H. Wang, J. Wang, H. Guo, X. Chen, X. Yu, Y. Ma, *et al.*, A novel high temperature vinylpyridine-based phthalonitrile polymer with a low melting point and good mechanical properties, Polym. Chem. 9(8) (2018) 976-983. https://doi.org/10.1039/C7PY01990D.

[31] N. Mushtaq, G. Chen, L.R. Sidra, Y. Liu, X. Fang, Synthesis and crosslinking study of isomeric poly(thioether ether imide)s containing pendant nitrile and terminal phthalonitrile groups, Polym. Chem. 7(48) (2016) 7427-7435. https://doi.org/10.1039/c6py01705c.

[32] T. Liu, Y. Li, Y. Su, H. Yu, N. Zhao, Y. Yang, *et al.*, Preparation and properties of poly(aryl ether ketone) based phthalonitrile resins/clay nanocomposites, Polym. Compos. 37(10) (2016) 3003-3014. https://doi.org/10.1002/pc.23497.

[33] N.B. McKeown, Phthalocyanine-containing polymers, J. Mater. Chem. 10(9) (2000) 1979-1995. https://doi.org/10.1039/B000793P.

[34] N.B. McKeown, P.M. Budd, Polymers of intrinsic microporosity (PIMs): organic materials for membrane separations, heterogeneous catalysis and hydrogen storage, Chem. Soc. Rev. 35(8) (2006) 675-83. https://doi.org/10.1039/b600349d.

[35] N.B. McKeown, S. Makhseed, P.M. Budd, Phthalocyanine-based nanoporous network polymers, Chem. Commun. (Camb.) (23) (2002) 2780-1. https://doi.org/10.1039/b207642j.

[36] C. Gao, H. Gu, A. Du, H. Zhou, D. Pan, N. Naik, *et al.*, Polyaniline facilitated curing of phthalonitrile resin with enhanced processibility and mechanical property, Polymer 219 (2021) 123533. https://doi.org/10.1016/j.polymer.2021.123533.

[37] Y. Han, W.S.W. Ho, Polymeric membranes for CO_2 separation and capture, J. Membr. Sci. 628 (2021). https://doi.org/10.1016/j.memsci.2021.119244.

[38] H. Sanaeepur, A. Ebadi Amooghin, S. Bandehali, A. Moghadassi, T. Matsuura, B. Van der Bruggen, Polyimides in membrane gas separation: Monomer's molecular design and structural engineering, Prog. Polym. Sci. 91 (2019) 80-125. https://doi.org/10.1016/j.progpolymsci.2019.02.001.

[39] K. Vanherck, G. Koeckelberghs, I.F.J. Vankelecom, Crosslinking polyimides for membrane applications: A review, Prog. Polym. Sci. 38(6) (2013) 874-896. https://doi.org/10.1016/j.progpolymsci.2012.11.001.

[40] D.-J. Liaw, K.-L. Wang, Y.-C. Huang, K.-R. Lee, J.-Y. Lai, C.-S. Ha, Advanced polyimide materials: Syntheses, physical properties and applications, Prog. Polym. Sci. 37(7) (2012) 907-974. https://doi.org/10.1016/j.progpolymsci.2012.02.005.

[41] Y. Zhang, J.Y. Chong, R. Xu, R. Wang, Effective separation of water-DMSO through solvent resistant membrane distillation (SR-MD), Water Res. 197 (2021) 117103. https://doi.org/10.1016/j.watres.2021.117103.

[42] H. Dommati, S.S. Ray, J.-C. Wang, S.-S. Chen, A comprehensive review of recent developments in 3D printing technique for ceramic membrane fabrication for water purification, RSC Adv. 9(29) (2019) 16869-16883. https://doi.org/10.1039/c9ra00872a.

[43] L.C. Hwa, M.B. Uday, N. Ahmad, A.M. Noor, S. Rajoo, K.B. Zakaria, Integration and fabrication of the cheap ceramic membrane through 3D printing technology, Mater. Today Commun. 15 (2018) 134-142. https://doi.org/10.1016/j.mtcomm.2018.02.029.

[44] M. Lee, K. Li, 1.12 Microstructured Ceramic Hollow Fiber Membranes and Their Applications, Comprehensive Membrane Science and Engineering, 2017, pp. 298-329. https://doi.org/10.1016/b978-0-12-409547-2.12276-0.

[45] A. Buekenhoudt, F. Bisignano, G. De Luca, P. Vandezande, M. Wouters, K. Verhulst, Unravelling the solvent flux behaviour of ceramic nanofiltration and ultrafiltration membranes, J. Membr. Sci. 439 (2013) 36-47. https://doi.org/10.1016/j.memsci.2013.03.032.

[46] T.C. Merkel, H. Lin, X. Wei, R. Baker, Power plant post-combustion carbon dioxide capture: An opportunity for membranes, J. Membr. Sci. 359(1-2) (2010) 126-139. https://doi.org/10.1016/j.memsci.2009.10.041.

[47] P.S. Tin, H.Y. Lin, R.C. Ong, T.-S. Chung, Carbon molecular sieve membranes for biofuel separation, Carbon 49(2) (2011) 369-375. https://doi.org/10.1016/j.carbon.2010.09.031.

[48] D.Y. Koh, B.A. McCool, H.W. Deckman, R.P. Lively, Reverse osmosis molecular differentiation of organic liquids using carbon molecular sieve membranes, Science 353(6301) (2016) 804-807. https://doi.org/10.1126/science.aaf1343.

[49] C.-P. Hu, C.K. Polintan, L.L. Tayo, S.-C. Chou, H.-A. Tsai, W.-S. Hung, *et al.*, The gas separation performance adjustment of carbon molecular sieve membrane depending on the chain rigidity and free volume characteristic of the polymeric precursor, Carbon 143 (2019) 343-351. https://doi.org/10.1016/j.carbon.2018.11.037.

[50] X. Zhang, Y. Wang, M. Gu, M. Wang, Z. Zhang, W. Pan, *et al.*, Molecular engineering of dispersed nickel phthalocyanines on carbon nanotubes for selective CO_2 reduction, Nat. Energy. 5(9) (2020) 684-692. https://doi.org/10.1038/s41560-020-0667-9.

[51] W. Guan, Y. Guo, G. Yu, Carbon Materials for Solar Water Evaporation and Desalination, Small (2021) e2007176. https://doi.org/10.1002/smll.202007176.

[52] M. Safarpour, S. Arefi-Oskoui, A. Khataee, A review on two-dimensional metal oxide and metal hydroxide nanosheets for modification of polymeric membranes, J. Ind. Eng. Chem. 82 (2020) 31-41. https://doi.org/10.1016/j.jiec.2019.11.002.

[53] X. Wu, M. Ding, H. Xu, W. Yang, K. Zhang, H. Tian, *et al.*, Scalable Ti3C2Tx MXene Interlayered Forward Osmosis Membranes for Enhanced Water Purification and Organic Solvent Recovery, ACS Nano 14(7) (2020) 9125-9135. https://doi.org/10.1021/acsnano.0c04471.

[54] L. Loske, K. Nakagawa, T. Yoshioka, H. Matsuyama, 2D Nanocomposite Membranes: Water Purification and Fouling Mitigation, Membranes (Basel) 10(10) (2020). https://doi.org/10.3390/membranes10100295.

[55] E. Yang, K. Goh, C.Y. Chuah, R. Wang, T.-H. Bae, Asymmetric mixed-matrix membranes incorporated with nitrogen-doped graphene nanosheets for highly selective gas separation, J. Membr. Sci. 615 (2020). https://doi.org/10.1016/j.memsci.2020.118293.

[56] D. Lere Keshebo, C.-P. Hu, C.-C. Hu, W.-S. Hung, C.-F. Wang, H.-C. Tsai, *et al.*, Effect of composition of few-layered transition metal dichalcogenide nanosheets on separation mechanism of hydrogen selective membranes, J. Membr. Sci. 634 (2021) 119419. https://doi.org/10.1016/j.memsci.2021.119419.

[57] Z.X. Low, P.M. Budd, N.B. McKeown, D.A. Patterson, Gas Permeation Properties, Physical Aging, and Its Mitigation in High Free Volume Glassy Polymers, Chem. Rev. 118(12) (2018) 5871-5911. https://doi.org/10.1021/acs.chemrev.7b00629.

[58] H.A. Mannan, H. Mukhtar, T. Murugesan, R. Nasir, D.F. Mohshim, A. Mushtaq, Recent Applications of Polymer Blends in Gas Separation Membranes, Chem. Eng. Technol. 36(11) (2013) 1838-1846. https://doi.org/10.1002/ceat.201300342.

[59] M. Galizia, W.S. Chi, Z.P. Smith, T.C. Merkel, R.W. Baker, B.D. Freeman, 50th Anniversary Perspective: Polymers and Mixed Matrix Membranes for Gas and Vapor Separation: A Review and Prospective Opportunities, Macromolecules 50(20) (2017) 7809-7843. https://doi.org/10.1021/acs.macromol.7b01718.

[60] L.M. Robeson, The upper bound revisited, J. Membr. Sci. 320(1-2) (2008) 390-400. https://doi.org/10.1016/j.memsci.2008.04.030.

[61] E. Favre, 2.6 Polymeric Membranes for Gas Separation, Comprehensive Membrane Science and Engineering, 2017, pp. 124-175. https://doi.org/10.1016/b978-0-12-409547-2.12743-x.

[62] L.M. Robeson, Q. Liu, B.D. Freeman, D.R. Paul, Comparison of transport properties of rubbery and glassy polymers and the relevance to the upper bound relationship, J. Membr. Sci. 476 (2015) 421-431. https://doi.org/10.1016/j.memsci.2014.11.058.

[63] L.M. Robeson, Correlation of separation factor versus permeability for polymeric membranes, J. Membr. Sci. 62(2) (1991) 165-185. https://doi.org/10.1016/0376-7388(91)80060-J.

[64] M. Rezakazemi, M. Sadrzadeh, T. Matsuura, Thermally stable polymers for advanced high-performance gas separation membranes, Prog. Energy Combust. Sci. 66 (2018) 1-41. https://doi.org/10.1016/j.pecs.2017.11.002.

[65] W. Chen, W. Chen, B. Zhang, S. Yang, C.-Y. Liu, Thermal imidization process of polyimide film: Interplay between solvent evaporation and imidization, Polymer 109 (2017) 205-215. https://doi.org/10.1016/j.polymer.2016.12.037.

[66] R. Giesa, H.W. Schmidt, Soluble Polyimides, in: K.H.J. Buschow, R.W. Cahn, M.C. Flemings, B. Ilschner, E.J. Kramer, S. Mahajan, P. Veyssière (Eds.), Encyclopedia of Materials: Science and Technology, Elsevier, Oxford, 2001, pp. 8750-8752. https://doi.org/10.1016/B0-08-043152-6/01565-5.

[67] H. Park, Relationship between chemical structure of aromatic polyimides and gas permeation properties of their carbon molecular sieve membranes, J. Membr. Sci. 229(1-2) (2004) 117-127. https://doi.org/10.1016/j.memsci.2003.10.023.

[68] O. Sanyal, C. Zhang, G.B. Wenz, S. Fu, N. Bhuwania, L. Xu, *et al.*, Next generation membranes —using tailored carbon, Carbon 127 (2018) 688-698. https://doi.org/10.1016/j.carbon.2017.11.031.

[69] G. Genduso, W. Ogieglo, Y. Wang, I. Pinnau, Carbon molecular sieve gas separation materials and membranes: A comprehensive review, J. Membr. Sci. 699 (2024) 122533. https://doi.org/10.1016/j.memsci.2024.122533.

[70] C.W. Jones, W.J. Koros, Carbon molecular sieve gas separation membranes-I. Preparation and characterization based on polyimide precursors, Carbon 32(8) (1994) 1419-1425. https://doi.org/doi.org/10.1016/0008-6223(94)90135-X.

[71] L.Y. Jiang, Y. Wang, T.-S. Chung, X.Y. Qiao, J.-Y. Lai, Polyimides membranes for pervaporation and biofuels separation, Prog. Polym. Sci. 34(11) (2009) 1135-1160. https://doi.org/10.1016/j.progpolymsci.2009.06.001.

[72] L. Shao, B.T. Low, T.-S. Chung, A.R. Greenberg, Polymeric membranes for the hydrogen economy: Contemporary approaches and prospects for the future, J. Membr. Sci. 327(1) (2009) 18-31. https://doi.org/10.1016/j.memsci.2008.11.019.

[73] P.M. Budd, N.B. McKeown, D. Fritsch, Free volume and intrinsic microporosity in polymers, J. Mater. Chem. 15(20) (2005). https://doi.org/10.1039/b417402j.

[74] K. Mizrahi Rodriguez, S. Lin, A.X. Wu, G. Han, J.J. Teesdale, C.M. Doherty, *et al.*, Leveraging Free Volume Manipulation to Improve the Membrane Separation Performance of Amine-Functionalized PIM-1, Angew. Chem. Int. Ed. 60(12) (2021) 6593-6599. https://doi.org/10.1002/anie.202012441.

[75] M.E. Dose, M. Chwatko, I. Hubacek, N.A. Lynd, D.R. Paul, B.D. Freeman, Thermally cross-linked diaminophenylindane (DAPI) containing polyimides for membrane based gas separations, Polymer 161 (2019) 16-26. https://doi.org/10.1016/j.polymer.2018.11.050.

[76] A. Morisato, H.C. Shen, S.S. Sankar, B.D. Freeman, I. Pinnau, C.G. Casillas, Polymer characterization and gas permeability of poly(1-trimethylsilyl-1-propyne) [PTMSP], poly(1-phenyl-1-propyne) [PPP], and PTMSP/PPP blends, J. Polym. Sci., Part B: Polym. Phys. 34(13) (1996) 2209-2222. https://doi.org/10.1002/(SICI)1099-0488(19960930)34:13<2209::AID-POLB10>3.0.CO;2-9.

[77] C.Z. Liang, T.-S. Chung, J.-Y. Lai, A review of polymeric composite membranes for gas separation and energy production, Prog. Polym. Sci. 97 (2019). https://doi.org/10.1016/j.progpolymsci.2019.06.001.

[78] S.-J. Kim, Y. Ahn, J.F. Kim, S.-E. Nam, H. Park, Y.H. Cho, *et al.*, Effect of solvent on crosslinking of a polyimide membrane using the liquid-phase crosslinking process for CO_2/CH_4 separation, Sep. Purif. Technol. 260 (2021). https://doi.org/10.1016/j.seppur.2020.118213.

[79] S. Mazinani, R. Ramezani, G.F. Molelekwa, S. Darvishmanesh, R. Di Felice, B. Van der Bruggen, Plasticization suppression and CO_2 separation enhancement of Matrimid through homogeneous blending with a new high performance polymer, J. Membr. Sci. 574 (2019) 318-324. https://doi.org/10.1016/j.memsci.2018.12.060.

[80] H. Kawakami, M. Mikawa, S. Nagaoka, Gas transport properties in thermally cured aromatic polyimide membranes, J. Membr. Sci. 118(2) (1996) 223-230. https://doi.org/10.1016/0376-7388(96)00115-9.

[81] K.-i. Okamoto, K. Tanaka, M. Katsube, O. Sueoka, Y. Ito, Positronium formation in various polyimides, Radiat. Phys. Chem. 41(3) (1993) 497-502. https://doi.org/10.1016/0969-806X(93)90011-I.

[82] P. Li, T.S. Chung, D.R. Paul, Gas sorption and permeation in PIM-1, J. Membr. Sci. 432 (2013) 50-57. https://doi.org/10.1016/j.memsci.2013.01.009.

[83] J. Wu, S. Japip, T.-S. Chung, Infiltrating molecular gatekeepers with coexisting molecular solubility and 3D-intrinsic porosity into a microporous polymer scaffold for gas separation, J. Mater. Chem. A 8(13) (2020) 6196-6209. https://doi.org/10.1039/c9ta12028a.

[84] W.F. Yong, F.Y. Li, Y.C. Xiao, T.S. Chung, Y.W. Tong, High performance PIM-1/Matrimid hollow fiber membranes for CO_2/CH_4, O_2/N_2 and CO_2/N_2 separation, J. Membr. Sci. 443 (2013) 156-169. https://doi.org/10.1016/j.memsci.2013.04.037.

[85] W.F. Yong, F.Y. Li, T.S. Chung, Y.W. Tong, Molecular interaction, gas transport properties and plasticization behavior of cPIM-1/Torlon blend membranes, J. Membr. Sci. 462 (2014) 119-130. https://doi.org/10.1016/j.memsci.2014.03.046.

[86] W.F. Yong, H. Zhang, Recent advances in polymer blend membranes for gas separation and pervaporation, Prog. Mater. Sci. 116 (2021). https://doi.org/10.1016/j.pmatsci.2020.100713.

[87] L.M. Robeson, Polymer Blends in Membrane Transport Processes, Ind. Eng. Chem. Res. 49(23) (2010) 11859-11865. https://doi.org/10.1021/ie100153q.

[88] A.A. Lin, T.K. Kwei, A. Reiser, On the physical meaning of the Kwei equation for the glass transition temperature of polymer blends, Macromolecules 22(10) (2002) 4112-4119. https://doi.org/10.1021/ma00200a052.

[89] J.D. Moon, A.T. Bridge, C. D'Ambra, B.D. Freeman, D.R. Paul, Gas separation properties of polybenzimidazole/thermally-rearranged polymer blends, J. Membr. Sci. 582 (2019) 182-193. https://doi.org/10.1016/j.memsci.2019.03.067.

[90] N.P. Panapitiya, S.N. Wijenayake, D.D. Nguyen, Y. Huang, I.H. Musselman, K.J. Balkus, Jr., *et al.*, Gas Separation Membranes Derived from High-Performance Immiscible Polymer Blends Compatibilized with Small Molecules, ACS Appl. Mater. Interfaces. 7(33) (2015) 18618-18627. https://doi.org/10.1021/acsami.5b04747.

[91] L. Huang, Z. Xing, X. Zhuang, J. Wei, Y. Ma, B. Wang, *et al.*, Polymeric membranes and their derivatives for H_2/CH_4 separation: State of the art, Sep. Purif. Technol. 297 (2022) 121504. https://doi.org/10.1016/j.seppur.2022.121504.

[92] N. Sazali, A comprehensive review of carbon molecular sieve membranes for hydrogen production and purification, Int. J. Adv. Manuf. Tech. 107(5-6) (2020) 2465-2483. https://doi.org/10.1007/s00170-020-05196-y.

[93] M. Kiyono, P.J. Williams, W.J. Koros, Effect of pyrolysis atmosphere on separation performance of carbon molecular sieve membranes, J. Membr. Sci. 359(1-2) (2010) 2-10. https://doi.org/10.1016/j.memsci.2009.10.019.

[94] S.-J. Kim, Y. Kwon, D. Kim, H. Park, Y.H. Cho, S.-E. Nam, *et al.*, A Review on Polymer Precursors of Carbon Molecular Sieve Membranes for Olefin/Paraffin Separation, Membranes 11(7) (2021) 482.

[95] J.E. Koresh, A. Sofer, Molecular Sieve Carbon Permselective Membrane. Part I. Presentation of a New Device for Gas Mixture Separation, Sep. Sci. Technol. 18(8) (1983) 723-734. https://doi.org/10.1080/01496398308068576.

[96] M. Liu, M.D. Nothling, S. Zhang, Q. Fu, G.G. Qiao, Thin film composite membranes for postcombustion carbon capture: Polymers and beyond, Prog. Polym. Sci. 126 (2022) 101504. https://doi.org/10.1016/j.progpolymsci.2022.101504.

[97] N. Sazali, W.N. Wan Salleh, A.F. Ismail, N.H. Ismail, K. Kadirgama, A brief review on carbon selective membranes from polymer blends for gas separation performance, Rev. Chem. Eng. 37(3) (2021) 339-362. https://doi.org/10.1515/revce-2018-0086.

[98] Y.H. Yoon, D. O'Nolan, M.L. Beauvais, K.W. Chapman, R.P. Lively, Direct evidence of the ultramicroporous structure of carbon molecular sieves, Carbon 210 (2023) 118002. https://doi.org/10.1016/j.carbon.2023.118002.

[99] M. Rungta, G.B. Wenz, C. Zhang, L. Xu, W. Qiu, J.S. Adams, *et al.*, Carbon molecular sieve structure development and membrane performance relationships, Carbon 115 (2017) 237-248. https://doi.org/10.1016/j.carbon.2017.01.015.

[100] Y.-J. Fu, C.-C. Hu, D.-W. Lin, H.-A. Tsai, S.-H. Huang, W.-S. Hung, *et al.*, Adjustable microstructure carbon molecular sieve membranes derived from thermally stable polyetherimide/polyimide blends for gas separation, Carbon 113 (2017) 10-17. https://doi.org/10.1016/j.carbon.2016.11.026.

[101] J. Koresh, A. Soffer, A molecular sieve carbon membrane for continuous process gas separation, Carbon 22(2) (1984) 225. https://doi.org/10.1016/0008-6223(84)90402-0.

[102] H. Hatori, Y. Yamada, M. Shiraishi, H. Nakata, S. Yoshitomi, Carbon molecular sieve films from polyimide, Carbon 30(2) (1992) 305-306. https://doi.org/10.1016/0008-6223(92)90095-E.

[103] H. Suda, K. Haraya, Gas Permeation through Micropores of Carbon Molecular Sieve Membranes Derived from Kapton Polyimide, J. Phys. Chem. B 101(20) (1997) 3988-3994. https://doi.org/10.1021/jp963997u.

[104] K.M. Steel, W.J. Koros, Investigation of porosity of carbon materials and related effects on gas separation properties, Carbon 41(2) (2003) 253-266. https://doi.org/10.1016/S0008-6223(02)00309-3.

[105] J.S. Adams, A.K. Itta, C. Zhang, G.B. Wenz, O. Sanyal, W.J. Koros, New insights into structural evolution in carbon molecular sieve membranes during pyrolysis, Carbon 141 (2019) 238-246. https://doi.org/10.1016/j.carbon.2018.09.039.

[106] O. Sanyal, S.S. Hays, N.E. León, Y.A. Guta, A.K. Itta, R.P. Lively, *et al.*, A Self-Consistent Model for Sorption and Transport in Polyimide-Derived Carbon Molecular Sieve Gas Separation Membranes, Angew. Chem. Int. Ed. 59(46) (2020) 20343-20347. https://doi.org/10.1002/anie.202006521.

[107] W. Qiu, J.E. Leisen, Z. Liu, W. Quan, W.J. Koros, Key Features of Polyimide-Derived Carbon Molecular Sieves, Angew. Chem. Int. Ed. 60(41) (2021) 22322-22331. https://doi.org/10.1002/anie.202106740.

[108] G.M. Jenkins, K. Kawamura, Polymeric Carbons: Carbon Fibre, Glass and Char, Cambridge University Press, 1976.

[109] C.-P. Hu, J.S.K. Lim, K.-H. Ping, W.-S. Hung, Y.N. Liang, X.M. Hu, Understanding hydrogen solubility and free volume characteristics in charge-transfer

phthalonitrile prepolymer and polyimide blend membranes, J. Membr. Sci. 687 (2023) 122058. https://doi.org/10.1016/j.memsci.2023.122058.

[110] T.A. Centeno, A.B. Fuertes, Supported carbon molecular sieve membranes based on a phenolic resin, J. Membr. Sci. 160(2) (1999) 201-211. https://doi.org/10.1016/S0376-7388(99)00083-6.

[111] M.A. Llosa Tanco, D.A. Pacheco Tanaka, A. Mendes, Composite-alumina-carbon molecular sieve membranes prepared from novolac resin and boehmite. Part II: Effect of the carbonization temperature on the gas permeation properties, Int. J. Hydrog. Energy 40(8) (2015) 3485-3496. https://doi.org/10.1016/j.ijhydene.2014.11.025.

[112] L.-H. Cheng, Y.-J. Fu, K.-S. Liao, J.-T. Chen, C.-C. Hu, W.-S. Hung, *et al.*, A high-permeance supported carbon molecular sieve membrane fabricated by plasma-enhanced chemical vapor deposition followed by carbonization for CO_2 capture, J. Membr. Sci. 460 (2014) 1-8. https://doi.org/10.1016/j.memsci.2014.02.033.

[113] K.-S. Liao, H. Chen, S. Awad, J.-P. Yuan, W.-S. Hung, K.-R. Lee, *et al.*, Determination of Free-Volume Properties in Polymers Without Orthopositronium Components in Positron Annihilation Lifetime Spectroscopy, Macromolecules 44(17) (2011) 6818-6826. https://doi.org/10.1021/ma201324k.

[114] P.S. Tin, T.-S. Chung, A.J. Hill, Advanced Fabrication of Carbon Molecular Sieve Membranes by Nonsolvent Pretreatment of Precursor Polymers, Ind. Eng. Chem. Res. 43(20) (2004) 6476-6483. https://doi.org/10.1021/ie049606c.

[115] K.-S. Liao, Y.-J. Fu, C.-C. Hu, J.-T. Chen, D.-W. Lin, K.-R. Lee, *et al.*, Microstructure of carbon molecular sieve membranes and their application to separation of aqueous bioethanol, Carbon 50(11) (2012) 4220-4227. https://doi.org/10.1016/j.carbon.2012.05.003.

[116] Y.C. Jean, Principles and Applications of Positron and Positronium Chemistry, WORLD SCIENTIFIC, 2003.

[117] S.J. Tao, Positronium Annihilation in Molecular Substances, J. Chem. Phys. 56(11) (1972) 5499-5510. https://doi.org/10.1063/1.1677067.

[118] W. Ogieglo, A. Furchner, X. Ma, K. Hazazi, A.T. Alhazmi, I. Pinnau, Thin Composite Carbon Molecular Sieve Membranes from a Polymer of Intrinsic Microporosity Precursor, ACS Appl. Mater. Interfaces. 11(20) (2019) 18770-18781. https://doi.org/10.1021/acsami.9b04602.

[119] K. Mizrahi Rodriguez, W.-N. Wu, T. Alebrahim, Y. Cao, B.D. Freeman, D. Harrigan, *et al.*, Multi-lab study on the pure-gas permeation of commercial polysulfone (PSf) membranes: Measurement standards and best practices, J. Membr. Sci. 659 (2022) 120746. https://doi.org/10.1016/j.memsci.2022.120746.

[120] M. Laskoski, T. Keller, Fire Resistant, 2nd Generation Resorcinol, PEEK™-Like Phthalonitrile Composites For Advanced Applications, TechConnect Br. 2017 - Adv. Mater. (2017) 254-257.

[121] T.M. Keller, D.D. Dominguez, M. Laskoski, Oligomeric bisphenol A-based PEEK-like phthalonitrile-cure and polymer properties, J. Polym. Sci., Part A: Polym. Chem. 54(23) (2016) 3769-3777. https://doi.org/10.1002/pola.28276.

[122] M. Brewis, G.J. Clarkson, V. Goddard, M. Helliwell, A.M. Holder, N.B. McKeown, Silicon Phthalocyanines with Axial Dendritic Substituents, Angew Chem. Int. Ed. Engl. 37(8) (1998) 1092-1094. https://doi.org/10.1002/(SICI)1521-3773(19980504)37:8<1092::AID-ANIE1092>3.0.CO;2-G.

[123] F.J.M. Hoeben, P. Jonkheijm, E.W. Meijer, A.P.H.J. Schenning, About Supramolecular Assemblies of π-Conjugated Systems, Chem. Rev. 105(4) (2005) 1491-1546. https://doi.org/10.1021/cr030070z.

[124] G. de la Torre, P. Vázquez, F. Agulló-López, T. Torres, Role of Structural Factors in the Nonlinear Optical Properties of Phthalocyanines and Related Compounds, Chem. Rev. 104(9) (2004) 3723-3750. https://doi.org/10.1021/cr030206t.

[125] A.W. Snow, N.L. Jarvis, Molecular association and monolayer formation of soluble phthalocyanine compounds, J. Am. Chem. Soc. 106(17) (1984) 4706-4711. https://doi.org/10.1021/ja00329a012.

[126] İ. Değirmencioğlu, M. Er, R. Bayrak, A.R. Özkaya, Redox-Switchable New Phthalocyanines Containing Hydrazono-Thiazole-Carboxylate Fragments: Synthesis, Electrochemical, Spectroelectrochemical and Electrocolorimetric Investigation, J. Fluoresc. 27(3) (2017) 869-881. https://doi.org/10.1007/s10895-016-2023-9.

[127] J. Wang, C. Wu, R. Liu, S. Li, Enhanced dielectric behavior in nanocomposites of polyurethane bonded with copper phthalocyanine oligomers, Polym. J. 46(5) (2014) 285-292. https://doi.org/10.1038/pj.2013.101.

[128] B. Han, X. Ding, B. Yu, H. Wu, W. Zhou, W. Liu, *et al.*, Two-Dimensional Covalent Organic Frameworks with Cobalt(II)-Phthalocyanine Sites for Efficient Electrocatalytic Carbon Dioxide Reduction, J. Am. Chem. Soc. 143(18) (2021) 7104-7113. https://doi.org/10.1021/jacs.1c02145.

[129] S. Senthilarasu, Y.B. Hahn, S.-H. Lee, Structural analysis of zinc phthalocyanine (ZnPc) thin films: X-ray diffraction study, J. Appl. Phys. 102(4) (2007). https://doi.org/10.1063/1.2771046.

[130] D.R. Tackley, G. Dent, W. Ewen Smith, Phthalocyanines: structure and vibrations, Phys. Chem. Chem. Phys. 3(8) (2001) 1419-1426. https://doi.org/10.1039/B007763L.

[131] L. Ding, J. Qiao, X. Dai, J. Zhang, J. Zhang, B. Tian, Highly active electrocatalysts for oxygen reduction from carbon-supported copper-phthalocyanine synthesized by high temperature treatment, Int. J. Hydrogen Energy 37(19) (2012) 14103-14113. https://doi.org/10.1016/j.ijhydene.2012.07.046.

[132] R. Pode, On the problem of open circuit voltage in metal phthalocyanine/C60 organic solar cells, Adv. Mater. Lett. 2(1) (2012) 3-11. https://doi.org/10.5185/amlett.2010.12186.

[133] M. Rungta, L. Xu, W.J. Koros, Structure–performance characterization for carbon molecular sieve membranes using molecular scale gas probes, Carbon 85 (2015) 429-442. https://doi.org/10.1016/j.carbon.2015.01.008.

[134] Y. Iflah, I. Zilbermann, S. Pevzner, S. Halevy, Y. Bochlin, Y. Kadosh, *et al.*, Growth Behavior of Copper and Platinum Nanoparticles in an Imidazolium Based Ionic Liquid, J. Electrochem. Soc. 164(8) (2017) H5026. https://doi.org/10.1149/2.0031708jes.

[135] I. Kumakiri, K. Tamura, Y. Sasaki, K. Tanaka, H. Kita, Influence of Iron Additive on the Hydrogen Separation Properties of Carbon Molecular Sieve Membranes, Ind. Eng. Chem. Res. 57(15) (2018) 5370-5377. https://doi.org/10.1021/acs.iecr.7b05265.

[136] Y.-H. Chu, D. Yancey, L. Xu, M. Martinez, M. Brayden, W. Koros, Iron-containing carbon molecular sieve membranes for advanced olefin/paraffin separations, J. Membr. Sci. 548 (2018) 609-620. https://doi.org/10.1016/j.memsci.2017.11.052.

[137] N. Kosinov, J. Gascon, F. Kapteijn, E.J.M. Hensen, Recent developments in zeolite membranes for gas separation, J. Membr. Sci. 499 (2016) 65-79. https://doi.org/10.1016/j.memsci.2015.10.049.

[138] S. Samarasinghe, C.Y. Chuah, H.E. Karahan, G. Sethunga, T.H. Bae, Enhanced O_2/N_2 Separation of Mixed-Matrix Membrane Filled with Pluronic-Compatibilized Cobalt Phthalocyanine Particles, Membranes (Basel) 10(4) (2020). https://doi.org/10.3390/membranes10040075.

[139] O. Hosseinkhani, A. Kargari, H. Sanaeepur, Facilitated transport of CO_2 through Co(II)-S-EPDM ionomer membrane, J. Membr. Sci. 469 (2014) 151-161. https://doi.org/10.1016/j.memsci.2014.06.021.

[140] H. Nagar, P. Vadthya, N.S. Prasad, S. Sridhar, Air separation by facilitated transport of oxygen through a Pebax membrane incorporated with a cobalt complex, RSC Adv. 5(93) (2015) 76190-76201. https://doi.org/10.1039/C5RA10755E.

[141] J. Gilron, A. Soffer, Knudsen diffusion in microporous carbon membranes with molecular sieving character, J. Membr. Sci. 209(2) (2002) 339-352. https://doi.org/10.1016/S0376-7388(02)00074-1.

[142] L. Hu, T. Bui Vinh, A. Krishnamurthy, S. Fan, W. Guo, S. Pal, *et al.*, Tailoring sub-3.3 Å ultramicropores in advanced carbon molecular sieve membranes for blue hydrogen production, Sci. Adv. 8(10) (2022) eabl8160. https://doi.org/10.1126/sciadv.abl8160.

[143] B. Zhao, H. Li, Z. Chen, J. Lin, Y. Liu, Enhancing gas separation performance of polyimide with Tröger's bases: Unveiling the impact on polymer and carbon molecular sieve membranes, Sep. Purif. Technol. 336 (2024) 126286. https://doi.org/10.1016/j.seppur.2024.126286.

[144] J. Liang, Z. Wang, M. Huang, S. Wu, Y. Shi, Y. Zhang, *et al.*, Effects on Carbon Molecular Sieve Membrane Properties for a Precursor Polyimide with Simultaneous Flatness and Contortion in the Repeat Unit, ChemSusChem 13(20) (2020) 5531-5538. https://doi.org/10.1002/cssc.202001572.

[145] Z. Liu, W. Qiu, W. Quan, W.J. Koros, Advanced carbon molecular sieve membranes derived from molecularly engineered cross-linkable copolyimide for gas separations, Nat. Mater. 22(1) (2023) 109-116. https://doi.org/10.1038/s41563-022-01426-8.

[146] S.S. Hosseini, M.R. Omidkhah, A. Zarringhalam Moghaddam, V. Pirouzfar, W.B. Krantz, N.R. Tan, Enhancing the properties and gas separation performance of PBI–polyimides blend carbon molecular sieve membranes via optimization of the pyrolysis process, Sep. Purif. Technol. 122 (2014) 278-289. https://doi.org/10.1016/j.seppur.2013.11.021.

[147] J. Olvera-Mancilla, C. Aguilar-Lugo, L. Fomina, F.M. Sanchez-Arevalo, M.O. González-Díaz, R. Sulub-Sulub, *et al.*, Fluorinated Polybenzimidazole as a Novel Precursor for Carbon Molecular Sieve Membranes with Enhanced Gas Separation Properties, Ind. Eng. Chem. Res. 61(19) (2022) 6587-6599. https://doi.org/10.1021/acs.iecr.2c00020.

[148] K. Hazazi, Y. Wang, B. Ghanem, X. Hu, T. Puspasari, C. Chen, *et al.*, Precise molecular sieving of ethylene from ethane using triptycene-derived submicroporous carbon membranes, Nat. Mater. 22(10) (2023) 1218-1226. https://doi.org/10.1038/s41563-023-01629-7.

[149] B. Comesaña-Gándara, J. Chen, C.G. Bezzu, M. Carta, I. Rose, M.-C. Ferrari, *et al.*, Redefining the Robeson upper bounds for CO_2/CH_4 and CO_2/N_2 separations using a series of ultrapermeable benzotriptycene-based polymers of intrinsic microporosity, Energy Environ. Sci. 12(9) (2019) 2733-2740. https://doi.org/10.1039/c9ee01384a.

[150] R. Swaidan, B. Ghanem, I. Pinnau, Fine-Tuned Intrinsically Ultramicroporous Polymers Redefine the Permeability/Selectivity Upper Bounds of Membrane-Based Air

and Hydrogen Separations, ACS Macro Lett. 4(9) (2015) 947-951. https://doi.org/10.1021/acsmacrolett.5b00512.

[151] F. Radmanesh, A. Tena, E.J.R. Sudhölter, N.E. Benes, Low temperature pyrolysis of thin film composite polyphosphazene membranes for hot gas separation, Mater. Today Nano 24 (2023) 100379. https://doi.org/10.1016/j.mtnano.2023.100379.

[152] Climate Change 2022 - Mitigation of Climate Change: Working Group III Contribution to the Sixth Assessment Report of the Intergovernmental Panel on Climate Change, Cambridge University Press, 2023

[153] D.S. Sholl, R.P. Lively, Seven chemical separations to change the world, Nature 532(7600) (2016) 435-437. https://doi.org/10.1038/532435a.

[154] C.-H. Yu, C.-H. Huang, C.-S. Tan, A Review of CO_2 Capture by Absorption and Adsorption, Aerosol Air Qual. Res. 12(5) (2012) 745-769. https://doi.org/10.4209/aaqr.2012.05.0132.

[155] F. Wu, M.D. Argyle, P.A. Dellenback, M. Fan, Progress in O_2 separation for oxy-fuel combustion–A promising way for cost-effective CO_2 capture: A review, Prog. Energy Combust. Sci. 67 (2018) 188-205. https://doi.org/10.1016/j.pecs.2018.01.004.

[156] M. Liu, M.D. Nothling, P.A. Webley, Q. Fu, G.G. Qiao, Postcombustion Carbon Capture Using Thin-Film Composite Membranes, Acc. Chem. Res. 52(7) (2019) 1905-1914. https://doi.org/10.1021/acs.accounts.9b00111.

[157] B.D. Freeman, Basis of Permeability/Selectivity Tradeoff Relations in Polymeric Gas Separation Membranes, Macromolecules 32(2) (1999) 375-380. https://doi.org/10.1021/ma9814548.

[158] Z. Yang, W. Guo, S.M. Mahurin, S. Wang, H. Chen, L. Cheng, *et al.*, Surpassing Robeson Upper Limit for CO_2/N_2 Separation with Fluorinated Carbon Molecular Sieve Membranes, Chem 6(3) (2020) 631-645. https://doi.org/10.1016/j.chempr.2019.12.006.

[159] P.S. Tin, T.-S. Chung, Y. Liu, R. Wang, Separation of CO_2/CH_4 through carbon molecular sieve membranes derived from P84 polyimide, Carbon 42(15) (2004) 3123-3131. https://doi.org/10.1016/j.carbon.2004.07.026.

[160] D. Kim, Y. Kwon, J.-H. Lee, S.-J. Kim, Y.-I. Park, Tailoring the Stabilization and Pyrolysis Processes of Carbon Molecular Sieve Membrane Derived from Polyacrylonitrile for Ethylene/Ethane Separation, Membranes 12(1) (2022). https://doi.org/10.3390/membranes12010093.

[161] L.I.B. David, A.F. Ismail, Influence of the thermastabilization process and soak time during pyrolysis process on the polyacrylonitrile carbon membranes for O_2/N_2 separation, J. Membr. Sci. 213(1) (2003) 285-291. https://doi.org/10.1016/S0376-7388(02)00513-6.

[162] B. Zhao, H. Li, Y. Yu, Y. Liu, Improving gas separation performances of poly(furfuryl alcohol)-based carbon molecular sieve membrane by tuning furan ring opening and membrane structures, J. Membr. Sci. 688 (2023) 122117. https://doi.org/10.1016/j.memsci.2023.122117.

[163] M.B. Shiflett, H.C. Foley, Ultrasonic Deposition of High-Selectivity Nanoporous Carbon Membranes, Science 285(5435) (1999) 1902-1905. https://doi.org/10.1126/science.285.5435.1902.

[164] C. Song, T. Wang, X. Wang, J. Qiu, Y. Cao, Preparation and gas separation properties of poly(furfuryl alcohol)-based C/CMS composite membranes, Sep. Purif. Technol. 58(3) (2008) 412-418. https://doi.org/10.1016/j.seppur.2007.05.019.

[165] D. Torres, S. Pérez-Rodríguez, L. Cesari, C. Castel, E. Favre, V. Fierro, *et al.*, Review on the preparation of carbon membranes derived from phenolic resins for gas separation: From petrochemical precursors to bioresources, Carbon 183 (2021) 12-33. https://doi.org/10.1016/j.carbon.2021.06.087.

[166] M.A. Llosa Tanco, D.A. Pacheco Tanaka, S.C. Rodrigues, M. Texeira, A. Mendes, Composite-alumina-carbon molecular sieve membranes prepared from novolac resin and boehmite. Part I: Preparation, characterization and gas permeation studies, Int. J. Hydrog. Energy 40(16) (2015) 5653-5663. https://doi.org/10.1016/j.ijhydene.2015.02.112.

[167] Y. Wu, F. Wang, B. Zhang, D. Zhao, T. Wang, J. Qiu, A simple one-step drop-coating approach on fabrication of supported carbon molecular sieve membranes with high gas separation performance, Asia-Pac. J. Chem. Eng. 13(6) (2018) e2251. https://doi.org//10.1002/apj.2251.

[168] S. Li, H. McGinness, T. Wang, R. Guo, Crosslinked Matrimid®-like polyimide membranes with unimodal network structure for enhanced stability and gas separation performance, Polymer 237 (2021). https://doi.org/10.1016/j.polymer.2021.124323.

[169] W. Ogieglo, K. Song, C. Chen, Q. Lei, Y. Han, I. Pinnau, Nano-Confinement Effects on Structural Development and Organic Solvent-Induced Swelling of Ultrathin Carbon Molecular Sieve Films, ACS Appl. Mater. Interfaces 13(18) (2021) 21765-21774. https://doi.org/10.1021/acsami.1c03392.

[170] K. Zhang, X. Yu, Y. Wang, Y. Liu, Thermally Activated Structural Changes of a Norbornene–Benzoxazine–Phthalonitrile Thermosetting System: Simple Synthesis, Self-Catalyzed Polymerization, and Outstanding Flame Retardancy, ACS Appl. Polym. Mater. 1(10) (2019) 2713-2722. https://doi.org/10.1021/acsapm.9b00668.

[171] M.V. Yakovlev, O.S. Morozov, E.S. Afanaseva, B.A. Bulgakov, A.V. Babkin, A.V. Kepman, Tri-functional phthalonitrile monomer as stiffness increasing additive for easy

processable high performance resins, React. Funct. Polym. 146 (2020) 104409. https://doi.org/10.1016/j.reactfunctpolym.2019.104409.

[172] X. Liu, S. Zhang, J. Ye, M. Wu, J. Hou, X. Liu, A highly-crosslinked phthalonitrile modified bismaleimide-triazine resin for PCB substrates: The synergistic effect on curing behavior and properties, Eur. Polym. J. 196 (2023) 112243. https://doi.org/10.1016/j.eurpolymj.2023.112243.

[173] A.S. Singh, J.K. Banshiwal, P. Mishra, S.K. Shukla, D.S. Bag, D.N. Tripathi, Preparation of semi-interpenetrating networks of phthalonitrile and polyetherimide resin: study of their curing characteristics and thermal properties, J. Therm. Anal. Calorim. 148(10) (2023) 4171-4183. https://doi.org/10.1007/s10973-023-12042-2.

[174] Y. Tian, Z. Pu, J. Xia, L. Hu, J. Cheng, J. Zhong, Research on the relationship between structure and properties of the soluble polyaryl ether ketone terminated with phthalonitrile, J. Polym. Res. 26(11) (2019) 252. https://doi.org/10.1007/s10965-019-1933-z.

[175] F. Zhao, R. Liu, C. Kang, X. Yu, K. Naito, X. Qu, *et al.*, A novel high-temperature naphthyl-based phthalonitrile polymer: synthesis and properties, RSC Adv. 4(16) (2014) 8383. https://doi.org/10.1039/c3ra46638h.

[176] T. Zhou, H. Xiao, W. Peng, B. Liang, Y. Liu, J. Lv, *et al.*, Study on pyrolysis behaviors of L-tyrosine-based phthalonitrile resin, Polym. Test. 86 (2020). https://doi.org/10.1016/j.polymertesting.2020.106506.

[177] S. Liu, Z. Kang, L. Fan, X. Li, B. Zhang, Y. Feng, *et al.*, Carbon molecular sieve membranes derived from hydrogen-bonded organic frameworks for CO_2/CH_4 separation, J. Membr. Sci. 678 (2023) 121674. https://doi.org/10.1016/j.memsci.2023.121674.

[178] Y. Ma, M.L. Jue, F. Zhang, R. Mathias, H.Y. Jang, R.P. Lively, Creation of Well-Defined “Mid-Sized” Micropores in Carbon Molecular Sieve Membranes, Angew. Chem. Int. Ed. 58(38) (2019) 13259-13265. https://doi.org/10.1002/anie.201903105.

[179] Y.-J. Fu, K.-S. Liao, C.-C. Hu, K.-R. Lee, J.-Y. Lai, Development and characterization of micropores in carbon molecular sieve membrane for gas separation, Microporous Mesoporous Mater. 143(1) (2011) 78-86. https://doi.org/10.1016/j.micromeso.2011.02.007.

[180] X. Guo, B. Liang, M. Chen, X. He, H. Xiao, K. Zeng, *et al.*, Study on Pyrolysis Behavior of Bio-based adenine containing phthalonitrile resin obtained by powder metallurgy-like process, Polym. Degrad. Stab. 188 (2021). https://doi.org/10.1016/j.polymdegradstab.2021.109569.

[181] L. Sheng, C. Yin, J. Xiao, A novel phthalonitrile monomer with low post cure temperature and short cure time, RSC Adv. 6(27) (2016) 22204-22212. https://doi.org/10.1039/c5ra25431k.

[182] X. Chen, J. Liu, Z. Xi, S. Shan, H. Ding, X. Qu, *et al.*, Synthesis and thermal properties of high temperature phthalonitrile resins cured with self-catalytic amino-contanining phthalonitrle compounds, High Perform. Polym. 29(10) (2016) 1209-1221. https://doi.org/10.1177/0954008316673419.

[183] M. Laskoski, D.D. Dominguez, T.M. Keller, Synthesis and properties of aromatic ether phosphine oxide containing oligomeric phthalonitrile resins with improved oxidative stability, Polymer 48(21) (2007) 6234-6240. https://doi.org/10.1016/j.polymer.2007.08.028.

[184] T.M. Keller, J.R. Griffith, The synthesis of highly fluorinated phthalonitrile resins and cure studies, J. Fluor. Chem. 13(4) (1979) 315-324. https://doi.org/10.1016/S0022-1139(00)82081-3.

[185] L. Lei, L. Bai, A. Lindbråthen, F. Pan, X. Zhang, X. He, Carbon membranes for CO2 removal: Status and perspectives from materials to processes, J. Chem. Eng. 401 (2020). https://doi.org/10.1016/j.cej.2020.126084.

[186] G. Yang, H. Guo, Z. Kang, L. Zhao, S. Feng, F. Jiao, *et al.*, Green Hydrogen Separation from Nitrogen by Mixed-Matrix Membranes Consisting of Nanosized Sodalite Crystals, ChemSusChem 12(19) (2019) 4529-4537. https://doi.org/10.1002/cssc.201802577.

[187] S.S. Hosseini, N. Peng, T.S. Chung, Gas separation membranes developed through integration of polymer blending and dual-layer hollow fiber spinning process for hydrogen and natural gas enrichments, J. Membr. Sci. 349(1) (2010) 156-166. https://doi.org/10.1016/j.memsci.2009.11.043.

[188] M. Yáñez, A. Ortiz, D. Gorri, I. Ortiz, Comparative performance of commercial polymeric membranes in the recovery of industrial hydrogen waste gas streams, Int. J. Hydrog. Energy 46(33) (2021) 17507-17521. https://doi.org/10.1016/j.ijhydene.2020.04.026.

[189] S. Shishatskiy, C. Nistor, M. Popa, S.P. Nunes, K.V. Peinemann, Polyimide Asymmetric Membranes for Hydrogen Separation: Influence of Formation Conditions on Gas Transport Properties, Adv. Eng. Mater. 8(5) (2006) 390-397. https://doi.org/10.1002/adem.200600024.

[190] S. Sridhar, R.S. Veerapur, M.B. Patil, K.B. Gudasi, T.M. Aminabhavi, Matrimid polyimide membranes for the separation of carbon dioxide from methane, J. Appl. Polym. Sci. 106(3) (2007) 1585-1594. https://doi.org/10.1002/app.26306.

[191] G. Chiappetta, G. Clarizia, E. Drioli, Design of an integrated membrane system for a high level hydrogen purification, J. Chem. Eng. 124(1) (2006) 29-40. https://doi.org/10.1016/j.cej.2006.08.009.

[192] P. Tin, Effects of cross-linking modification on gas separation performance of Matrimid membranes, J. Membr. Sci. 225(1-2) (2003) 77-90. https://doi.org/10.1016/j.memsci.2003.08.005.

[193] M. Omidvar, C.M. Stafford, H. Lin, Thermally stable cross-linked P84 with superior membrane H_2/CO_2 separation properties at 100 °C, J. Membr. Sci. 575 (2019) 118-125. https://doi.org/10.1016/j.memsci.2019.01.003.

[194] S. Japip, K.-S. Liao, T.-S. Chung, Molecularly Tuned Free Volume of Vapor Cross-Linked 6FDA-Durene/ZIF-71 MMMs for H_2/CO_2 Separation at 150 °C, Adv. Mater. 29(4) (2017) 1603833. https://doi.org/10.1002/adma.201603833.

[195] Y. Zhang, W.H. Lee, J.G. Seong, J.Y. Bae, Y. Zhuang, S. Feng, *et al.*, Alicyclic segments upgrade hydrogen separation performance of intrinsically microporous polyimide membranes, J. Membr. Sci. 611 (2020) 118363. https://doi.org/10.1016/j.memsci.2020.118363.

[196] W.F. Yong, F.Y. Li, Y.C. Xiao, P. Li, K.P. Pramoda, Y.W. Tong, *et al.*, Molecular engineering of PIM-1/Matrimid blend membranes for gas separation, J. Membr. Sci. 407-408 (2012) 47-57. https://doi.org/10.1016/j.memsci.2012.03.038.

[197] J.M. Pérez-Francisco, J.L. Santiago-García, M.I. Loría-Bastarrachea, M. Aguilar-Vega, Evaluation of Gas Transport Properties of Highly Rigid Aromatic PI DPPD-IMM/PBI Blends, Ind. Eng. Chem. Res. 56(33) (2017) 9355-9366. https://doi.org/10.1021/acs.iecr.7b02074.

[198] H. Wang, D.R. Paul, T.-S. Chung, Surface modification of polyimide membranes by diethylenetriamine (DETA) vapor for H_2 purification and moisture effect on gas permeation, J. Membr. Sci. 430 (2013) 223-233. https://doi.org/10.1016/j.memsci.2012.12.008.

[199] S.S. Hosseini, M.M. Teoh, T.S. Chung, Hydrogen separation and purification in membranes of miscible polymer blends with interpenetration networks, Polymer 49(6) (2008) 1594-1603. https://doi.org/10.1016/j.polymer.2008.01.052.

[200] C.E. Powell, X.J. Duthie, S.E. Kentish, G.G. Qiao, G.W. Stevens, Reversible diamine cross-linking of polyimide membranes, J. Membr. Sci. 291(1-2) (2007) 199-209. https://doi.org/10.1016/j.memsci.2007.01.016.

[201] P.S.O. Patrício, J.A. de Sales, G.G. Silva, D. Windmöller, J.C. Machado, Effect of blend composition on microstructure, morphology, and gas permeability in PU/PMMA

blends, J. Membr. Sci. 271(1) (2006) 177-185. https://doi.org/10.1016/j.memsci.2005.06.064.

[202] S. Mazinani, R. Ramezani, S. Darvishmanesh, G.F. Molelekwa, R. Di Felice, B. Van der Bruggen, A ground breaking polymer blend for CO_2/N_2 separation, J. CO_2 Util. 27 (2018) 536-546. https://doi.org/10.1016/j.jcou.2018.08.024.

[203] V.S.P.K. Neti, X. Wu, M. Hosseini, R.A. Bernal, S. Deng, L. Echegoyen, Synthesis of a phthalocyanine 2D covalent organic framework, CrystEngComm 15(36) (2013). https://doi.org/10.1039/c3ce41091a.

[204] E.L. Spitler, W.R. Dichtel, Lewis acid-catalysed formation of two-dimensional phthalocyanine covalent organic frameworks, Nat. Chem. 2(8) (2010) 672-7. https://doi.org/10.1038/nchem.695.

[205] Z. Yang, T. Liu, S. Wang, H. Chen, X. Suo, T. Wang, *et al.*, Fabrication of Ionic Covalent Triazine Framework-Linked Membranes via a Facile Sol–Gel Approach, Chem. Mater. 33(9) (2021) 3386-3393. https://doi.org/10.1021/acs.chemmater.1c00699.

[206] J. Barsema, S. Klijnstra, J. Balster, N. Vandervegt, G. Koops, M. Wessling, Intermediate polymer to carbon gas separation membranes based on Matrimid PI, J. Membr. Sci. 238(1-2) (2004) 93-102. https://doi.org/10.1016/j.memsci.2004.03.024.

[207] F. Zhou, W.J. Koros, Study of thermal annealing on Matrimid® fiber performance in pervaporation of acetic acid and water mixtures, Polymer 47(1) (2006) 280-288. https://doi.org/10.1016/j.polymer.2005.11.017.

[208] Y. Liu, C. Li, Z. Ren, S. Yan, M.R. Bryce, All-organic thermally activated delayed fluorescence materials for organic light-emitting diodes, Nat. Rev. Mater. 3(4) (2018) 18020. https://doi.org/10.1038/natrevmats.2018.20.

[209] A. Kertik, L.H. Wee, K. Sentosun, J.A.R. Navarro, S. Bals, J.A. Martens, *et al.*, High-Performance CO_2-Selective Hybrid Membranes by Exploiting MOF-Breathing Effects, ACS Appl. Mater. Interfaces 12(2) (2020) 2952-2961. https://doi.org/10.1021/acsami.9b17820.

[210] A. Kertik, L.H. Wee, M. Pfannmöller, S. Bals, J.A. Martens, I.F.J. Vankelecom, Highly selective gas separation membrane using in situ amorphised metal–organic frameworks, Energy Environ. Sci. 10(11) (2017) 2342-2351. https://doi.org/10.1039/c7ee01872j.

[211] M. Peydayesh, T. Mohammadi, O. Bakhtiari, Effective hydrogen purification from methane via polyimide Matrimid® 5218- Deca-dodecasil 3R type zeolite mixed matrix membrane, Energy 141 (2017) 2100-2107. https://doi.org/10.1016/j.energy.2017.11.101.

[212] W. Qiu, C.-C. Chen, L. Xu, L. Cui, D.R. Paul, W.J. Koros, Sub-Tg Cross-Linking of a Polyimide Membrane for Enhanced CO_2 Plasticization Resistance for Natural Gas

Separation, Macromolecules 44(15) (2011) 6046-6056. https://doi.org/10.1021/ma201033j.

[213] Y. Shi, Z. Wang, Y. Shi, S. Zhu, Y. Zhang, J. Jin, Synergistic Design of Enhanced π–π Interaction and Decarboxylation Cross-Linking of Polyimide Membranes for Natural Gas Separation, Macromolecules 55(7) (2022) 2970-2982. https://doi.org/10.1021/acs.macromol.1c02573.

[214] K.D. Vogiatzis, A. Mavrandonakis, W. Klopper, G.E. Froudakis, Ab initio Study of the Interactions between CO_2 and N-Containing Organic Heterocycles, ChemPhysChem 10(2) (2009) 374-383. https://doi.org/10.1002/cphc.200800583.

[215] P. Raveendran, Y. Ikushima, S.L. Wallen, Polar Attributes of Supercritical Carbon Dioxide, Acc. Chem. Res. 38(6) (2005) 478-485. https://doi.org/10.1021/ar040082m.

[216] J.D. Wind, S.M. Sirard, D.R. Paul, P.F. Green, K.P. Johnston, W.J. Koros, Carbon Dioxide-Induced Plasticization of Polyimide Membranes: Pseudo-Equilibrium Relationships of Diffusion, Sorption, and Swelling, Macromolecules 36(17) (2003) 6433-6441. https://doi.org/10.1021/ma0343582.

[217] Y.P. Yampolskii, I. Pinnau, B.D. Freeman, Materials science of membranes for gas and vapor separation, John Wiley & Sons, Hoboken, NJ (2006). https://doi.org/10.1002/047002903X.

[218] O.C. David, D. Gorri, A. Urtiaga, I. Ortiz, Mixed gas separation study for the hydrogen recovery from H_2/CO/N_2/CO_2 post combustion mixtures using a Matrimid membrane, J. Membr. Sci. 378(1) (2011) 359-368. https://doi.org/10.1016/j.memsci.2011.05.029.